Department of Electrical Engineering and Automation

Bearingless Motors: Modeling and Control

Maksim Sokolov

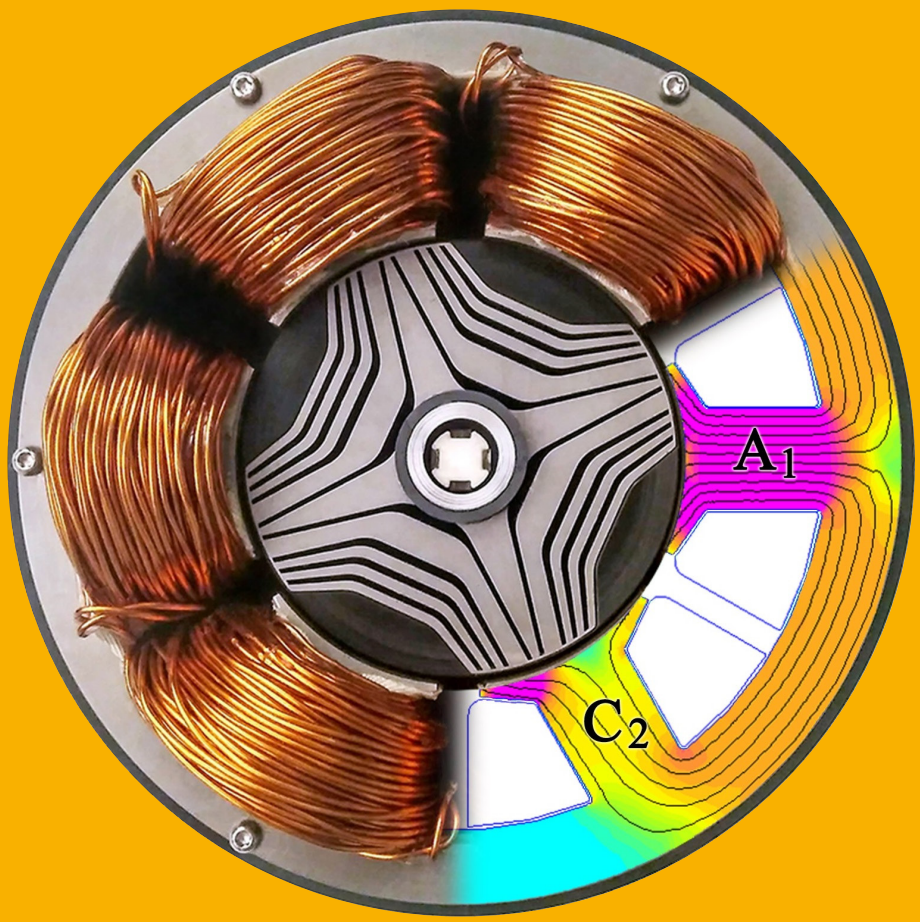

Aalto University

DOCTORAL DISSERTATIONS

Aalto University publication series
DOCTORAL DISSERTATIONS 186/2021

Bearingless Motors: Modeling and Control

Maksim Sokolov

A doctoral dissertation completed for the degree of Doctor of Science (Technology) to be defended, with the permission of the Aalto University School of Electrical Engineering, at a public examination held online and at the lecture hall TU2 of the school on 21 January 2022 at 9:00.

Aalto University
School of Electrical Engineering
Department of Electrical Engineering and Automation
Electric drives research group

Supervising professor
Prof. Marko Hinkkanen, Aalto University, Finland

Thesis advisor
Dr. Seppo Saarakkala, Aalto University / Sulzer Pumps Finland Oy, Finland

Preliminary examiners
Prof. Eric L. Severson, University of Wisconsin-Madison, USA
Prof. Karuna Kalita, Indian Institute of Technology Guwahati, India

Opponent
Prof. Cheng Ming, Southeast University, China

Aalto University publication series
DOCTORAL DISSERTATIONS 186/2021

ISBN 978-952-64-0650-3 (printed)
ISBN 978-952-64-0651-0 (pdf)
ISSN 1799-4934 (printed)
ISSN 1799-4942 (pdf)
http://urn.fi/URN:ISBN:978-952-64-0651-0

Unigrafia Oy
Helsinki 2021

Finland

Printed matter
4041-0619

Aalto University

Abstract

Aalto University, P.O. Box 11000, FI-00076 Aalto www.aalto.fi

Author
Maksim Sokolov

Name of the doctoral dissertation
Bearingless Motors: Modeling and Control

Publisher School of Electrical Engineering

Unit Department of Electrical Engineering and Automation

Series Aalto University publication series DOCTORAL DISSERTATIONS 186/2021

Field of research Electrical Power and Energy Engineering

Manuscript submitted 2 June 2021 **Date of the defence** 21 January 2022

Permission for public defence granted (date) 26 August 2021 **Language** English

☐ **Monograph** ☒ **Article dissertation** ☐ **Essay dissertation**

Abstract

Bearingless motors integrate the functions of an active magnetic bearing (AMB) and an electric motor in the same magnetic circuit, which is utilized both for driving the motor and for maintaining active levitation.

This research focuses on two types of bearingless machines: rotating synchronous reluctance machines (SyRM) and linear flux-switching permanent-magnet (FSPM) machines. The complex nature of these devices results in non-trivial control challenges, which require accurate modeling of the magnetic behavior and of the force production of these machines.

Particular attention in modeling is given to the effects of magnetic saturation and air gap variation. Both effects can result in degraded control performance or even instability if not accounted for. For bearingless SyRMs, an explicit-function-based magnetic model including cross-saturation is proposed. The model is able to predict radial forces even in a saturated machine. Furthermore, based on the textbook model of bearingless SyRMs, an improved model is developed that includes a more precise inverse air-gap approximation. The improved model has better accuracy in the predicted variation of forces and inductances due to eccentricity. For bearingless FSPM linear machines, a dynamic model based on an equivalent magnetic circuit is proposed, taking into account the effects of the saturation, the air gap variation, and the attraction force due to the permanent-magnet (PM) leakage flux. An analysis and characterization of the studied machines is conducted using the finite-element method (FEM).

The proposed dynamic models are utilized as a basis for the development of model-based control systems. Classical state feedback control with direct pole placement is applied to bearingless machines. However, traditional current controllers cannot guarantee consistent performance in the presence of saturation and cross-coupling effects. These effects are automatically taken into account by the proposed state-space flux-linkage controller. A digital implementation of the controller is provided and robustness against the system parameter inaccuracies is analyzed. For levitation control, an observer-based state-space levitation controller is designed. Analytical tuning rules for each proposed controller are presented. Furthermore, feedback linearization is used for accurate calculation of current references based on the requested forces and torque.

The applicability of the developed modeling and control methods is demonstrated with experimental results from three prototype bearingless machines including levitation, rotation, and propulsion tests.

Keywords Bearingless motor, magnetic model, magnetic saturation, eccentricity, inductance, radial force, unbalanced magnetic pull, flux-switching permanent-magnet (FSPM) machine, synchronous reluctance machine (SyRM), linear motor, magnetic levitation, model-based state-space control, flux-linkage controller, combined winding

ISBN (printed) 978-952-64-0650-3 **ISBN (pdf)** 978-952-64-0651-0

ISSN (printed) 1799-4934 **ISSN (pdf)** 1799-4942

Location of publisher Helsinki **Location of printing** Helsinki **Year** 2021

Pages 165 **urn** http://urn.fi/URN:ISBN:978-952-64-0651-0

Preface

The research work was carried out between May 2015 and May 2020 in the Electric Drives research group, Department of Electrical Engineering and Automation, Aalto University. This work has been financed by the Academy of Finland, the Doctoral Programme in Electrical Engineering of Aalto University, and the KONE Corporation. The additional financial support given by the Walter Ahlström Foundation is gratefully acknowledged.

My sincere gratitude goes to my supervisor Prof. Marko Hinkkanen for his valuable guidance and support that made this work possible, and for showing by example what it means to be a good leader and a good researcher. My warm thanks are also due to Dr. Seppo Saarakkala for his light-hearted humor and his patience while introducing me to the world of electric drives and control systems. I would also like to thank Dr. Rafał Jastrzębski for putting his trust in me and giving a much-needed kick-start to my scientific career.

Thank you to my fellow PhD students and colleagues in Aalto—Jussi Koppinen, Jarno Kukkola, Asad Awan, Waqar Khan, Mahafugur Rahman, Reza Hosseinzadeh, and others—for the good times at the lab and sharing the ups and downs of the student's life. I would very much like to thank Tero Hakala, Pasi Raassina, Tuukka Korhonen, and Seppo Suur-Askola for the fascinating discussions and their help with the experimental setup. My thanks also to the support engineers of our department—Vesa Korhonen and Ari Haavisto—who have contributed greatly to making the experimental side of this work possible.

I am very grateful to Prof. Wolfgang Gruber, Dr. Hubert Mitterhofer, and all the people I met at the Johannes Kepler University Linz and the Linz Center of Mechatronics—for their incredible hospitality and for making my research visit both productive and pleasant.

I would like to thank my family for their kind support and plentiful Skype calls that made me feel at home while being far away.

Finally, I would like to thank my wife Maria for being an immense source of love and happiness in my life.

Dedicated to my grandfather and my first power electronics teacher, Efim Havenson.

Espoo, December 15, 2021,

Maksim Sokolov

Contents

Preface **1**

Contents **3**

List of Publications **5**

Author's Contribution **7**

Abbreviations **9**

Symbols **11**

1. Introduction **15**
1.1 Background 15
1.1.1 Rotating Bearingless Motors 17
1.1.2 Linear Bearingless Motors 19
1.2 Objective and Outline of the Dissertation 20

2. System Modeling **23**
2.1 Mechanical Models 23
2.2 Space Vectors 25
2.3 Rotating SyRMs 26
2.3.1 Separated Windings 28
2.3.2 Saturation Modeling 32
2.3.3 Eccentricity Modeling 35
2.3.4 Combined Multiphase Winding 41
2.4 Linear FSPM Machines 43
2.4.1 Generic Dynamic Model 44
2.4.2 Magnetic Model and Force Production 46
2.4.3 Model Validation 48
2.4.4 Mechanical Model of a Double-Sided Linear System 51

3. Control **53**
3.1 Cascaded Control 54

3.2 Inner Control Loop: Current or Flux-Linkage Controller . 55
3.3 Reference Calculation 58
3.3.1 Rotating SyRMs 58
3.3.2 Double-Sided Linear FSPM Machines 61
3.4 Outer Control Loop 61
3.4.1 Rotation/Propulsion Control 61
3.4.2 Levitation Control 62
3.5 Pole Placement Considerations 64

4. Experimental Bearingless Setups 67
4.1 4.7-kW SyRM with Separated Windings 67
4.2 Slice SyRM with Combined Windings 69
4.3 Linear FSPM Motor System 71

5. Example Experimental Results 73
5.1 4.7-kW SyRM with Separated Windings 73
5.2 Slice SyRM with Combined Windings 74
5.3 Linear FSPM Motor System 75

6. Summary of Publications 77
6.1 Abstracts 77
6.2 Scientific Contributions 80

7. Conclusions 81

References 83

Errata 89

Publications 91

List of Publications

This thesis consists of an overview and of the following publications which are referred to in the text by their Roman numerals.

I M. Sokolov, R. P. Jastrzebski, S. E. Saarakkala, M. Hinkkanen, A. Mystkowski, J. Pyrhönen, and O. Pyrhönen. Analytical method for design and thermal evaluation of a long-term flywheel energy storage system. In *Proc. 2016 International Symposium on Power Electronics, Electrical Drives, Automation and Motion (SPEEDAM)*, pp. 270–275, Capri, Italy, June 2016.

II S. E. Saarakkala, M. Sokolov, V. Mukherjee, J. Pippuri, K. Tammi, A. Belahcen, and M. Hinkkanen. Flux-linkage model including cross-saturation for a bearingless synchronous reluctance motor. In *Proc. 15th International Symposium on Magnetic Bearings (ISMB15)*, pp. 501–508, Kitakyushu, Japan, August 2016.

III S. E. Saarakkala, M. Sokolov, M. Hinkkanen, J. Kataja, and K. Tammi. State-space flux-linkage control of bearingless synchronous reluctance motors. In *Proc. 2016 IEEE Energy Conversion Congress and Exposition (ECCE)*, 8 p., Milwaukee, WI, USA, September 2016.

IV S. E. Saarakkala, V. Mukherjee, M. Sokolov, M. Hinkkanen, and A. Belahcen. Analytical model including rotor eccentricity for bearingless synchronous reluctance motors. In *Proc. 2018 XIII International Conference on Electrical Machines (ICEM)*, pp. 1388–1394, Alexandroupoli, Greece, September 2018.

V M. Sokolov, W. Gruber, S. E. Saarakkala, and M. Hinkkanen. Modeling of a bearingless synchronous reluctance motor with combined windings. In *Proc. 2019 IEEE Energy Conversion Congress and Exposition (ECCE)*, pp. 7084–7090, Baltimore, MD, USA, September 2019.

VI S. E. Saarakkala, M. Sokolov, R. Hosseinzadeh, and M. Hinkkanen. Levitation control for a double-sided bearingless linear motor based

on feedback linearization. In *Proc. 2019 IEEE Energy Conversion Congress and Exposition (ECCE)*, pp. 4923–4930, Baltimore, MD, USA, September 2019.

VII M. Sokolov, S. E. Saarakkala, R. Hosseinzadeh, and M. Hinkkanen. A dynamic model for bearingless flux-switching permanent-magnet linear machines. *IEEE Transactions on Energy Conversion*, vol. 35, no. 3, pp. 1218–1227, September 2020.

Author's Contribution

Publication I: "Analytical method for design and thermal evaluation of a long-term flywheel energy storage system"

Maksim Sokolov developed the flywheel system design method, designed an example electrical machine, carried out the thermal performance study, and wrote the paper.

Publication II: "Flux-linkage model including cross-saturation for a bearingless synchronous reluctance motor"

Maksim Sokolov developed the lookup table-based simulation model, contributed to the processing and analysis of the FEA results, and participated in the writing of the paper.

Publication III: "State-space flux-linkage control of bearingless synchronous reluctance motors"

Maksim Sokolov developed the lookup table-based simulation model, which was used to carry out the time-domain simulations. Furthermore, he performed the literature study, and participated in the writing of the paper.

Publication IV: "Analytical model including rotor eccentricity for bearingless synchronous reluctance motors"

Maksim Sokolov conducted the original time-domain simulations and stability analysis and participated in the writing of the paper.

Publication V: "Modeling of a bearingless synchronous reluctance motor with combined windings"

Maksim Sokolov developed the proposed theory, carried out the 2D and 3D finite element analyses, implemented and tuned the control system, constructed and commissioned the experimental setup, performed the measurements, and wrote the paper.

Publication VI: "Levitation control for a double-sided bearingless linear motor based on feedback linearization"

Maksim Sokolov contributed to the lookup table-based simulation model and the development and tuning of the control system. Furthermore, he participated in the commissioning of the experimental setup, performing the experiments, recording the measurements, and writing of the paper.

Publication VII: "A dynamic model for bearingless flux-switching permanent-magnet linear machines"

Maksim Sokolov contributed to the development of the proposed model, carried out part of the FEM simulations and analyzed the FEM data, participated in the commissioning of the experimental setup and conducting the measurements, and wrote the paper.

Abbreviations

AC	Alternating current
AMB	Active magnetic bearing
DC	Direct current
DOF	Degree of freedom
DSP	Digital signal processor
EMF	Electromotive force
FEM	Finite-element method
FSPM	Flux-switching permanent-magnet
LLS	Linear least squares
MMF	Magnetomotive force
PID	Proportional integral derivative
PM	Permanent magnet
SISO	Single-input single-output
SyRM	Synchronous reluctance machine

Symbols

Matrices are denoted by boldface upper-case letters and vectors by boldface lower-case letters. Stationary-reference-frame vectors and matrices are marked with the superscript s. Reference values are marked with the subscript ref. Estimated variables are marked with a hat.

a_d, b_d	Inverse inductance d-axis coefficients
a_m, a_s, b_s, b_t	Reluctance terms of the equivalent circuit
a_p, b_c, c_c	Continuous-time levitation controller coefficients
a_q, b_q	Inverse inductance q-axis coefficients
a_z, b_z, c_z	Discrete-time levitation controller coefficients
c_dq	Inverse inductance saturation coefficient
c_m, f_m	Coefficients related to force due to the leakage fluxes
c_0	Coefficient linking the inductances to the force constants
$\boldsymbol{D}_\mathrm{m}$, $\boldsymbol{D}_\mathrm{s}$, $\boldsymbol{D}_\mathrm{M}$	Displacement dependency matrices
d_c, e_c	Continuous-time observer coefficients
d_z, e_z	Discrete-time observer coefficients
$\boldsymbol{F}^\mathrm{s}$	Radial force vector in stationary coordinates
F_x, F_y	Bearingless motor forces in stationary coordinates
F_x1, F_x2	Traction forces of individual linear machine units
F_y1, F_y2	Attraction forces of individual linear machine units
g_0	Nominal air gap of the machine
$\boldsymbol{I}$	Identity matrix $\left[\begin{smallmatrix}1 & 0\\ 0 & 1\end{smallmatrix}\right]$

i, j	Radial position in rotor coordinates
$\boldsymbol{i}$	Stator current vector in rotor coordinates
$\boldsymbol{i}^{\mathrm{s}}$	Stator current vector in stator coordinates
$\boldsymbol{i}_{\mathrm{t}}$	Torque-producing current vector in rotor coordinates
$\boldsymbol{i}_{\mathrm{f}}$	Force-producing current vector in rotor coordinates
i_α, i_β	Stator current components in stator coordinates
$i_{\mathrm{A}}, i_{\mathrm{B}}, i_{\mathrm{C}}$	Stator phase currents
$i_{\mathrm{A1}}, i_{\mathrm{B1}}, i_{\mathrm{C1}}$	Phase currents of the first star connection
$i_{\mathrm{A2}}, i_{\mathrm{B2}}, i_{\mathrm{C2}}$	Phase currents of the second star connection
$i_{\mathrm{d}}, i_{\mathrm{q}}$	Stator current components in rotor coordinates
$i_{\mathrm{fA}}, i_{\mathrm{fB}}, i_{\mathrm{fC}}$	Force components of the phase currents
$i_{\mathrm{fd}}, i_{\mathrm{fq}}$	Force-producing current components in rotor coordinates
$i'_{\mathrm{fd}}, i'_{\mathrm{fq}}$	Force-producing current components used for control
$i_{\mathrm{tA}}, i_{\mathrm{tB}}, i_{\mathrm{tC}}$	Torque components of the phase currents
$i_{\mathrm{td}}, i_{\mathrm{tq}}$	Torque-producing current components in rotor coordinates
i_{m}	Equivalent MMF of the PMs
$i_{\mathrm{m0}}, b_{\mathrm{m}}, b'_{\mathrm{m}}$	Equivalent PM MMF coefficients
$\boldsymbol{J}$	Orthogonal rotation matrix $\left[\begin{smallmatrix} 0 & -1 \\ 1 & 0 \end{smallmatrix}\right]$
J	Total moment of inertia
$\boldsymbol{K}, \boldsymbol{K}_{\mathrm{I}}, \boldsymbol{K}_{\mathrm{T}}$	Flux-linkage controller gain matrices
$K(\theta)$	Coefficient used to model the rotor saliency
$\boldsymbol{K}_{\mathrm{fb}}$	Levitation controller state-feedback gain vector
k_1, k_2, k_{I}	Levitation controller gains
$L_{\mathrm{d}}, L_{\mathrm{q}}$	Main winding direct- and quadrature-axis inductances
$L_{\mathrm{d0}}, L_{\mathrm{q0}}, L_{\mathrm{s0}}$	Self-inductances of the proposed eccentricity model
$\boldsymbol{L}_{\mathrm{m}}, \boldsymbol{L}_{\mathrm{s}}$	Main- and suspension-winding inductance matrices
$L_{\mathrm{q,0}}, a, b$	Coefficients of the q-axis inductance function
L_{s}	Suspension-winding inductance

$L_{\mathrm{s},0}$, c, d	Coefficients of the suspension-winding inductance function
l_1, l_2	State observer gains
$\boldsymbol{M}$	Radial force constant matrix
M_d, M_q	Radial force constants
$M_{\mathrm{d},0}$, e, f	Coefficients of the force-constant function
m	Rotor or mover mass
$\boldsymbol{O}$	Zero matrix $\left[\begin{smallmatrix}0 & 0\\ 0 & 0\end{smallmatrix}\right]$
p	Number of rotor pole pairs
R	Stator-winding resistance
R_m, R_s	Main- and suspension-winding resistances
s	Laplace-domain variable
T_M	Motor torque
T_s	Sampling time of the outer control loop
T_sc	Sampling time of the inner control loop
t	Time
$\boldsymbol{u}_\mathrm{f}$	Force-producing voltage vector in rotor coordinates
$\boldsymbol{u}_\mathrm{t}$	Torque-producing voltage vector in rotor coordinate
v_x, v_y	Linear velocities in stationary coordinates
W	Magnetic field energy
w_0	Magnetic field energy due to the leakage fluxes
x, y, z	Position in stationary coordinates
$\boldsymbol{x}_\mathrm{I}$	Integral state vector of the flux-linkage controller
y_1, y_2 y_3, y_4	Air gaps of individual linear machine units
z	Time-shift operator

α_c	Bandwidth of the inner control loop
Γ_d, Γ_q	Inverse inductances
γ	Rotor saliency coefficient
ΔF_y	Differential attraction force
Δy	Differential air gap
θ	Spatial angle along the air gap
ϑ_M	Mechanical angular position of the rotor
ϑ_m	Electrical angular position of the rotor
ΣF_x	Total thrust force
τ	Pole pitch of the linear machine rail
ϕ_r	PM remanent flux
ψ_d, ψ_q	Flux-linkage components in rotor coordinates
$\boldsymbol{\psi}_\mathrm{f}$	Force-producing flux-linkage vector in rotor coordinates
ψ_fd, ψ_fq	Force-producing flux-linkage components
$\boldsymbol{\psi}_\mathrm{t}$	Torque-producing flux-linkage vector in rotor coordinates
ψ_td, ψ_tq	Torque-producing flux-linkage components
ω_M	Mechanical angular speed of the rotor
ω_m	Electrical angular speed of the rotor

1. Introduction

1.1 Background

Most of the present-day electric energy conversion—be it generation or consumption—is performed by electric machines: motors and generators [1]. Electric motors are a ubiquitous feature for much of the world's population: from home appliances and air conditioning systems to electric vehicles and elevators. The industrial application of electric drives is also quite common, including, for example, gas and liquid pumps, compressors, blowers, turbines, machine tools, and robotics. The growing demand for more sustainable energy conversion has led to extensive research efforts towards increasing the energy efficiency of electric drives.

One important advantage of electric motors is reliability. However, there is one component that experiences continuous mechanical wear, which are the mechanical bearings utilized for supporting the rotating shaft. A substantial amount of electrical-machine faults are caused by failure in mechanical bearings. As such, these bearings often require maintenance, which in some applications may be rather difficult and expensive to perform and may result in equipment downtime and additional costs. Mechanical bearings can be a source of audible noise, vibrations, and additional friction losses—issues, which are usually exacerbated without proper maintenance and lubrication. In some applications (e.g., food production, chemical processing, and medical devices), the use of oil-based bearing lubricant can be an issue due to oil contamination. In heating, ventilation, and air conditioning systems, oil contamination may impede thermal transfer and result in decreased efficiency [2].

In recent years, high-speed rotating machines have been getting increased attention in, e.g., compressors, turbines, turbomolecular pumps, blowers, spindles, and flywheels energy storage systems. For the same power rating, a high-speed motor can be smaller and, thus, achieve higher power densities and have a more efficient material utilization. Moreover,

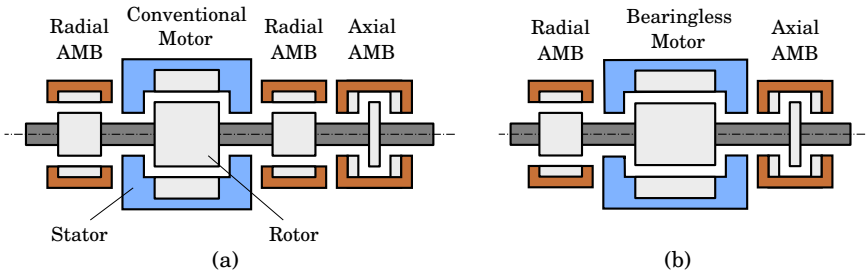

Figure 1.1. Comparison of magnetically levitated drive systems supported by (a) AMBs and (b) a bearingless motor in conjunction with AMBs.

a direct-drive solution eliminates the need for mechanical transmission elements and improves reliability. However, bearings are often a limiting factor in high-speed applications. The expected lifetime of a conventional bearing is roughly inversely proportional to the rotational speed and the load of the motor shaft [3]. For example, in modern exhaust gas turbochargers, the shaft reaches rotational speeds of up to 300 000 r/min. In this application, roller bearings are responsible, along with their lubrication, for up to approximately 80% of system failures [4].

One attractive alternative to mechanical bearings is a magnetic suspension. In rotating machinery, active magnetic bearings (AMBs) are the most represented technology that utilizes magnetic levitation. An AMB consists of an electromagnetic force actuator supplied by a power amplifier, which is actively controlled based on the rotor position feedback. By adding a negative feedback control system, the AMB generates forces that are able to support the weight of the shaft, reject external disturbances, and result in a stable, contact-free levitation. For example, Fig. 1.1(a) shows a typical arrangement of AMBs required for a complete levitation of a rotating shaft in five degrees-of-freedom (DOF). Two radial AMBs and an axial AMB are required to support the shaft. A conventional electric motor is used for torque production. However, the drawbacks of AMBs are mainly due to their high cost, complexity, and size. This arrangement also requires a substantial amount of power electronics to supply the active components. Systems with AMBs also necessitate an increased shaft length, which leads to a reduced critical speed of the machine.

One step towards a more integrated solution involves combining the functions of an AMB together with an electric machine. Such an electric machine that can simultaneously generate both the driving torque and controlled radial force for levitation is called a bearingless machine. The name self-bearing motor also appears in the literature. Other less common terminologies include levitated motor, floating actuator, and integrated or combined motor bearing.

Fig. 1.1(b) illustrates a magnetically levitated system where the function of one radial AMB is performed by the bearingless motor. The benefits of

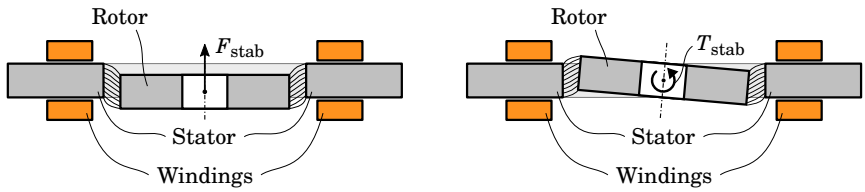

(a) Axial displacement example (b) Tilting example

Figure 1.2. Example of a fully levitating bearingless slice motor. Axial displacement and tilting are passively stabilized by the axial force F_{stab} and torque T_{stab}.

this arrangement include a shorter shaft and fewer power semiconductor devices required for the supplying power electronics. Bearingless motors can typically achieve a higher force production capability than that of AMBs, due to a larger active surface area [5]. The higher level of mechanical integration results in the drive system being easier to assemble, design, and service. Moreover, less coils need to be wound during the manufacturing process. Finally, bearingless machines can be supplied by widely available three-phase inverters, while AMBs usually require custom power electronics.

Apart from the applications where a bearingless machine can replace one or more of the AMBs, there are also bearingless topologies that offer completely contactless operation without the need for additional AMBs. One noteworthy example of such a topology is a so-called bearingless slice motor [6]. The name comes from the fact that such motors have a disc-shaped rotor with a small ratio of axial length to diameter. This allows the air-gap fields to passively stabilize the rotor's tilting and axial degrees of freedom, as shown in Fig. 1.2. Only the rotation and radial movements then require active control [7]. Bearingless slice motors have garnered commercial interest in centrifugal pumps and mixing devices for semiconductor manufacturing, bioreactors, and medical applications [8].

1.1.1 Rotating Bearingless Motors

For a rotating bearingless machine, the basic principle is disrupting the p pole-pair field in the air gap with a $p \pm 1$ pole-pair field. The concept was first introduced in the 1970s in [9] and [10]. However, the possibility for further development only appeared in the 1980s with the ability to apply modern power electronics, digital signal processors, and field-oriented control theory. To the best of the author's knowledge, the term "bearingless motor" was first utilized in 1988 in a conference paper [11]. The recent advancements in the field of bearingless motors are nicely summarized in a number of review papers [12], [13], and [14].

Many different types of bearingless motors have been presented in the

literature over the years. Permanent magnet (PM) machines have been a popular bearingless machine type, especially in the category of slice motors. Bearingless induction machines have also received a considerable amount of attention, usually for high power applications [12]. Less attention has been given to switched reluctance, synchronous reluctance, homopolar, and other bearingless machine types.

Conventional synchronous reluctance machines (SyRMs) have recently received increased attention and are successfully competing with induction motors in terms of efficiency, torque-per-ampere ratio, and power density [15], [16]. The performance of PM machines is usually superior to that of SyRMs, specifically with regards to the power factor and power density. However, machines without PMs have inherent advantages, such as lower cost, easily adjustable excitation, higher temperature tolerance, and no risk of demagnetization. Typically, SyRMs have not been considered for use as high-speed machines due to insufficient rotor robustness. However, recent developments suggest that both transversally laminated machines [17], [18] as well as solid rotor construction machines [19], [20] can be suitable in certain high-speed applications.

In the category of rotating bearingless machines, the scope of this dissertation is limited to the SyRM topology. In bearingless SyRMs, the required p and $p \pm 1$ pole-pair fields can be generated using different winding concepts. These concepts can be broadly divided into two major categories: separated windings and combined windings.

Separated Windings

Separated windings is the oldest and most common winding type in bearingless machines [21], [14]. For this winding type, the fundamentals of field-oriented vector control and the decoupling of the torque and force production were developed in [22] and [23].

In this approach, two physically separate winding sets are placed into the stator slots and are fed by separate inverters. This winding type features a simple selection of currents for independent torque and force production and is suitable for high rotation speeds, since the suspension winding does not experience the rotation-induced back electromotive force (EMF). However, installing two windings in the stator slots results in a more difficult manufacturing process. Another disadvantage of this winding type is the inefficient use of the slot space, as part of the slot is occupied by the suspension winding conductors and cannot be used for producing torque.

Combined Windings

The term "combined winding" denotes the combining of the torque and force production within one winding system. There are several combined winding approaches, which all share a common feature—being able to utilize all of the stator slot space for both the torque and the radial force

production. This reduces the copper losses [7] and allows the control system to dynamically allocate the winding for torque-producing current or force-producing current, depending on the requirements of the situation. However, these windings require a modified control scheme to select proper current references and decouple the torque and force production.

Combined multiphase winding utilizes multiple phases to simultaneously generate two magnetic fields with different numbers of pole pairs. It is also referred to as "split winding" in [5], [24], [25] or "divided winding" in [26], [27]. This winding type is first described in [10]. The multiphase winding can have one neutral point or two separate neutral points. Combined multiphase winding is often used in low-power bearingless slice motors [14]. The main advantages of a multiphase winding are in the effective utilization of copper and simpler manufacturing. However, in this winding configuration, the rotation back-EMF lowers the voltage available for controlling the force production, which negatively affects the levitation control performance at higher speeds [28].

A solution to the back-EMF-related issues has been proposed with so-called "no-voltage winding" [29]. The name comes from the fact that there is no back-EMF voltage visible from the suspension inverter terminals. No-voltage windings can be realized with either a bridge winding configuration [30], [31] or with parallel windings [32]. These approaches merge the advantages of the separated windings and the combined multiphase windings. However, it introduces more complexity in the required power electronics [33].

The scope of this dissertation includes rotating bearingless SyRMs with separated windings and with combined multiphase windings.

1.1.2 Linear Bearingless Motors

The bearingless concept is also applicable in linear machines. Linear levitation systems have been successfully utilized in magnetic levitation (Maglev) train systems for many years. However, in Maglevs, the levitation system is usually separate from the propulsion system [34]. A linear bearingless machine system combines both functions in the same magnetic circuit. This can be achieved by exploiting the fact that in addition to the desired thrust force, linear machines always produce an attraction force between the rail and the mover. When a pair of linear motor units is placed opposite each other with their rails mechanically fixed together, it becomes possible to produce a net normal force in both directions by controlling the attraction force of each motor unit. Levitation can be achieved by active control of the net normal force based on the air-gap feedback. At the same time, both motor units can contribute to the required thrust force production.

Fig. 1.3 shows an example configuration that is able to provide active levitation in four DOF while also producing thrust force in the x-direction.

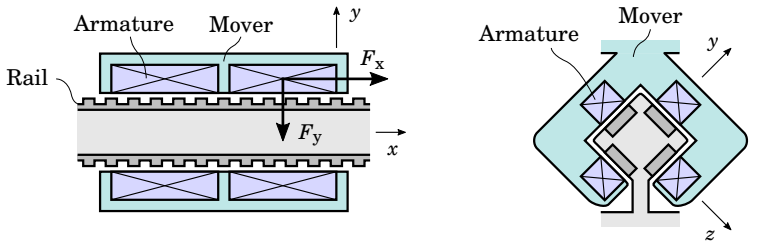

Figure 1.3. Example of a linear bearingless system. The four-sided configuration allows the mover assembly to maintain active levitation in four DOF by controlling the normal forces F_y of each machine unit. Each machine unit also produces thrust force F_x for propulsion in the x-direction.

Eight motor units have their mover parts attached together in a four-sided configuration around the rail. The directions of the thrust force F_x and the normal force F_y are shown for one machine unit.

Different linear machine types can be utilized in a linear bearingless system. For long-stroke applications, such as urban rail transit or ropeless elevator systems, an important factor is the complexity and price of manufacturing a long rail. A flux-switching permanent-magnet (FSPM) machine has neither windings nor PMs on the rail side. On that side, electrical steel is the only active material required, while both windings and PMs are placed in a relatively short mover. In addition, this machine type features comparatively high power density and close to sinusoidal back-EMF voltages. The scope of this dissertation includes linear bearingless FSPM machines.

1.2 Objective and Outline of the Dissertation

Bearingless machines offer advantages in a high level of integration. However, this comes at the price of a high degree of complexity in designing, modeling, and controlling such systems. An inherently unstable nature, magnetic cross-coupling, air gap variation, and nonlinear effects contribute to the technical challenges of implementing bearingless systems. Efficient and reliable control requires accurate knowledge of the machine behavior in all possible operating points. This fact makes mathematical machine models an important tool for control system design, estimation purposes, time-domain simulations, and robustness analyses.

Consequently, the aim of this dissertation is to develop dynamic models and model-based control systems for bearingless SyRMs and linear bearingless FSPM machines. The development of the dynamic models is focused on the following points:

- Proper modeling of the cross-coupling effects between the motoring and levitation functions.

- Modeling of nonlinear effects due to magnetic saturation. SyRMs and FSPM machines are often operated in the nonlinear region of the BH curve. If not taken into account, the effect of saturation causes the machine to behave inconsistently throughout its operating range.
- Proper modeling of air gap variation. Air gap variation in bearingless machines is a common phenomenon at lift-up or during operation, e.g., due to mass imbalance or bending modes of the rotor. An unaccounted for inductance change and unbalanced magnetic pull (UMP) due to air gap variation can deteriorate the performance of the model-based control systems and even lead to instability in the worst case scenario.
- Developed models should be general enough to be applicable to various machine designs, be physically consistent, and represent the actual machine accurately enough for control design purposes.
- The models are developed based on the machine analysis through finite-element method (FEM) simulations.

The proposed modeling methods are utilized as a basis for the contributions in control design. The control system development in this dissertation focuses on model-based control methods. State-feedback controllers are developed for both the inner and outer control loops. Proper controller tuning is a topic that is not extensively covered in the literature. Often, tuning is performed using trial-and-error methods, while improper tuning of the feedback controller may result in poor performance or levitation instability. In this dissertation, analytical tuning rules for each developed controller are given.

The dissertation consists of an overview and seven publications. The goal of the overview is to outline an overall perspective on modeling and control of bearingless SyRM and FSPM linear machines and to briefly present the most important contributions of the publications. Chapter 2 reviews the mathematical dynamic models of the considered bearingless machines. Chapter 3 presents the design of the model-based cascaded control system, discusses pole placement considerations, and presents experimental levitation control results. Chapter 4 describes the experimental setups applied for testing. Chapter 5 shows example experimental results of active levitation control. New experimental results which have not been previously published are also presented[1]. Chapter 6 presents the abstracts of the publications and a summary of the scientific contributions of this dissertation. Chapter 7 provides some concluding remarks. Finally, the publications included in this dissertation are reprinted at the end.

[1]Due to time limitations, these experimental results have not been included in the enclosed publications, but the related modeling and control contributions have been.

2. System Modeling

This chapter focuses on the mathematical models of bearingless machines. The main purpose of the modeling approaches discussed here is to be applicable in control design.

These models can be broadly divided into two categories: the mechanical subsystem and the electromagnetic subsystem. The main focus of the dissertation is related to the modeling of the electromagnetic phenomena. Section 2.1 presents mechanical modeling and outlines a simple mechanical model used for all machines throughout the dissertation. Sections 2.2, 2.3, and 2.4 focus on the modeling of electromagnetic phenomena, including electrical dynamics, saturation characteristics, displacement modeling, and force production principles.

Two bearingless machine types are in the scope of this dissertation: rotating SyRMs (with separated and combined windings) and linear FSPM machines. First, the common aspects of both machine types are discussed.

2.1 Mechanical Models

The mechanical models of rotating and linear machines are shown in Fig. 2.1. The mechanical movement of the rotor (or mover in the case of linear machines) is modeled throughout the dissertation using a single-mass model. This assumes a rigid structure with no elasticity and no bending. Another assumption is that there is no cross-coupling between the controllable mechanical degrees of freedom. This means that in rotating machines, the rotation of the shaft and the displacements in the x- and y-axes are decoupled mechanical states. In linear machines, this means that the thrust (x-axis) and normal (y-axis) direction movements are independent of each other. Therefore, equations describing the displacement dynamics can be derived from Newton's second law of motion:

$$m\frac{\mathrm{d}v_\mathrm{x}}{\mathrm{d}t} = F_\mathrm{x} + F_\mathrm{x,d} \qquad \frac{\mathrm{d}x}{\mathrm{d}t} = v_\mathrm{x} \tag{2.1}$$

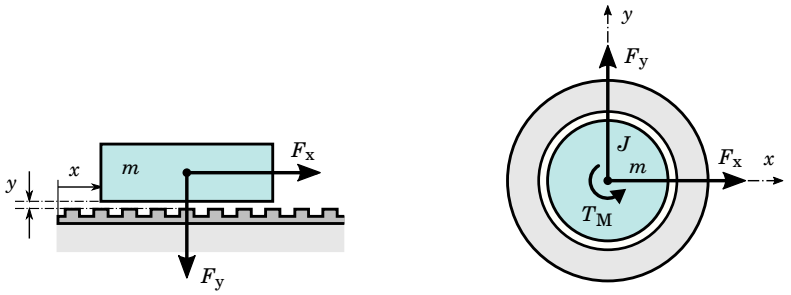

Figure 2.1. Single-mass model of the generic (a) linear and (b) rotating bearingless machines. Coordinate systems and mechanical degrees of freedom are shown.

$$m\frac{\mathrm{d}v_\mathrm{y}}{\mathrm{d}t} = F_\mathrm{y} + F_\mathrm{y,d} \qquad \frac{\mathrm{d}y}{\mathrm{d}t} = v_\mathrm{y} \tag{2.2}$$

where m is the total mass of the rotor; F_x and F_y are the forces generated by the bearingless motor; $F_\mathrm{x,d}$ and $F_\mathrm{y,d}$ are the external disturbance forces, e.g., gravity; and v_x and v_y are the linear velocities. As a side note, the forces F_x and F_y typically change as a function of the x and y displacement in a way that makes the electromechanical system open-loop unstable. Moreover, the force expressions are often nonlinear.

For rotating machines, the rotational dynamics are given as follows:

$$J\frac{\mathrm{d}\omega_\mathrm{M}}{\mathrm{d}t} = T_\mathrm{M} - T_\mathrm{L} \qquad \frac{\mathrm{d}\vartheta_\mathrm{M}}{\mathrm{d}t} = \omega_\mathrm{M} \tag{2.3}$$

where J is the total moment of inertia; ϑ_M is the angular position of the shaft; ω_M is the angular speed of the motor; T_M is the motor torque; and T_L is the load torque.

The mechanical model for linear bearingless machines is described by equations (2.1) and (2.2). Equations (2.1), (2.2), and (2.3) describe the mechanical model for rotating bearingless machines. These models are used as a basis for designing and tuning the levitation and rotation control loops in Chapter 3. However, the described single-mass model leaves out some important phenomena, that are worth keeping in mind:

- When rotating machines are considered in three dimensions, there is a cross-coupling between the tilting around the x and y axes due to the gyroscopic effect [5]. This effect becomes more important at high rotation speeds and with high rotor inertia, for example, in the case of a disk-shaped rotor or a flywheel.

- Every real-world rotor has some degree of imbalance due to the manufacturing tolerances. Such mass imbalance produces a disturbance with a frequency proportional to the rotation speed ω_M and an amplitude proportional to ω_M^2 [35]. Proper modeling and compensation of this disturbance can help reduce the rotor orbit during operation.

- In high-speed applications, the rotation speed may approach and even surpass the critical speed of the rotor. Such cases require higher fidelity models that include rotor flexing and can predict the bending modes of the system [36].
- Rotational dynamics can vary between different applications and depend on the driven load. To take into account more complex rotational mechanics, bearingless motors can make use of the same modeling approaches as the conventional electric motors, e.g., modeling torsional dynamics [35] or a multi-mass system [37].
- In real linear bearingless systems, the rail and the mover are not perfectly rigid. Due to high attraction forces between the rail and the mover, bending of either can occur and introduce resonant frequencies. Knowing these frequencies is important in order to design the controllers in a way that does not excite resonances.

2.2 Space Vectors

Real space vectors are used throughout the dissertation as a basis for the electrical machine analysis. Boldface lowercase letters are used to denote vector quantities, and boldface uppercase letters are used to denote matrices.

SyRMs and FSPM machines with three-phase winding systems are studied in this dissertation. The three-phase winding is either delta-connected or star-connected without a neutral wire. Therefore, the zero-sequence component is absent, and the three-phase system can be represented with an equivalent $\alpha\beta$ model. For example, the three-phase currents i_A, i_B, and i_C can be transformed into the $\alpha\beta$ components using the Clarke transformation:

$$\boldsymbol{i}^\mathrm{s} = \begin{bmatrix} i_\alpha \\ i_\beta \end{bmatrix} = \begin{bmatrix} \frac{2}{3} & -\frac{1}{3} & -\frac{1}{3} \\ 0 & \frac{1}{\sqrt{3}} & -\frac{1}{\sqrt{3}} \end{bmatrix} \begin{bmatrix} i_\mathrm{A} \\ i_\mathrm{B} \\ i_\mathrm{C} \end{bmatrix} \tag{2.4}$$

where the superscript s denotes the vector in stator coordinates with the orthogonal components α and β. The space vectors for the voltages and the flux linkages are defined similarly.

Electrical machines are often analyzed in the rotating coordinate system, since the sinusoidally varying quantities in stator coordinates become DC quantities in rotor coordinates.

In bearingless machines, magnetic fields with different numbers of pole pairs may be present in the machine at the same time. Hence, the vectors in stator coordinates are transformed into the rotor coordinates by rotating

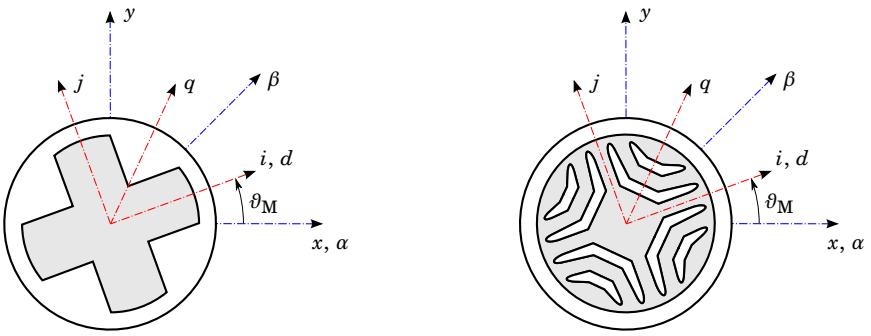

Figure 2.2. Coordinate systems of a bearingless SyRM and the reluctance rotor construction: (a) with salient poles and (b) with multiple flux barriers. Stator coordinates are denoted with blue lines, and rotor coordinates are denoted with red lines.

them with the electrical angle $\vartheta_\mathrm{m} = p\vartheta_\mathrm{M}$, where p is the number of pole pairs. This means that the resulting vectors are rotating synchronously with their respective fields. For example, the current components can be transformed into the rotor coordinates using

$$\boldsymbol{i} = \begin{bmatrix} i_\mathrm{d} \\ i_\mathrm{q} \end{bmatrix} = \mathrm{e}^{-\vartheta_\mathrm{m}\boldsymbol{J}} \boldsymbol{i}^\mathrm{s} = \begin{bmatrix} \cos(\vartheta_\mathrm{m}) & \sin(\vartheta_\mathrm{m}) \\ -\sin(\vartheta_\mathrm{m}) & \cos(\vartheta_\mathrm{m}) \end{bmatrix} \begin{bmatrix} i_\alpha \\ i_\beta \end{bmatrix} \tag{2.5}$$

where $\boldsymbol{J} = \left[\begin{smallmatrix} 0 & -1 \\ 1 & 0 \end{smallmatrix}\right]$ is the orthogonal rotation matrix. Vectors in rotor coordinates are denoted with no superscript and have d and q orthogonal components. Similar transformations can be applied to the flux linkages and the voltages. For linear machines, the same transformations apply. In linear machines, ϑ_m depends on the thrust-direction position x as $\vartheta_\mathrm{m} = 2\pi x/\tau$, where τ is the pole pitch of the rail.

For machines with a sinusoidal magnetomotive force (MMF) distribution in the air gap, applying the dq model makes flux linkages and inductances appear constant during steady-state operation. For well-designed SyRMs and FSPM machines, it is a reasonable assumption [38], [39]. However, it is worth noting that in real-world machines, the MMF distribution always differs to some degree from a perfect sine wave. The resulting spatial harmonics can cause torque and force ripple, which may require additional compensation. Machine-specific modeling is discussed in the following sections.

2.3 Rotating SyRMs

A synchronous reluctance machine is an alternating-current (AC) machine that has neither PMs nor conductors in the rotor and relies only on the magnetic saliency of the rotor to produce torque. Two typical reluctance

rotors are shown in Fig. 2.2: one with salient-pole construction and one with internal flux barriers. SyRMs feature an inexpensive rotor construction, high efficiency, and comparatively high torque density, although they generally have a lower power factor as compared to PM machines [40].

One of the attractive application areas of bearingless SyRMs is flywheel energy storage. Here, an important advantage of SyRMs as compared to PM machines is the ability to turn off the field completely, which eliminates the idling losses [41]. Recent developments in composite materials have allowed allowed for an increase in the energy density of the flywheels. A composite rotor is able to withstand high centrifugal stress and, thus, can reach high rotation speeds. The kinetic rotation energy is given as $W_{kin} = \frac{1}{2} J \omega_{\mathrm{M}}^2$, which makes it easy to see why increasing the rotation speed ω_{M} has a significant contribution to the amount of stored energy. This fact motivated the development of high-speed flywheels with rotation speeds from 10000 to 100000 r/min [42]. High rotation speed requires solving challenges related to the lifetime of bearings [43]

Publication I studies the thermal performance of a flywheel energy storage system. The ability of the electrical machine rotor to withstand high temperatures as well as low rotor losses are important aspects in this application, which makes the bearingless SyRM an attractive solution [44].

In the literature, bearingless SyRMs were first introduced in the beginning of the 1990s with [45], [46]. Numerous papers on the topic have been published since, but bearingless SyRMs have received less attention as compared to the surface-mounted PM or induction machine types [12]. A slice motor version of the bearingless SyRM was first studied in [47] and showed comparable performance to other slice motor types.

The coordinate systems used for modeling the bearingless SyRMs are shown in Fig. 2.2. The machines with two-pole-pair rotors are given as an example, but the same basic principles apply for other pole-pair numbers. The mechanical quantities are described in xy coordinates in the stator reference frame and in ij coordinates in the rotor reference frame. Three-phase electrical quantities are modeled in $\alpha\beta$ and dq coordinates for the stator and rotor reference frames, respectively. The rotor d-axis in SyRMs is aligned with the path of lowest reluctance.

Bearingless operation with SyRMs is achieved by having the winding system produce a p and $p \pm 1$ pole-pair fields in the air gap. The p pole-pair field corresponds to the number of rotor pole pairs and is used for generating torque, and a $p \pm 1$ pole-pair field is used for generating the radial suspension force.

Fig. 2.3 illustrates the principle of torque and force production. As an example, a SyRM with a four-pole rotor is considered. The current vector $\boldsymbol{i}_{\mathrm{t}}$ generates the four-pole field (shown in red), which is used for torque production. In the case shown in Fig. 2.3, $\boldsymbol{i}_{\mathrm{t}}$ is aligned with the d-axis,

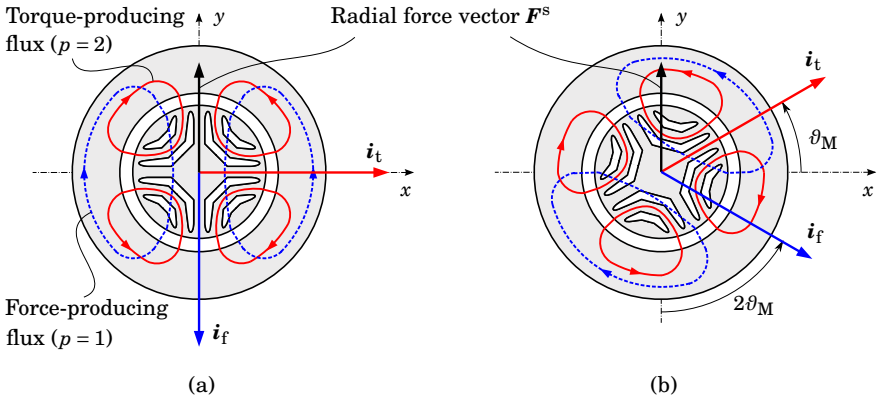

Figure 2.3. Principle of torque and force production in an example bearingless SyRM. The current vector $\boldsymbol{i}_{\mathrm{t}}$ that generates the torque-producing flux is shown in red, and $\boldsymbol{i}_{\mathrm{f}}$ that generates the force-producing flux is shown in blue. The current vectors are adjusted such that the resulting force vector $\boldsymbol{F}^{\mathrm{s}}$ is constant, while the rotor is (a) at 0 angle and (b) rotated by ϑ_{M}.

which magnetizes the machine while not generating torque. It is important to note that a non-zero magnetization is necessary to generate the radial force because it acts as a bias flux in the air gap in which the unbalance can be generated. This unbalance in the four-pole flux is generated by the two-pole flux (shown in blue). The two-pole flux can be seen to strengthen the four-pole flux in the upper section of the machine while weakening it in the lower section. This results in a magnetic pull on the rotor, generated in the upwards direction, denoted with the force vector $\boldsymbol{F}^{\mathrm{s}}$. For bearingless motor operation, the current vectors $\boldsymbol{i}_{\mathrm{t}}$ and $\boldsymbol{i}_{\mathrm{f}}$ can be adjusted to generate the required torque and force at any rotor angle. Fig. 2.3(b) shows that when the rotor is rotated by the angle ϑ_{M}, the current vector $\boldsymbol{i}_{\mathrm{t}}$ has to be rotated synchronously with the rotor in order to keep the same torque production and magnetization level, while the current vector $\boldsymbol{i}_{\mathrm{f}}$ has to be rotated by $2\vartheta_{\mathrm{M}}$ in order to produce the same force vector $\boldsymbol{F}^{\mathrm{s}}$.

In order to generate the two magnetic fields required for the torque and force production, different winding concepts can be used, as introduced in Section 1.1. In the scope of this dissertation are bearingless SyRMs with separated windings and with combined multiphase windings. The proposed modeling approaches are presented for the machines with four-pole main and two-pole suspension fields, but they can be easily extended to machines with other numbers of poles.

2.3.1 Separated Windings

In this winding concept, two three-phase windings are placed separately into the stator slots. The main winding carries the torque-producing current $\boldsymbol{i}_{\mathrm{t}}$, while the suspension winding carries the force-producing current $\boldsymbol{i}_{\mathrm{f}}$. The number of pole pairs of the main winding p equals the number of pole

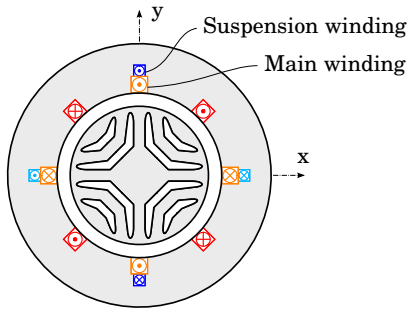

Figure 2.4. Example of a three-phase bearingless SyRM with separated windings, shown with equivalent two-phase windings. Each phase winding is sinusoidally distributed along the air gap, while only the center of the conductors is shown. Crosses and dots denote the positive direction of the current.

pairs of the reluctance rotor, while the suspension winding is designed with $p \pm 1$ pole pairs. An example bearingless SyRM with a four-pole main winding and a two-pole suspension winding is shown in Fig. 2.4. Three-phase windings are modeled with equivalent two-phase windings.

The most widely acknowledged textbook model of bearingless SyRMs with separated windings is presented in [5] and [48]. The model is described below and is considered to be a baseline for further development.

Currents, flux linkages, and voltages are transformed into synchronous coordinates using (2.4) and (2.5). The electrical angle is used in the transformations, which is $\vartheta_\mathrm{m} = 2\vartheta_\mathrm{M}$ for main-winding-related values, and $\vartheta_\mathrm{m} = \vartheta_\mathrm{M}$ for suspension-winding-related values. In synchronous coordinates, the voltage equations of the main winding and the suspension winding are given as follows

$$\frac{\mathrm{d}\boldsymbol{\psi}_\mathrm{t}}{\mathrm{d}t} = \boldsymbol{u}_\mathrm{t} - R_\mathrm{m}\boldsymbol{i}_\mathrm{t} - 2\omega_\mathrm{M}\boldsymbol{J}\boldsymbol{\psi}_\mathrm{t} \tag{2.6a}$$

$$\frac{\mathrm{d}\boldsymbol{\psi}_\mathrm{f}}{\mathrm{d}t} = \boldsymbol{u}_\mathrm{f} - R_\mathrm{s}\boldsymbol{i}_\mathrm{f} - \omega_\mathrm{M}\boldsymbol{J}\boldsymbol{\psi}_\mathrm{f} \tag{2.6b}$$

where R_m and R_s are main winding and suspension winding resistances, and voltage vectors are defined as $\boldsymbol{u}_\mathrm{t} = \begin{bmatrix} u_\mathrm{td} & u_\mathrm{tq} \end{bmatrix}^\mathrm{T}$ and $\boldsymbol{u}_\mathrm{f} = \begin{bmatrix} u_\mathrm{fd} & u_\mathrm{fq} \end{bmatrix}^\mathrm{T}$. The current vectors and the flux-linkage vectors are defined similarly. Linear magnetics are assumed, and the flux linkages of the main winding $\boldsymbol{\psi}_\mathrm{t}$ and the suspension winding $\boldsymbol{\psi}_\mathrm{f}$ are

$$\underbrace{\begin{bmatrix} \boldsymbol{\psi}_\mathrm{t} \\ \boldsymbol{\psi}_\mathrm{f} \end{bmatrix}}_{\boldsymbol{\psi}} = \underbrace{\begin{bmatrix} \boldsymbol{L}_\mathrm{m} & \boldsymbol{M} \\ \boldsymbol{M}^\mathrm{T} & \boldsymbol{L}_\mathrm{s} \end{bmatrix}}_{\boldsymbol{L}_\Sigma} \underbrace{\begin{bmatrix} \boldsymbol{i}_\mathrm{t} \\ \boldsymbol{i}_\mathrm{f} \end{bmatrix}}_{\boldsymbol{i}} \tag{2.7}$$

with the inductance matrices given as

$$\boldsymbol{L}_\mathrm{m} = \begin{bmatrix} L_\mathrm{d} & 0 \\ 0 & L_\mathrm{q} \end{bmatrix}, \quad \boldsymbol{L}_\mathrm{s} = \begin{bmatrix} L_\mathrm{s} & 0 \\ 0 & L_\mathrm{s} \end{bmatrix}, \quad \boldsymbol{M} = \begin{bmatrix} M_\mathrm{d} i & -M_\mathrm{d} j \\ M_\mathrm{q} j & M_\mathrm{q} i \end{bmatrix} \tag{2.8}$$

where L_d, L_q are the main winding d- and q-channel inductances; L_s is the suspension-winding inductance; and M_d and M_q are radial-force constants (H/m). The radial-force vector in stationary xy coordinates is defined as

$$\boldsymbol{F}^\mathrm{s} = \begin{bmatrix} F_\mathrm{x} \\ F_\mathrm{y} \end{bmatrix} = \mathrm{e}^{\vartheta_\mathrm{M}\boldsymbol{J}} \begin{bmatrix} M_\mathrm{d} i_\mathrm{td} & M_\mathrm{q} i_\mathrm{tq} \\ M_\mathrm{q} i_\mathrm{tq} & -M_\mathrm{d} i_\mathrm{td} \end{bmatrix} \boldsymbol{i}_\mathrm{f} \tag{2.9}$$

It can be seen in the equation above that because of saliency the force production is coupled with the torque production due to the terms $M_\mathrm{q} i_\mathrm{tq}$. This somewhat complicates the control system design, as compared to the non-salient machines. The electromagnetic torque is defined in the same way as for the conventional SyRMs

$$T_\mathrm{M} = 3(\psi_\mathrm{td} i_\mathrm{tq} - \psi_\mathrm{tq} i_\mathrm{td}) = 3(L_\mathrm{d} - L_\mathrm{q}) i_\mathrm{td} i_\mathrm{tq} \tag{2.10}$$

The flux produced by the suspension winding can also influence the torque production, but this effect is usually neglected.

The textbook model presented above has the following limitations:

- The inductances are derived by first approximating the inverse air-gap length of an eccentric rotor with a series expansion of cosine function and using it further to define the permeance function of the air gap. Only the first term is included in the series expansion; hence, the obtained analytical small-signal model is valid only in the vicinity of the centric operating point.
- Since the inductances have no dependency on the rotor displacement, the UMP is not included in the model.
- The model assumes no cross-coupling between the main and suspension windings when the rotor is centric, since the cross-coupling term appears in (2.8) only when i and j are non-zero.
- Assuming constant M_d and M_q results in a linear force/current relationship, which may not be the case in a real motor due to saturation.
- The assumption of linear magnetics results in neglecting the self-saturation and the cross-saturation between the main and suspension windings.

To introduce the UMP into the model, [5] proposes to model the inductance variation due to the rotor radial displacement with additional second-order equations. However, this adds complexity to the model and requires tuning of additional unbalanced pull coefficients. Moreover, this method does not guarantee that the power balance is respected in the model.

In [49], analytical inductance models including rotor saliency and eccentricity are derived. The saliency of the rotor is taken into account by using

a piecewise defined inverse air gap length, making it a more elaborate way to derive the inductances. However, only the first term is included in the series expansion, resulting in an inaccurate approximation when using the model to predict the UMP.

In [50], the saturation effects coming from the motor currents are investigated. Variation in force constants due to the changing i_{tq} were taken into account in the control system by using a decoupling compensator. In [51] the saturation is taken into account using a simple magnetic model and measured magnetization curve. However, both of these works do not propose appropriate changes to the dynamic motor model and lack a method for quantifying the saturation effects.

In [52], a model order reduction method based on orthogonal interpolation is used to model a bearingless SyRM including saturation and eccentricity. However, the study does not discuss the implications of the saturation and eccentricity as they relate to modeling and control design. In addition, the method is not suitable to be generalized for different motor designs.

Publication II investigates the magnetic saturation phenomena using the FEM and proposes an explicit-function-based magnetic model for bearingless SyRMs. The saturation characteristics are analyzed in more detail than in the previous studies, including self-saturation and cross-saturation. Suitable explicit functions are proposed to model the most notable dependencies. Additionally, current controllers based on explicit-function and constant parameters are compared using time-domain simulations.

Publication IV investigates the rotor eccentricity-related phenomena and proposes an improved dynamic model that more accurately represents eccentric operation. The model is based on the inverse air gap length approximation and takes the rotor saliency into account. The proposed model includes more terms in the series expansion, which allows it to inherently include the UMP effect in the calculated radial forces. The model is compared against the FEM results and against the textbook model. A straightforward linear least squares (LLS) fitting method to obtain the parameter values of the proposed model is also presented. Parameterizing the proposed model requires no radial force data, since the model predicts the radial forces by using the magnetic circuit parameters as a basis.

The proposed saturation modeling and eccentricity modeling approaches are considered separately, i.e., a modeling approach combining both phenomena at once is left for future research. The contributions to saturation and eccentricity modeling from Publication II and Publication IV are briefly reviewed in the following subsections.

2.3.2 Saturation Modeling

Instead of assuming a linear magnetic circuit as in (2.8), the flux linkages are modeled as a function of currents

$$\boldsymbol{\psi}(\boldsymbol{i}) = \begin{bmatrix} \boldsymbol{\psi}_\mathrm{t}(\boldsymbol{i}_\mathrm{t}, \boldsymbol{i}_\mathrm{f}) \\ \boldsymbol{\psi}_\mathrm{f}(\boldsymbol{i}_\mathrm{t}, \boldsymbol{i}_\mathrm{f}) \end{bmatrix} = \begin{bmatrix} \psi_\mathrm{td}(i_\mathrm{td}, i_\mathrm{tq}, i_\mathrm{fd}, i_\mathrm{fq}) \\ \psi_\mathrm{tq}(i_\mathrm{td}, i_\mathrm{tq}, i_\mathrm{fd}, i_\mathrm{fq}) \\ \psi_\mathrm{fd}(i_\mathrm{td}, i_\mathrm{tq}, i_\mathrm{fd}, i_\mathrm{fq}) \\ \psi_\mathrm{fq}(i_\mathrm{td}, i_\mathrm{tq}, i_\mathrm{fd}, i_\mathrm{fq}) \end{bmatrix} \tag{2.11}$$

The model assumes a lossless magnetic field and omits spatial harmonics. Hence the model does not include dependencies on rotor speed or angular position. The functions in (2.11) can be characterized using the FEM. A set of static FEM simulations is performed, which covers the entire possible operating range of the machine in terms of allowable currents.

Each simulation is characterized by the supplied current combination $(i_\mathrm{td}, i_\mathrm{tq}, i_\mathrm{fd}, i_\mathrm{fq})$. Operating points are pre-defined by changing the currents one by one in fixed steps to cover the entire possible operating range of the machine. The rotor is kept centric and at zero angle in order to leave out the phenomena related to the eccentricity and spatial harmonics. From the resulting magnetic field solutions, the flux linkages $(\psi_\mathrm{td}, \psi_\mathrm{tq}, \psi_\mathrm{fd}, \psi_\mathrm{fq})$ as well as the radial forces F_x, F_y and torque T_M are calculated.

A set of 2D magnetostatic FEM simulations in 9000 pre-defined operating points was carried out for an example 4.7-kW bearingless SyRM. The FEM simulations were carried out using COMSOL Multiphysics software. Details of the studied machine design are presented in Section 4.1. Selected dependencies based on the FEM results are presented with 3D plots in Fig. 2.5.

Influence of the Main-Winding Current

The effects of the main-winding current components i_td, i_tq are demonstrated in Figs. 2.5(a–d). The d-channel of the main winding shows neither the self-saturation nor the cross-saturation, as can be seen in Fig. 2.5(a). L_d shows less than 6% variation throughout the whole operating region and, thus, can be considered to be constant. However, in the q-channel, clear self-saturation can be seen between i_tq and ψ_tq, shown in Fig. 2.5(b). Self-saturation in the q-channel is due to the thin iron flux bridges in the rotor, which saturate already at low values of i_tq. The lack of magnetic saturation in the d-channel in this example SyRM is due to a rather large air-gap length of 1 mm. The suspension-winding flux linkages ψ_fd and ψ_fq experience the cross-saturation from the main-winding q-axis current component i_tq. This phenomenon is demonstrated for ψ_fq in Fig. 2.5(c).

Since the radial forces are obtained from each FEM simulation, the radial-force constants M_d, M_q can also be analyzed as a function of currents at each operating point, by calculating them from (2.9). Both M_d and M_q show

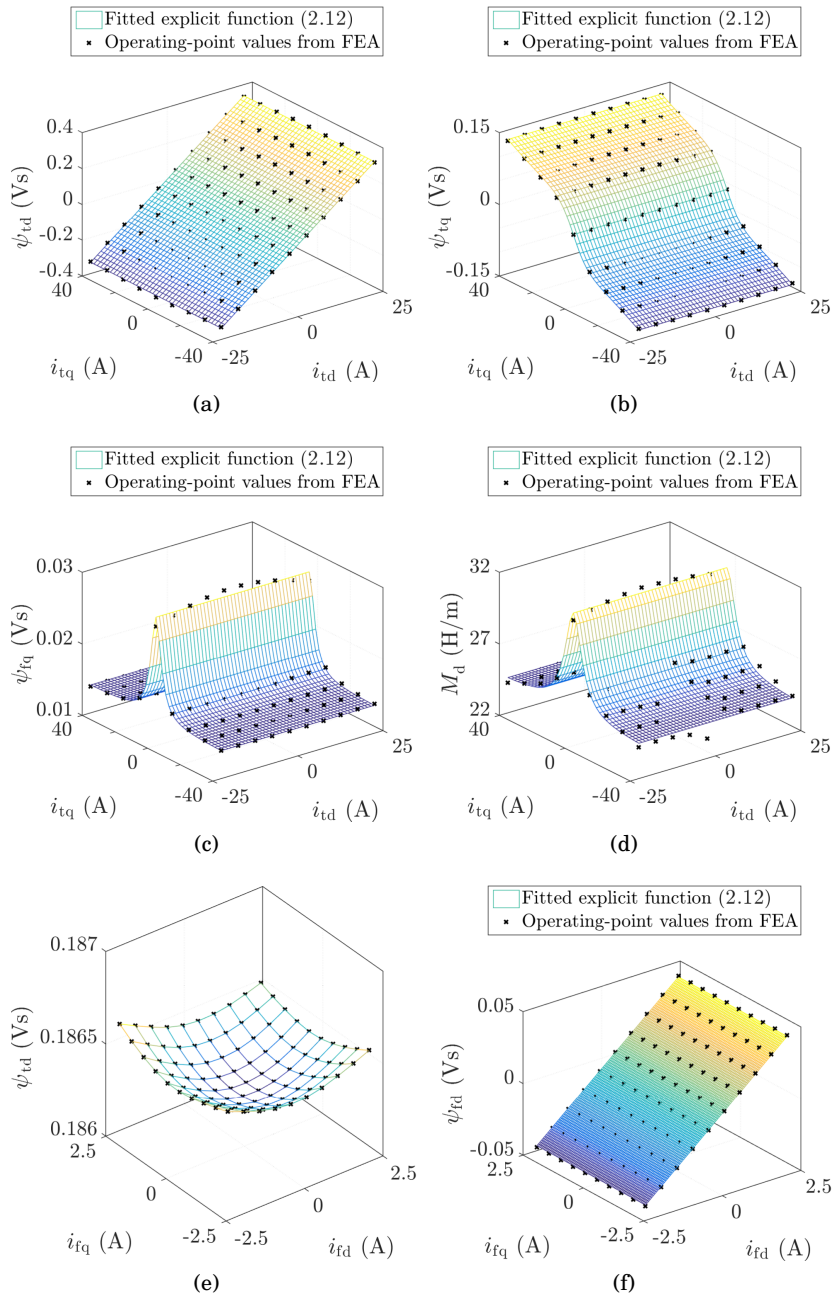

Figure 2.5. Flux linkages and radial force constants as functions of the current components: (a) $\psi_{td}(i_{td}, i_{tq})$; (b) $\psi_{tq}(i_{td}, i_{tq})$; (c) $\psi_{fq}(i_{td}, i_{tq})$; (d) $M_d(i_{td}, i_{tq})$; (e) $\psi_{td}(i_{fd}, i_{fq})$; and (f) $\psi_{fd}(i_{fd}, i_{fq})$. (a), (b), (c), and (d) are plotted at $i_{fd} = i_{fq} = 0.75$ A, while (e) and (f) are plotted at $i_{td} = 12.5$ A and $i_{tq} = 40$ A. FEM-based results are shown with black crosses, while the surfaces show the results calculated from the magnetic model (2.12). In (e), only FEM results are displayed to show that ψ_{td} remains nearly constant irrespective of i_{fd} and i_{fq}.

Table 2.1. Magnetic model parameters of an example machine.

Parameter	$L_{q,0}$ [mH]	a [mH]	b [1/A^2]	$L_{s,0}$ [mH]	c [mH/A^2]	d [1/A^2]
Value	2.7	6	0.006	37.3	1.3	0.07
Parameter	$M_{d,0}$ [H/m]	e [H/(m·A^2)]	f [1/A^2]	L_d [mH]	M_q [H/m]	
Value	31.28	0.18	0.026	15	0.66	

strong dependency on the main winding currents. Fig. 2.5(d) shows M_d as a function of i_{td} and i_{tq}. Because M_d dominates the overall radial force production, the variation in M_q has a minor effect and can be omitted.

Influence of the Suspension-Winding Current
Based on the FEM results, the cross-saturation between the suspension-winding currents and the main-winding flux linkages is minimal, as demonstrated in Fig. 2.5(e). Hence, the suspension-winding currents are assumed to have no influence on the main-winding inductances L_d and L_q. Fig. 2.5(f) shows that the suspension winding exhibits no self-saturation and no cross-saturation behavior between its current and flux-linkage components. Thus, the suspension winding inductance L_s depends only on the main winding currents.

Explicit-Function-Based Magnetic Model
Based on the findings from the FEM analysis, an explicit-function-based magnetic model is proposed. The form of the explicit functions applied here for the saturation modeling was initially proposed in [53]

$$\psi_{td}(i_{td}) = L_d i_{td} \qquad \psi_{tq}(i_{tq}) = L_q(i_{tq}) i_{tq} \tag{2.12a}$$

$$\psi_{fd}(i_{tq}, i_{fd}) = L_s(i_{tq}) i_{fd} \qquad \psi_{fq}(i_{tq}, i_{fq}) = L_s(i_{tq}) i_{fq} \tag{2.12b}$$

$$L_q(i_{tq}) = L_{q,0} + \frac{a}{1 + b i_{tq}^2} \qquad L_s(i_{tq}) = L_{s,0} - \frac{c i_{tq}^2}{1 + d i_{tq}^2} \tag{2.12c}$$

$$M_d(i_{tq}) = M_{d,0} - \frac{e i_{tq}^2}{1 + f i_{tq}^2} \qquad L_d = \text{const} \quad M_q = \text{const} \tag{2.12d}$$

where $L_{q,0}$, $L_{s,0}$, $M_{d,0}$, a, b, c, d, e, and f are the coefficients of the inductance and force-constant functions. Flux linkages as functions of current components are expressed with (2.12a) and (2.12b). The saturating inductances are given as (2.12c). Finally, the radial force constant M_d as a function of i_{tq} is modeled with (2.12d) using the same function form as the inductances. The force constant M_q and the inductance L_d are assumed to be constant.

The coefficients of the explicit functions can be obtained by fitting the model to the FEM-based or measured data. Here, the model is fitted to the FEM-based results of the example bearingless SyRM, and the resulting coefficients are given in Table 2.1. The resulting explicit functions (2.12) are

plotted against the corresponding FEM results in Fig. 2.5 for comparison. Based on these plots, it can be concluded that the form and the fitting of the proposed explicit functions result in a suitable magnetic model for the example bearingless SyRM.

2.3.3 Eccentricity Modeling

The effects of the magnetic saturation are ignored in the following. When a cylindrical rotor surface is assumed and the rotor is displaced from its centric point to a certain x and y position, the air gap length at the angle θ can be given as a cosine function within a complete revolution ($\theta = 0 \dots 2\pi$)

$$g(\theta, x, y) = g_0 - x\cos(\theta) - y\sin(\theta) \tag{2.13}$$

where g_0 is the nominal air gap of the motor. Then, the permeance function is given as

$$P(\theta, x, y) = \mu_0 r l g^{-1}(\theta, x, y) \tag{2.14}$$

where r is the rotor radius; l is the axial length; and μ_0 is the permeability of air. The permeance function can then be used to define the air-gap flux distribution and finally to obtain the inductances by integrating the product of MMF and corresponding flux linkage over the circumference of the air gap [5]. However, the inverse air-gap function is required in order to be able to use the permeance function for calculation of the inductance matrices elements. The exact analytical inverse air-gap function would result in a complicated integration. Instead, the inverse air-gap function can be approximated using series expansion

$$\begin{aligned} g^{-1}(\theta, x, y) &= \frac{K(\theta)}{g(\theta, x, y)} \\ &\approx \frac{K(\theta)}{g_0}\left(1 + \underbrace{\left[\frac{x}{g_0}\cos(\theta) + \frac{y}{g_0}\sin(\theta)\right]}_{\text{first term}} + \underbrace{\left[\frac{x}{g_0}\cos(\theta) + \frac{y}{g_0}\sin(\theta)\right]^2}_{\text{second term}} + \cdots\right) \end{aligned} \tag{2.15}$$

where the coefficient $K(\theta)$ is used for modeling the rotor saliency. The more terms are considered in the expansion, the more accurately it models the actual inverse air-gap length. The textbook model is obtained if only the first term of the series expansion is considered, which becomes a limiting factor when predicting the radial forces, as is shown below. Moreover, in the textbook model, $K(\theta) = 1$, since the rotor saliency is neglected.

Proposed Model

Publication IV proposes an improved model which includes the effects of eccentricity, rotor saliency, and UMP. The proposed model is briefly reviewed below. Since assuming a cylindrical rotor for a SyRM is not

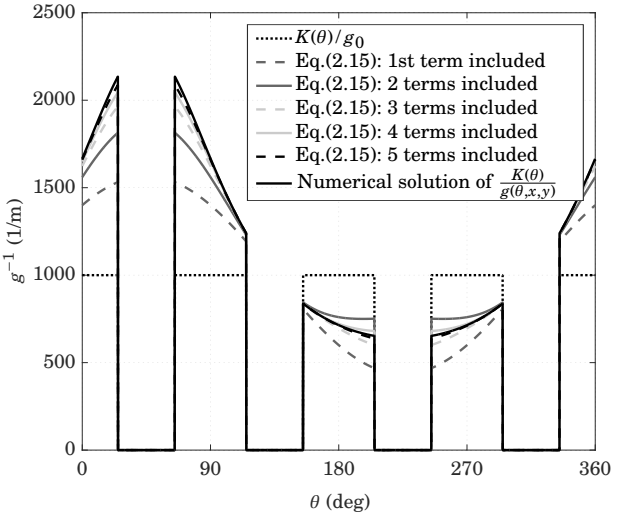

Figure 2.6. Inverse air-gap length calculated numerically compared to the different levels of approximation with (2.15). The nominal air gap of the motor is $g_0 = 1$ mm.

realistic, the coefficient $K(\theta)$ is used to take the rotor saliency into account. Similarly to [49], the coefficient $K(\theta)$ is piecewise defined as

$$K(\theta) = \begin{cases} 0, & \gamma < \theta < \frac{\pi}{2} - \gamma \\ 0, & \frac{\pi}{2} + \gamma < \theta < \pi - \gamma \\ 0, & \pi + \gamma < \theta < \frac{3\pi}{2} - \gamma \\ 0, & \frac{3\pi}{2} + \gamma < \theta < 2\pi - \gamma \\ 1, & \text{otherwise} \end{cases} \tag{2.16}$$

where the constant $0 < \gamma < \pi/4$ defines the saliency of the rotor.

As an example, Fig. 2.6 shows the inverse air-gap length as a function of θ, when $x = y = 0.4$ mm and $\gamma = 25°$. The inverse air-gap length is numerically calculated as an inverse of (2.13) and compared with approximations from (2.15). From this, it can be seen that the accuracy of the series expansion substantially increases when more terms are included. Naturally, better accuracy comes at the price of increased complexity when calculating the elements of the inductance matrices.

In order to model the rotor displacement, the inductance matrices in (2.7) are presented as

$$\begin{aligned} \boldsymbol{L}_{\mathrm{m}}(x,y) &= \boldsymbol{L}_{\mathrm{m0}}\boldsymbol{D}_{\mathrm{m}}(x,y) & \boldsymbol{L}_{\mathrm{s}}(x,y) &= L_{\mathrm{s0}}\boldsymbol{D}_{\mathrm{s}}(x,y) \\ \boldsymbol{M}(x,y) &= c_0\boldsymbol{L}_{\mathrm{m0}}\boldsymbol{D}_{\mathrm{M}}(x,y) & \boldsymbol{L}_{\mathrm{m0}} &= \begin{bmatrix} L_{\mathrm{d0}} & 0 \\ 0 & L_{\mathrm{q0}} \end{bmatrix} \end{aligned} \tag{2.17}$$

where $\boldsymbol{D}_{\mathrm{m}}(x,y)$, $\boldsymbol{D}_{\mathrm{s}}(x,y)$, and $\boldsymbol{D}_{\mathrm{M}}(x,y)$ are the displacement dependency matrices; L_{d0}, L_{q0} are the self-inductances of the main winding; and L_{s0}

is the self-inductance of the suspension winding (which should not be confused with the coefficients $L_{q,0}$ and $L_{s,0}$ used in the saturation model). The scalar-valued coefficient $c_0 = \sqrt{2L_{s0}/(L_{d0}+L_{q0})}/2$ links the inductances to the force constants. Furthermore, the saliency ratio can be defined as

$$\frac{L_{d0}}{L_{q0}} = \frac{4\gamma + \sin(4\gamma)}{4\gamma - \sin(4\gamma)} \approx \frac{3}{4\gamma^2} - \frac{2}{5} \tag{2.18}$$

The exact form of the displacement matrices depends on the number of terms considered in the inverse air-gap approximation. Including only the first term results in

$$\boldsymbol{D}_m = \begin{bmatrix} 1 & 0 \\ 0 & 1 \end{bmatrix} \qquad \boldsymbol{D}_s = \begin{bmatrix} \frac{2\gamma(2g_0^2 - x^2)}{\pi g_0^2} & -\frac{2\gamma xy}{\pi g_0^2} \\ -\frac{2\gamma xy}{\pi g_0^2} & \frac{2\gamma(2g_0^2 - y^2)}{\pi g_0^2} \end{bmatrix} \qquad \boldsymbol{D}_M = \frac{1}{g_0}\begin{bmatrix} x & -y \\ y & x \end{bmatrix} \tag{2.19}$$

Considering a special case with a centric rotor when $x = y = 0$ results in

$$\boldsymbol{D}_m = \begin{bmatrix} 1 & 0 \\ 0 & 1 \end{bmatrix} \quad \boldsymbol{D}_s = \begin{bmatrix} 1 & 0 \\ 0 & 1 \end{bmatrix} \quad \boldsymbol{D}_M = \begin{bmatrix} 0 & 0 \\ 0 & 0 \end{bmatrix} \tag{2.20}$$

It is worth noting that the textbook model (2.8) is actually a combination of (2.19) and (2.20), where $\boldsymbol{D}_s$ is selected from (2.20) and $\boldsymbol{D}_M$ from (2.19), with an additional assumption that $L_d/L_q = M_d/M_q$.

Further, including the second term in the approximation (2.15) gives

$$\boldsymbol{D}_m = d_m = \left(1 + \frac{x^2 + y^2}{2g_0^2}\right) \quad \boldsymbol{D}_s = \begin{bmatrix} d_x & d_{xy} \\ d_{xy} & d_y \end{bmatrix} \tag{2.21}$$

$$\boldsymbol{D}_M = \frac{1}{g_0}\begin{bmatrix} \frac{2x(g_0^2+y^2)}{2g_0^2+x^2+y^2} & \frac{-2y(g_0^2+x^2)}{2g_0^2+x^2+y^2} \\ \frac{y(2g_0^2-x^2+y^2)}{2g_0^2+x^2+y^2} & \frac{x(2g_0^2+x^2-y^2)}{2g_0^2+x^2+y^2} \end{bmatrix}$$

where the full expressions for d_x, d_y, and d_{xy} are given in Publication IV. From (2.17) and (2.21), it is evident that the elements of inductance matrix $\boldsymbol{L}_m$ also depend on x and y when the second term is included.

The stored magnetic co-energy of the system is

$$W'_m = \frac{1}{2}\begin{bmatrix} \boldsymbol{i}_t^T & \boldsymbol{i}_f^T \end{bmatrix}\begin{bmatrix} \boldsymbol{L}_{m0}\boldsymbol{D}_m & c_0\boldsymbol{L}_{m0}\boldsymbol{D}_M \\ c_0\boldsymbol{L}_{m0}\boldsymbol{D}_M^T & L_{s0}\boldsymbol{D}_s \end{bmatrix}\begin{bmatrix} \boldsymbol{i}_t \\ \boldsymbol{i}_f \end{bmatrix} \tag{2.22}$$

The radial forces can be calculated as follows

$$\begin{aligned} F_x = \frac{\partial W'_m}{\partial x} &= \frac{1}{2}\left(\boldsymbol{i}_t^T\boldsymbol{L}_{m0}\frac{\partial \boldsymbol{D}_m}{\partial x}\boldsymbol{i}_t + \boldsymbol{i}_f^T L_{s0}\frac{\partial \boldsymbol{D}_s}{\partial x}\boldsymbol{i}_f\right) \\ &+ \frac{c_0}{2}\left(\boldsymbol{i}_t^T\boldsymbol{L}_{m0}\frac{\partial \boldsymbol{D}_M}{\partial x}\boldsymbol{i}_f + \boldsymbol{i}_f^T\boldsymbol{L}_{m0}\frac{\partial \boldsymbol{D}_M^T}{\partial x}\boldsymbol{i}_t\right) \\ F_y = \frac{\partial W'_m}{\partial y} &= \frac{1}{2}\left(\boldsymbol{i}_t^T\boldsymbol{L}_{m0}\frac{\partial \boldsymbol{D}_m}{\partial y}\boldsymbol{i}_t + \boldsymbol{i}_f^T L_{s0}\frac{\partial \boldsymbol{D}_s}{\partial y}\boldsymbol{i}_f\right) \\ &+ \frac{c_0}{2}\left(\boldsymbol{i}_t^T\boldsymbol{L}_{m0}\frac{\partial \boldsymbol{D}_M}{\partial y}\boldsymbol{i}_f + \boldsymbol{i}_f^T\boldsymbol{L}_{m0}\frac{\partial \boldsymbol{D}_M^T}{\partial y}\boldsymbol{i}_t\right) \end{aligned} \tag{2.23}$$

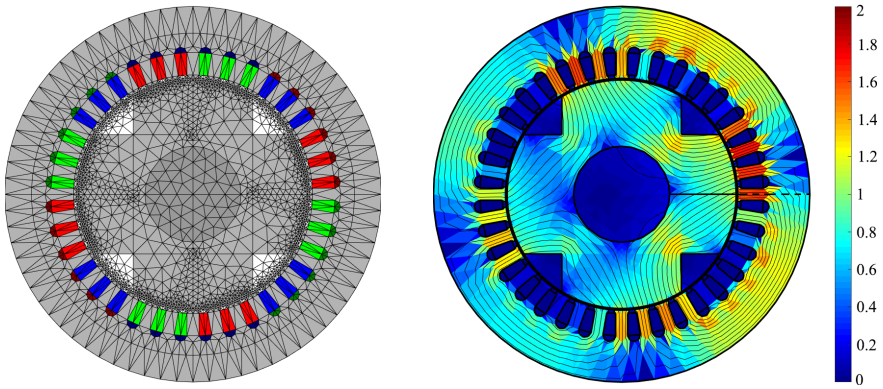

(a) (b) Flux density distribution (T)

Figure 2.7. Salient pole rotor SyRM used in 2D FEM simulations. (a) Motor geometry and mesh. (b) Example magnetic field solution at the rated operating point. The motor nominal air gap is 1 mm. FEM simulations are performed assuming linear magnetics.

It is worth noting that the partial derivatives of the displacement matrices in (2.23) define the x and y dependencies of the radial forces. Hence, including the second term in the inverse air-gap approximation is required in order to include the effect of the UMP in the model.

Parameter Estimation

The model parameters can be estimated based on FEM or measured data. Here, FEM-based data sets are used, which are generated using the same approach as in Section 2.3.2. Additionally, these simulation sets were carried out at different rotor radial positions. The motor geometry used for FEM analysis is shown in Fig. 2.7(a). An example magnetic field solution at the rated radial force and torque is shown in Fig. 2.7(b).

When the flux linkages, currents, and radial forces are obtained from the FEM at different operating points, the model parameter values can be calculated by applying the LLS fitting method. LLS can be used for identifying the parameters of both the textbook model and the proposed model.

The textbook model (2.8) contains five parameters to be decided: L_d, L_q, L_s, M_d, and M_q. In the textbook model, the force constants are treated as being independent from the inductances. Thus, parameter estimation requires two steps. Firstly, one LLS fit is required to obtain the force constants M_d and M_q from the FEM-based force data and (2.9). Secondly, with M_d and M_q fixed, another LLS fit can be used to solve the main- and suspension-winding inductances from (2.7) and (2.8).

As an example, the textbook model parameters are obtained from two FEM simulation sets: one with the rotor at $x = 0$ and $y = -0.6$ mm, imitating the rotor resting on the safety bearings, and one with the centric rotor at

Table 2.2. Parameter estimates of the textbook model (2.8).

Parameter	($x = 0$, $y = -0.6$ mm)	($x = y = 0$)
L_d (mH)	17	14.5
L_q (mH)	10.4	8.9
L_s (mH)	239	220
M_d (H/m)	57	40
M_q (H/m)	34	22

Table 2.3. Parameter estimates of the proposed model (2.17).

Parameter	($x = 0$, $y = -0.6$ mm)	($x = y = 0$)
$L_{\mathrm{d}0}$ (mH)	14.4	14.5
$L_{\mathrm{q}0}$ (mH)	8.8	8.9
$L_{\mathrm{s}0}$ (mH)	281	284
γ (deg)	34.7	34.9
c_0	2.46	2.47

$x = 0$, $y = 0$. The parameter values identified for both of these cases are compared in Table 2.2. Here, it can be seen that the identified textbook model parameters vary depending on the rotor radial position that was used when fitting the data.

In contrast to the textbook model, the proposed model (2.17) does not require the radial force data to solve all the necessary parameters. Fitting of the proposed model is performed solely based on (2.7) with inductance matrices (2.17) and displacement matrices (2.21). The data from the FEM is now used in two consecutive LLS fits. Firstly, the main-winding inductance matrix is solved from the operating points in which the suspension-winding current is set to zero. The main-winding inductances are then used to calculate γ from (2.18). Secondly, the suspension-winding inductance matrix can be solved from the operating points in which the main-winding current is set to zero. Finally, the scalar-valued coefficient c_0 can be solved as $c_0 = \sqrt{2L_{\mathrm{s}0}/(L_{\mathrm{d}0} + L_{\mathrm{q}0})}/2$. The detailed fitting procedures for both the textbook model and the proposed model are described in Publication IV.

The parameters of the proposed model are estimated in the same radial-position operating points as with the textbook model and using the same FEM data sets. The results are given in Table 2.3. It can be seen from the table that when the proposed model is used, the fitted parameter values are almost independent from the rotor radial position.

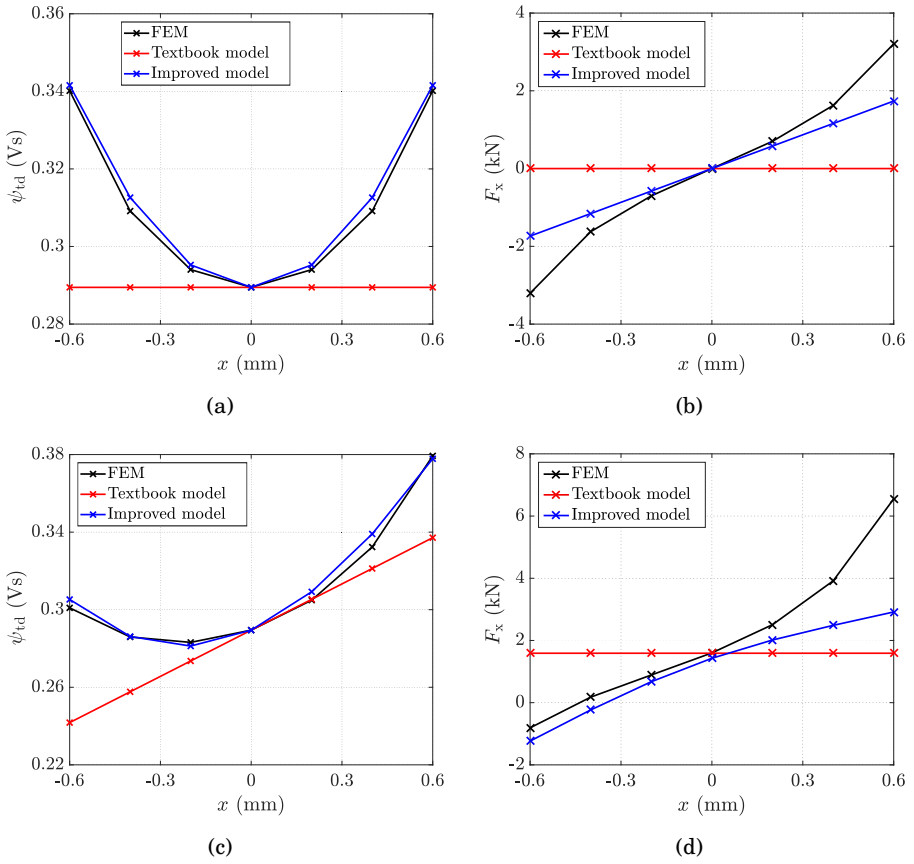

Figure 2.8. Flux linkage ψ_{td} and radial force F_x as functions of radial position x at $y = 0$: (a), (b) $i_{td} = 20$ A and $i_{tq} = i_{fd} = i_{fq} = 0$; (c), (d) $i_{td} = 20$ A, $i_{tq} = 0$ and $i_{fd} = i_{fq} = 2$ A.

Comparison of Models against FEM Results

The proposed model is compared against the textbook model and against the FEM results in Fig. 2.8. The models are parameterized from Table 2.2 and Table 2.3 with values corresponding to the centric rotor case. Using the parameterized models, the flux linkages and the radial forces are calculated using (2.8), (2.9), (2.17), and (2.23) at the same current and radial position operating points as the ones simulated in FEM.

Fig. 2.8(a) shows the flux-linkage component ψ_{td} as a function of radial position x at $y = 0$. Fig. 2.8(b) shows the corresponding radial force F_x. It can be seen that in the textbook model the main-winding flux-linkage variation due to the radial displacements is not modeled. This results in an inability to predict the radial forces due to the UMP. The proposed model inherently includes these effects and improves the accuracy of the predicted radial forces without the use of additional functions. Similar behavior can be seen in Fig. 2.8(c) and Fig. 2.8(d) when the suspension-winding current $i_{fd} = i_{fq} = 2$ A is also supplied. The accuracy of the proposed

model can be further increased by including three or more terms in the series expansion (2.15). However, this would result in a significant increase in the complexity of the model; hence, the selected model is a compromise between complexity and accuracy.

2.3.4 Combined Multiphase Winding

The textbook model of bearingless SyRMs as well as the saturation and eccentricity modeling presented in the previous sections are directly applicable only to machines with separated windings.

In machines with combined multiphase windings, the torque-producing and force-producing currents are superimposed into the same coils. Approaches to superimpose the torque-producing and force-producing currents are available in the literature. Selection of current references for decoupled torque and force generation is presented for a toroidal PM machine in [54]. In [27] and [24], the current reference selection and modeling of a bearingless induction machine with combined multiphase winding is discussed. In [55], similar current selection methods are presented for a parallel combined winding. A current reference selection method is presented for a bearingless slice SyRM in [47], and the torque and force equations are derived. However, to the best of the author's knowledge, dynamic models that are directly applicable for bearingless SyRMs with combined windings have not been presented in the literature before.

Publication V proposes a method to link the textbook model of the bearingless SyRM with separated windings to the machines with a combined multiphase winding. The method allows for the extension of the modeling concepts from Sections 2.3.2 and 2.3.3 to bearingless SyRMs with combined windings. The proposed theory is validated by means of FEM simulations and experimental results. The proposed linking method and FEM-based validation from Publication V are briefly presented below.

Linking Method

To describe the method, an example six-phase bearingless SyRM is considered with the winding diagram shown in Fig. 2.9(a). The phases are marked as A_1, B_1, C_1, A_2, B_2, C_2 and represent either a center coil of a distributed winding or a single coil of a concentrated winding. Six phases can be connected into two independent star connections [A_1, B_1, C_1] and [A_2, B_2, C_2], which allows the motor to be supplied with two general-purpose three-phase inverters.

For a SyRM with a four-pole rotor, the described winding system has to produce a four-pole field to generate the torque and a two-pole field to generate the radial force. The four-pole MMF is generated when both three-phase windings are supplied with the same current, i.e., $[i_{A1}, i_{B1}, i_{C1}] = [i_{A2}, i_{B2}, i_{C2}]$. The two-pole MMF is generated in the case when the three-

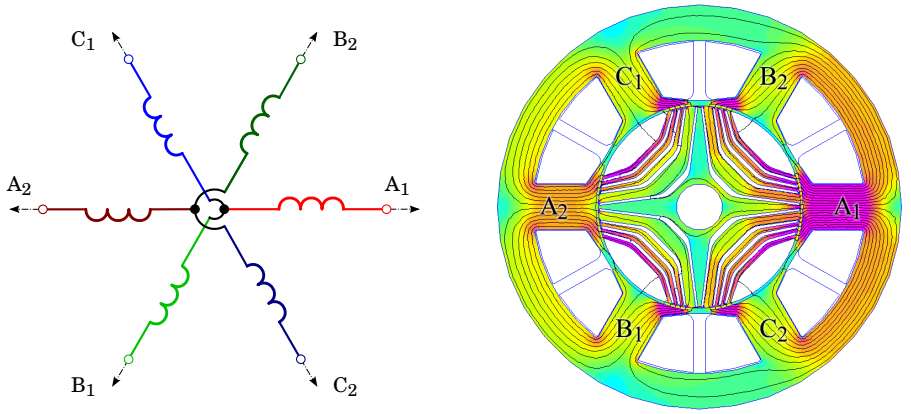

Figure 2.9. (a) Six-phase combined winding arranged into two three-phase star connections; (b) 2D FEM geometry and magnetic field solution of an example combined winding bearingless SyRM. Four-pole and two-pole fields are produced simultaneously by supplying the currents $[i_{A1}, i_{B1}, i_{C1}, i_{A2}, i_{B2}, i_{C2}] = [5, -2.5, -2.5, 3, -1.5, -1.5]$ A or $i_{td} = 4$ A, $i_{fd} = 1$ A, and $i_{tq} = i_{fq} = 0$ at $\vartheta_M = 0$.

phase windings are supplied with the same value but opposite sign currents $[i_{A1}, i_{B1}, i_{C1}] = [-i_{A2}, -i_{B2}, -i_{C2}]$. Thus, for a given current in each phase pair, e.g., i_{A1} and i_{A2}, the torque-producing component can be defined as $i_{tA} = (i_{A1} + i_{A2})/2$, and the force-producing component can be defined as $i_{fA} = (i_{A1} - i_{A2})/2$. The same definitions are applied to other phases resulting in

$$\begin{aligned} i_{tA} &= \frac{i_{A1} + i_{A2}}{2} \qquad i_{tB} = \frac{i_{B1} + i_{B2}}{2} \qquad i_{tC} = \frac{i_{C1} + i_{C2}}{2} \\ i_{fA} &= \frac{i_{A1} - i_{A2}}{2} \qquad i_{fB} = \frac{i_{B1} - i_{B2}}{2} \qquad i_{fC} = \frac{i_{C1} - i_{C2}}{2} \end{aligned} \tag{2.24}$$

The torque and force current components can be selected independently of each other to produce the four- and two-pole-pair fields, respectively. Hence, for modeling purposes, the torque and force current components in the combined winding are the same as the currents flowing in the main and in the suspension windings of a separated winding machine.

Due to the absence of the zero-sequence current, an equivalent two-phase $\alpha\beta$ model can be utilized. The torque current component vector $\boldsymbol{i}_t^s$ can be obtained from i_{tA}, i_{tB}, and i_{tC} directly by applying (2.4). However, the force current component vector $\boldsymbol{i}_f^s$ is obtained using a reversed phase sequence

$$\boldsymbol{i}_f^s = \begin{bmatrix} i_{f\alpha} \\ i_{f\beta} \end{bmatrix} = \begin{bmatrix} \frac{2}{3} & -\frac{1}{3} & -\frac{1}{3} \\ 0 & -\frac{1}{\sqrt{3}} & \frac{1}{\sqrt{3}} \end{bmatrix} \begin{bmatrix} i_{fA} \\ i_{fB} \\ i_{fC} \end{bmatrix} \tag{2.25}$$

since, for the force component, the counterclockwise phase sequence is seen as ACB, while for the torque component, it is ABC.

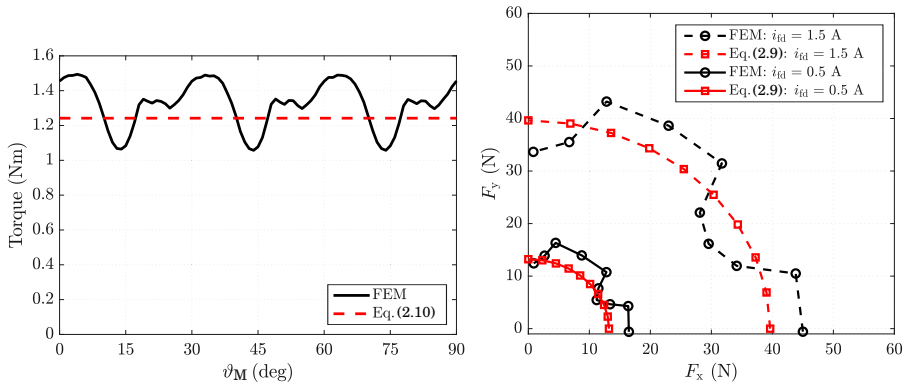

Figure 2.10. Comparison between the model and the FEM-based results: (a) torque as a function of ϑ_M at $i_{td} = i_{tq} = 6$ A and (b) radial forces at $i_{td} = 2$ A and ϑ_M, varying from 0 to $\pi/2$.

Finally, the resulting space vectors can be transformed into synchronous coordinates using (2.5), where $\vartheta_m = 2\vartheta_M$ for the torque component and $\vartheta_m = \vartheta_M$ for the force component. This gives current vectors $\boldsymbol{i}_t = \begin{bmatrix} i_{td} & i_{tq} \end{bmatrix}^T$ and $\boldsymbol{i}_f = \begin{bmatrix} i_{fd} & i_{fq} \end{bmatrix}^T$, which can be used to model the machine in rotor coordinates. Similar transformations, as the ones presented for the currents, can be used for voltages and flux linkages. As a result, the textbook model (2.6), (2.7), (2.8), (2.9), and (2.10) can be applied for modeling the combined winding bearingless SyRMs. The resulting dynamic model is applicable in time-domain simulations, model-based control design, stability analysis, and in real-time control algorithms.

FEM-based Validation of the Method

The applicability of the textbook model to bearingless SyRMs with combined multiphase windings is verified using the FEM. 2D magnetostatic FEM simulations were carried out using FEMM 4.2 software. FEM simulations are carried out for an example bearingless slice motor shown in Fig. 2.9(b). The details of the motor design are presented in Section 4.2. Fig. 2.10 shows the comparison between the torque and radial forces predicted by the textbook model and FEM-based results. The model is able to predict the average torque and radial force throughout the varying rotor angle, which confirms the proposed transformations.

2.4 Linear FSPM Machines

A linear FSPM bearingless machine is a complicated system to model due to multiple reasons: flux paths that change as the machine travels in the x-direction; PM leakage fluxes that cross the air gap and contribute

to the force production; typically substantial saturation effects, which result in nonlinear behavior; and changing air gap during operation, which influences the magnetics and the force production of the machine.

Various analytical and semi-analytical models have been presented for machine design and analysis purposes. Rotating bearingless FSPM machines have been developed in [56]. Nonlinear current to force and torque relationships have been modeled and taken into account in the control system presented in [57]. However, few concepts can be carried over from rotating to linear bearingless FSPM machines. Analytical models for conventional linear FSPM machines have been developed in [58], [59], and [60]. These models, however, are insufficient for bearingless applications, since the air gap variation and the normal force production are essential phenomena to be included in the modeling of a bearingless linear machine. In [61], a linear bearingless FSPM machine is studied using the FEM, including the force production characteristics, air-gap variation, and magnetic saturation. However, the proposed modeling approach relies on FEM-based data implemented in the form of lookup tables, which makes it difficult to generalize the model for other machine designs. Furthermore, the model of the machine is not presented independently from the control method.

Publication VII proposes a dynamic model for bearingless FSPM linear machines based on a physically feasible equivalent circuit. A magnetic equivalent circuit is used to derive the structure of the analytical equations describing the magnetic model and the force production. Using the FEM, the magnetic characteristics of an example three-phase machine are studied in detail, including the influence of the air gap variation, magnetic saturation, and linear movement position along the rail. A simple method for parameterizing the model from the FEM or measured data is presented. The model is also validated by means of experiments.

The proposed model from Publication VII and its validation using FEM simulations and experiments are reviewed below.

2.4.1 Generic Dynamic Model

Similar to the rotating variants, linear FSPM machines can be modeled and controlled using two-axis models [59]. The three-phase currents can be transformed into $\alpha\beta$ coordinates using (2.4), with similar transformations applicable to the voltages and flux linkages.

The key phenomena of three-phase FSPM linear machines can be better visualized and explained by using a conceptual two-phase machine. Fig. 2.11 shows a two-phase machine with a simple 4-slot/5-pole structure and visualizes the flux paths of the PMs at two mover positions. At the mover position $x = 0$, the PM flux links predominantly with the coils of the α-phase, while no PM flux links with the coils of the β-phase. The polarity

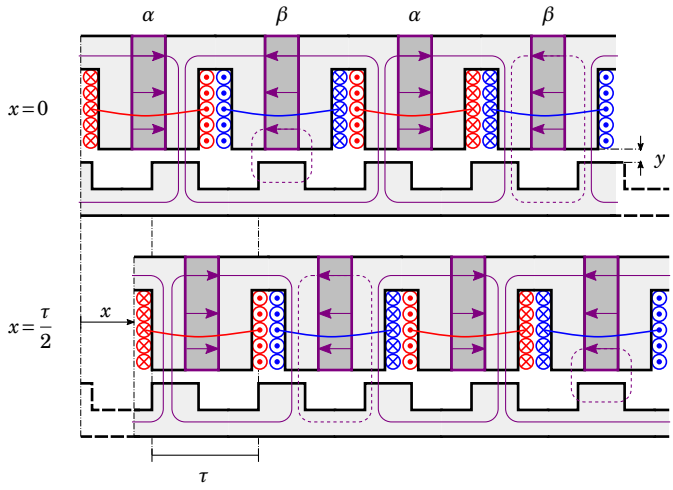

Figure 2.11. Conceptual two-phase FSPM linear machine with the mover at $x = 0$ and at $x = \tau/2$. The arrows show the polarities of the PMs. The crosses and dots define the positive direction of the coil currents. The phases α and β are labeled above the corresponding coils. The dominant flux paths due to the PMs are sketched. The leakage flux paths are shown with the dashed lines.

of the α-phase flux linkage is reversed, as the mover travels to $x = \tau/2$. There are also PM leakage fluxes which do not link with the windings and, thus, cannot be seen at the machine terminals. However, they cross the air gap and contribute to the magnetic field energy and the normal force production.

The FSPM machine is modeled in dq coordinates by transforming the currents with (2.5) and applying the same transformations to the voltages and flux linkages. In well-designed linear machines, the flux linkages vary almost sinusoidally, and the spatial harmonics and the end effects are minor. Therefore, the model in the dq coordinates is assumed independent of x, and the magnetic model is of the form

$$i_\mathrm{d} = i_\mathrm{d}(\psi_\mathrm{d}, \psi_\mathrm{q}, y) \qquad i_\mathrm{q} = i_\mathrm{q}(\psi_\mathrm{d}, \psi_\mathrm{q}, y) \tag{2.26}$$

Flux linkages are chosen as independent state variables, which simplifies the inclusion of the magnetic saturation and results in the most simple voltage equation form

$$\begin{aligned} \frac{\mathrm{d}\psi_\mathrm{d}}{\mathrm{d}t} &= u_\mathrm{d} - R i_\mathrm{d} + \omega_\mathrm{m} \psi_\mathrm{q} \\ \frac{\mathrm{d}\psi_\mathrm{q}}{\mathrm{d}t} &= u_\mathrm{q} - R i_\mathrm{q} - \omega_\mathrm{m} \psi_\mathrm{d} \end{aligned} \tag{2.27}$$

where $\omega_\mathrm{m} = (2\pi/\tau) \cdot (\mathrm{d}x/\mathrm{d}t)$ is the electrical angular speed.

The core losses of the machine are omitted, although if required they could be separately taken into account. Applying the assumption of a

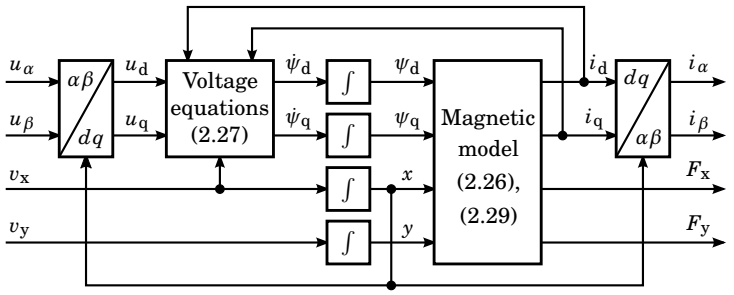

Figure 2.12. Block diagram in the dq coordinates representing a generic dynamic model of a bearingless linear machine.

lossless magnetic field, the rate of change of the magnetic field energy is

$$\frac{\mathrm{d}W}{\mathrm{d}t} = i_\mathrm{d}\left(\frac{\mathrm{d}\psi_\mathrm{d}}{\mathrm{d}t} - \omega_\mathrm{m}\psi_\mathrm{q}\right) + i_\mathrm{q}\left(\frac{\mathrm{d}\psi_\mathrm{q}}{\mathrm{d}t} + \omega_\mathrm{m}\psi_\mathrm{d}\right) - F_\mathrm{x}\frac{\mathrm{d}x}{\mathrm{d}t} - F_\mathrm{y}\frac{\mathrm{d}y}{\mathrm{d}t} \tag{2.28}$$

It is worth noting that the magnetic field energy W is generally nonzero at $\psi_\mathrm{d} = \psi_\mathrm{q} = 0$ because of the PM leakage fluxes. The thrust and normal forces can be derived from the magnetic field energy [39], [62]. Further assuming no x dependency, this results in the following expressions

$$F_\mathrm{x} = \frac{2\pi}{\tau}(\psi_\mathrm{d} i_\mathrm{q} - \psi_\mathrm{q} i_\mathrm{d}) \tag{2.29a}$$

$$F_\mathrm{y} = -\frac{\partial W(\psi_\mathrm{d}, \psi_\mathrm{q}, y)}{\partial y} \tag{2.29b}$$

Although the air gap y is not directly visible in (2.29a), the thrust-force production depends on the air gap value via the current components (2.26).

The presented equations comprise a generic dynamic model for a bearingless linear machine, represented with a block diagram in Fig. 2.12. The model of the electrical subsystem can be easily augmented with a mechanical model with forces F_x, F_y as inputs and the speeds v_x, v_y as outputs.

2.4.2 Magnetic Model and Force Production

The magnetic model in Fig. 2.12 is derived for FSPM linear machines by using equivalent magnetic circuits. Since the PM flux links only with the d-axis winding, the currents (2.26) can be written in a more specific form

$$i_\mathrm{d} = \Gamma_\mathrm{d}(\psi_\mathrm{d}, \psi_\mathrm{q}, y)\psi_\mathrm{d} - i_\mathrm{m}(y) \tag{2.30a}$$

$$i_\mathrm{q} = \Gamma_\mathrm{q}(\psi_\mathrm{d}, \psi_\mathrm{q}, y)\psi_\mathrm{q} \tag{2.30b}$$

where Γ_d and Γ_q are the inverse inductances and i_m is the equivalent MMF of the PMs seen from the terminals. All of these functions depend on the air gap y. The inverse inductances depend on the flux linkages due to the

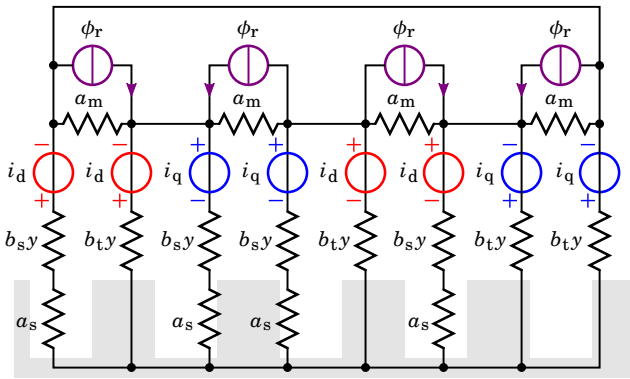

Figure 2.13. Magnetic equivalent circuit of the conceptual machine. The reluctance above the tooth is $b_t y$, and the reluctance of the slot is $a_s + b_s y$, where a_s, b_s, and b_t are assumed to be constants. Unity turns for the coil MMFs are assumed.

magnetic saturation. The magnetic field energy at $\psi_d = \psi_q = 0$ due to the leakage fluxes is denoted with w_0 and also depends on the air gap.

To find suitable and physically feasible expressions for Γ_d, Γ_q, i_m, and w_0, a magnetic equivalent circuit in Fig. 2.13 is considered. The circuit is formed based on the most significant flux paths of the conceptual machine shown in Fig. 2.11. The PMs are modeled using the Norton equivalent circuit [63], consisting of the internal reluctance a_m and the remanent flux ϕ_r of the magnet, which are both constant. The constant reluctance a_s models the reluctance between the rail poles. The reluctances $b_s y$ and $b_t y$ depend on the air gap, b_s and b_t being constants.

In Publication VII, the expressions for Γ_d, Γ_q, i_m, and w_0 are derived using standard circuit theory for the equivalent circuit in Fig. 2.13 while assuming linear magnetics. However, the resulting rational functions produce very long force expressions.

To simplify and generalize the model, the rational functions $\Gamma_d(y)$, $\Gamma_q(y)$, and $i_m(y)$ are approximated with their series expansion at $y = 0$. First-order expansion is used for the inverse inductances, and second-order expansion is applied for the equivalent MMF.

Finally, the expressions for the inverse inductances Γ_d and Γ_q are augmented with a non-linear reluctance term to model the saturation effects. This gives the final expressions for the magnetic model

$$\Gamma_d(\psi_d, \psi_q, y) = a_d + b_d y + c_{dq}(\psi_d^2 + \psi_q^2) \tag{2.31a}$$

$$\Gamma_q(\psi_d, \psi_q, y) = a_q + b_q y + c_{dq}(\psi_d^2 + \psi_q^2) \tag{2.31b}$$

$$i_m(y) = i_{m0} + b_m y + b'_m y^2 \tag{2.31c}$$

where a_d, a_q, b_d, b_q, c_{dq}, i_{m0}, b_m, and b'_m are constants. For the resulting model, the reciprocity condition $\partial i_d/\partial \psi_q = \partial i_q/\partial \psi_d$ holds, i.e., the nonlinear magnetic circuit is lossless [62]. A similar approach to saturation modeling has been used in [64]. A more elaborate saturation model with separate

Table 2.4. Fitted model parameters of an example machine.

Parameter	a_d [1/H]	a_q [1/H]	b_d [1/(H·mm)]	b_q [1/(H·mm)]	c_dq [1/(H·(Vs)^2)]
Value	4.4	4.1	−0.32	−0.21	7.1
Parameter	i_m0 [A]	b_m [A/mm]	b'_m [A/(mm)^2]	f_m [kN]	c_m [1/mm]
Value	3.8	−1.4	0.17	6.0	0.34

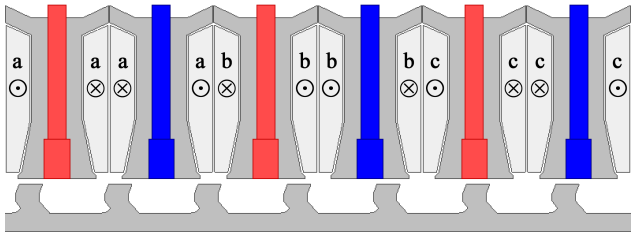

Figure 2.14. Geometry of an example three-phase FSPM linear machine. The crosses and dots define the positive direction of the coil currents.

terms for self-axis and cross-axis saturation can also be employed [65].

The total magnetic field energy corresponding to (2.31) is given as

$$W = \frac{\Gamma_\mathrm{d}(\psi_\mathrm{d},\psi_\mathrm{q},y)\psi_\mathrm{d}^2 + \Gamma_\mathrm{q}(\psi_\mathrm{d},\psi_\mathrm{q},y)\psi_\mathrm{q}^2}{2} - i_\mathrm{m}(y)\psi_\mathrm{d} - \frac{c_\mathrm{dq}(\psi_\mathrm{d}^2+\psi_\mathrm{q}^2)^2}{4} + w_0(y) \quad (2.32)$$

The field energy w_0 is assumed equal to the magnetically linear case. It is worth noting that despite this assumption, the nonlinear magnetic circuit is physically consistent

$$w_0(y) = \frac{\Gamma_\mathrm{d}(y)\psi_\mathrm{d0}(y)^2}{2} + \frac{f_\mathrm{m} y}{1+c_\mathrm{m} y} \quad (2.33)$$

where c_m and f_m are constants and $\psi_\mathrm{d0}(y)$ is the d-axis flux linkage at $i_\mathrm{d} = 0$, i.e., $\psi_\mathrm{d0}(y) = i_\mathrm{m}(y)/\Gamma_\mathrm{d}(y)$. Following (2.29b), the normal force expression is

$$F_\mathrm{y} = -\frac{b_\mathrm{d}\left[\psi_\mathrm{d}^2 - \psi_\mathrm{d0}(y)^2\right] + b_\mathrm{q}\psi_\mathrm{q}^2}{2} + (b_\mathrm{m} + 2b'_\mathrm{m} y)[\psi_\mathrm{d} - \psi_\mathrm{d0}(y)] - \frac{f_\mathrm{m}}{(1+c_\mathrm{m} y)^2} \quad (2.34)$$

The voltage equations (2.27) together with the magnetic model (2.30), (2.31) and the force expressions (2.29a), (2.34) describe the magnetic model of the bearingless FSPM linear machine including the effects of magnetic saturation and air gap variation.

2.4.3 Model Validation

The parameters of the proposed model depend on the geometry of a specific FSPM machine. However, the model is intended to be parameterized by fitting based on either the FEM or measured data. While different fitting methods are applicable for this task, one example fitting procedure based on the LLS method is described in Publication VII. Two consecutive fittings are performed to solve the parameters of the equations (2.31) and (2.34).

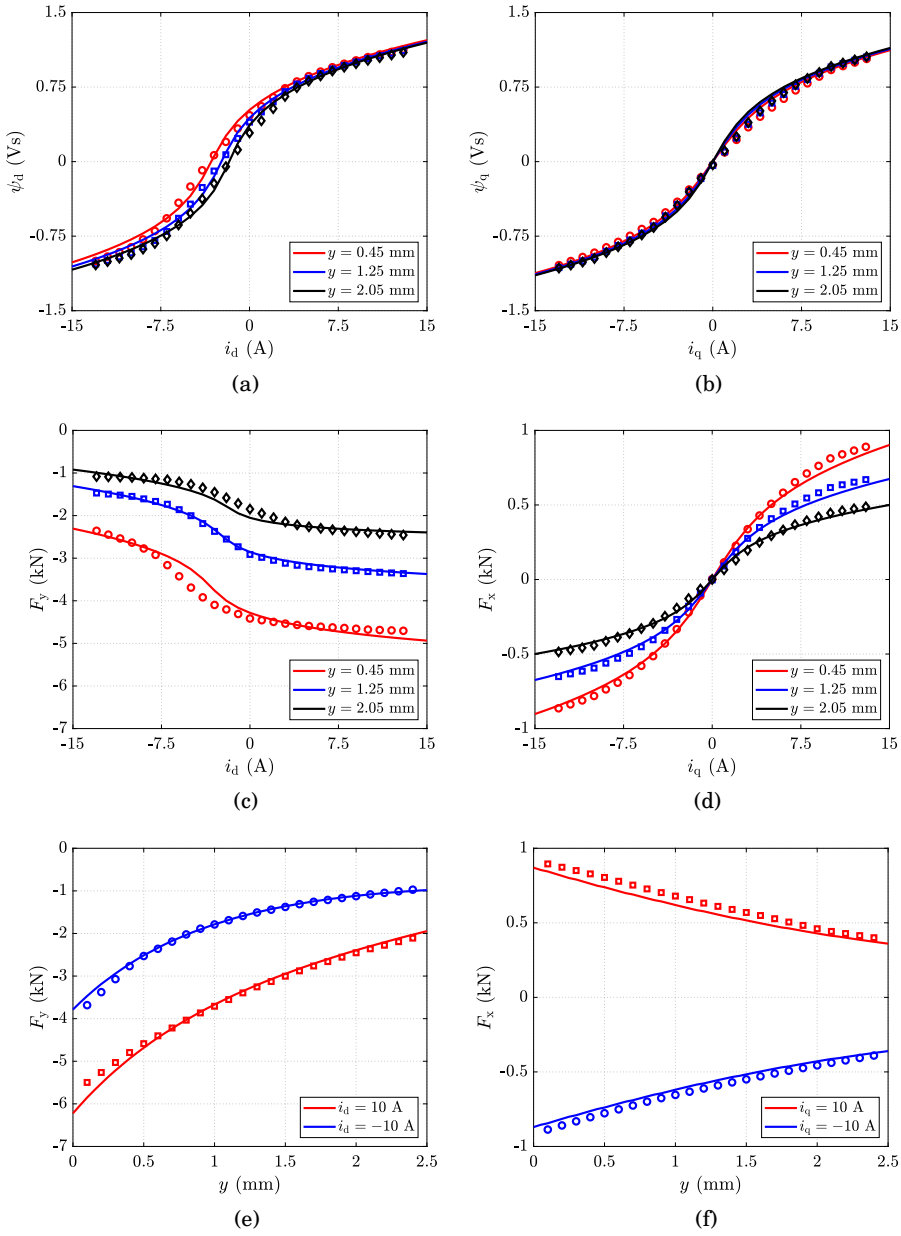

Figure 2.15. Comparison between the FEM results (shown with markers) and the fitted model predictions (shown with lines): (a) $\psi_d(i_d)$ at $i_q = 0$; (b) $\psi_q(i_q)$ at $i_d = 0$; (c) $F_y(i_d)$ at $i_q = 0$; (d) $F_x(i_q)$ at $i_d = 0$; (e) $F_y(y)$ at $i_q = 0$; and (f) $F_x(y)$ at $i_d = 0$.

In order to validate the proposed model the parameters are fitted into FEM data of an example FSPM linear machine shown in Fig. 2.14. The details of the machine construction are presented in Section 4.3. Ansys Maxwell software is used to carry out magnetostatic 2D FEM simulations. The FEM data used for fitting is computed by solving the flux linkages (ψ_d, ψ_q) and forces (F_x, F_y) as a function of currents (i_d, i_q) and the air gap y

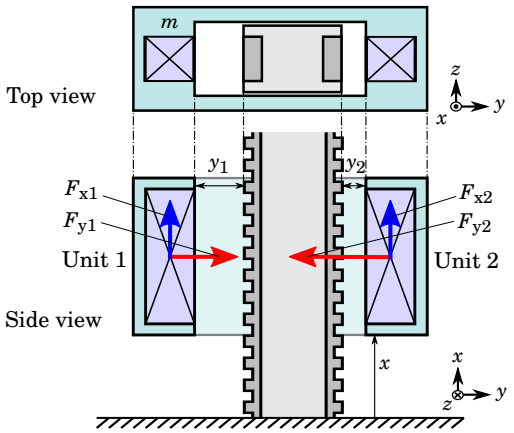

Figure 2.16. Mechanical arrangement of a double-sided linear bearingless system. The traction forces F_{x1}, F_{x2} and the attraction forces F_{y1}, F_{y2} of the two opposing machine units are shown with arrows.

in predefined operating points (similarly as in Section 2.3.2). The resulting fitted model parameters are given in Table 2.4.

The results predicted by the proposed model are compared to the FEM-based results. Figs. 2.15(a) and 2.15(b) show the self-axis saturation characteristics $\psi_d(i_d)$, $\psi_q(i_q)$ at three fixed air gap values y. Figs. 2.15(c) and 2.15(d) show the corresponding normal force F_y and thrust force F_x production as a function of the current components. It is worth noting that the forces are not fitted into the FEM force data, but rather they are calculated with (2.29a) and (2.34) based on the fitted magnetic model parameters shown in Table 2.4. Finally, Figs. 2.15(e) and 2.15(f) show the variation of forces F_y, F_x as a function of air gap y changing from 0 to double the nominal value.

Thus, it can be seen that the proposed model is able to predict the magnetic behavior and the force production of an example FSPM linear machine with reasonable accuracy. Additionally, the FEM results presented in Publication VII show the cross-saturation behavior and also demonstrate that the forces F_x and F_y are practically independent of the mover x-axis position. In Publication VII, the attraction force predicted by the model is compared against the experimentally measured force at different air gaps and currents. The comparison shows that the proposed model is able to predict the attraction force reasonably well. The model was also fitted to the FEM data of another FSPM linear machine design, and the fitting showed equally good results. Overall, the characteristics of the proposed model are smooth, predictable, and physically consistent, which is important when utilizing the model for control purposes.

2.4.4 Mechanical Model of a Double-Sided Linear System

Previous subsections consider the modeling of a single linear FSPM machine. However, when used as part of a linear bearingless system, multiple linear machine units are required to stabilize the necessary degrees of freedom, e.g., as shown in Fig. 1.3. For control design purposes, it is beneficial to define the mechanical model for the whole mover assembly, i.e., multiple motor units attached together.

Fig. 2.16 shows the simplest double-sided configuration with two machine units. Configurations with more machine units are typically used to stabilize additional DOFs, e.g., tilting around the z-axis. However, with a two-machine configuration, it is only possible to actively control two DOFs: levitation along the y-axis by controlling the attraction forces F_{y1}, F_{y2} and propulsion along the x-axis by controlling the thrust forces F_{x1}, F_{x2}.

For control design purposes, the double-sided two-machine unit configuration can be treated as one device by defining the total thrust force, the differential attraction force, and the differential air gap as

$$\Sigma F_{\mathrm{x}} = F_{\mathrm{x1}} + F_{\mathrm{x2}} \qquad \Delta F_{\mathrm{y}} = F_{\mathrm{y2}} - F_{\mathrm{y1}} \qquad \Delta y = \frac{y_1 - y_2}{2} \tag{2.35}$$

where y_1 and y_2 are the air gaps of individual machine units. These definitions are used in the levitation control design, which is discussed in the next chapter.

3. Control

In this chapter, the control system design is discussed. Classical model-based control theory [66] is applied to bearingless machines. The control is described as applied to rotating SyRMs and double-sided linear FSPM machines, but most concepts are also applicable to other machine types.

Control systems are developed in continuous-time domain in Publication III and Publication V, while a direct discrete-time design is applied in Publication VI. For digital implementation, continuous-time designs are discretized with forward Euler approximation. The approximation holds well when the sampling frequency is at least 10~20 times higher than the closed loop bandwidth [67].

The need for active control in magnetically levitated systems arises from Earnshaw's theorem. For magnetic fields, the theorem states that it is not possible to achieve static levitation using any combination of fixed magnets and electric charges (unless using diamagnetic materials, such as superconductors). This inherent unstable nature necessitates reliable active control in order to maintain the levitation of a bearingless system.

In the literature, the aspects of magnetic levitation control are mostly discussed in relation to AMBs. Some aspects can be carried over to the control of bearingless machines. However, there are additional control challenges that are associated with bearingless machines:

- The production of torque and force (or normal force and thrust force in linear systems) is often coupled due to a shared magnetic circuit and requires decoupling through an appropriate selection of currents.
- The magnetic circuit of SyRMs and FSPM machines often saturates during operation, which can make typical linear controllers unable to provide adequate performance throughout the operating range.
- A possible air gap change during operation has an influence on the magnetic circuit parameters and in turn on the force production, requiring additional compensation from the control system.

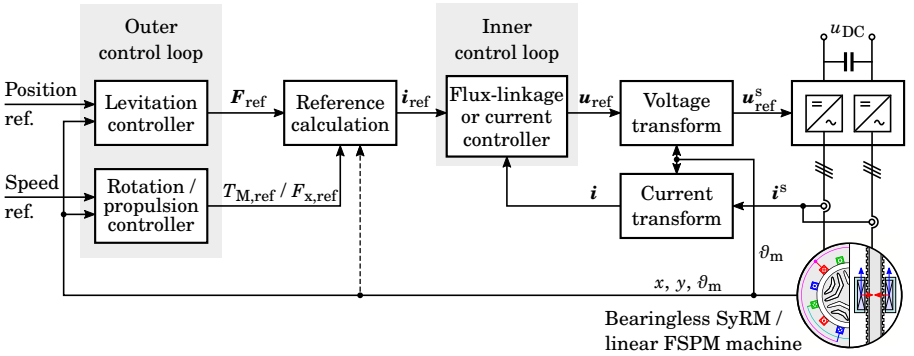

Figure 3.1. Overview of the cascaded control system structure.

3.1 Cascaded Control

In this dissertation, a cascaded control system structure is applied. The overall structure is illustrated with a functional block diagram in Fig. 3.1. The advantage of the cascaded structure is that each control loop can be designed and tuned separately. In addition, the signal flow between the subsystems is clearly visible, which allows the intermediate control signals to be probed for analysis or manipulated to account for additional effects, e.g., disturbances or nonlinearities. However, the designer must ensure sufficient separation between the poles of the inner and outer control loops to make sure that their dynamics are decoupled.

The plant represents either a bearingless SyRM with separated or combined windings or a bearingless double-sided FSPM linear machine arrangement. The plant is supplied with two three-phase inverters which in general can have the same or different DC-link supply. Following the analysis from Chapter 2, the control system is considered in synchronous coordinates. Current transform and voltage transform blocks are used as an interface between the phase quantities on the plant side and the synchronous-coordinate quantities on the control system side. The transformations are based on (2.4) and (2.5), but the exact form depends on the bearingless machine type.

In a control system of a double-sided FSPM linear machine, (2.4) and (2.5) can be applied directly to each machine unit to transform the measured currents, whereas voltage references are transformed back into the stator coordinates using the inverse of these transformations.

For rotating SyRMs, it is important to note that when the machine is rotating and a constant radial force is produced in xy coordinates, the electrical-angular frequencies of both the torque and the force component currents are the same (see Fig. 2.3). Thus, in order to avoid steady-state errors, the inner control loop is designed in a coordinate system rotating at the electrical angular frequency of $2\omega_{\mathrm{M}}$. Both the torque and force current vectors are rotated by the same angle $2\vartheta_{\mathrm{M}}$, resulting in the current vector

to be controlled $\boldsymbol{i} = [i_{\mathrm{td}}, i_{\mathrm{tq}}, i'_{\mathrm{fd}}, i'_{\mathrm{fq}}]^{\mathrm{T}}$. Here, i'_{fd} and i'_{fq} can be expressed as

$$\begin{bmatrix} i'_{\mathrm{fd}} \\ i'_{\mathrm{fq}} \end{bmatrix} = \mathrm{e}^{-\vartheta_{\mathrm{M}}\boldsymbol{J}} \begin{bmatrix} i_{\mathrm{fd}} \\ i_{\mathrm{fq}} \end{bmatrix} \tag{3.1}$$

The same transformation applies both to the measured currents as well as the reference currents. Detailed transformations used for the control of separated winding SyRMs are presented in Section IV of Publication III, and for the control of combined winding SyRMs in Section III of Publication V.

The inner control loop is used to realize the requested current reference $\boldsymbol{i}_{\mathrm{ref}} = [i_{\mathrm{td,ref}}, i_{\mathrm{tq,ref}}, i'_{\mathrm{fd,ref}}, i'_{\mathrm{fq,ref}}]^{\mathrm{T}}$ by receiving the measured current $\boldsymbol{i}$ as feedback and controlling the voltage reference $\boldsymbol{u}_{\mathrm{ref}}$ sent to the inverters. The current or flux linkage can be selected as a state variable when designing the controller. When employing a flux linkage controller, the currents $\boldsymbol{i}$ and $\boldsymbol{i}_{\mathrm{ref}}$ have to be mapped to the corresponding flux linkages using, e.g., lookup tables or explicit functions, as will be discussed further.

The outer control loop consists of a separate levitation controller and a rotation or propulsion controller for a rotating or linear bearingless system, respectively. These controllers can be designed and tuned independently of each other. The levitation controller ensures stable levitation by outputting a force reference $\boldsymbol{F}_{\mathrm{ref}}$ based on the measured rotor/mover position. The rotation/propulsion controller allows the bearingless machine to operate in speed-control mode by taking the speed feedback, e.g., as $\omega_{\mathrm{m}} = \mathrm{d}\vartheta_{\mathrm{m}}/\mathrm{d}t$, and outputting the torque reference $T_{\mathrm{M,ref}}$ for rotating machines and the propulsion force reference $F_{\mathrm{x,ref}}$ for linear machines.

The reference calculation block is used to map the mechanical references from the outer control loop to the current references for the inner control loop. This is an important part of the control system, which ensures that the requested forces/torque are actually realized by selecting appropriate current references. The Reference calculation may also require the rotor/-mover position and electrical angle information to compensate for the UMP and angle-dependent torque/force ripple.

In the following sections, each part of the control system is presented.

3.2 Inner Control Loop: Current or Flux-Linkage Controller

The inner control loop sets the dynamic limitation on the outer control loop. The performance of the inner control loop is especially important for bearingless machines in order to quickly and independently realize the requested torque and radial force for suspension. The inner control loop has to have sufficiently high bandwidth in order to compensate, e.g., unbalanced vibration and bending modes in high-speed applications [68], [69]. In addition, the ability to achieve high bandwidth at low switching frequencies would allow implementation with general purpose inverters.

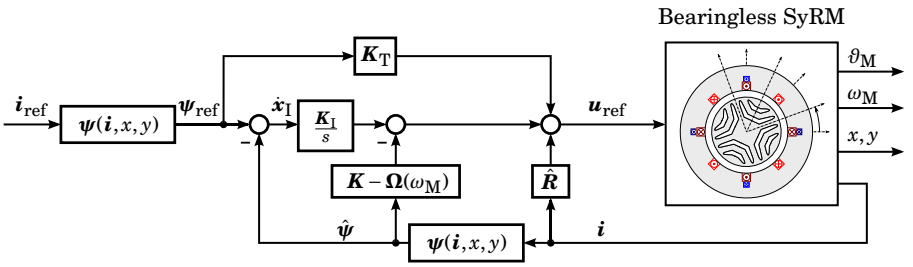

Figure 3.2. Proposed state-space flux-linkage controller structure for bearingless SyRMs. The controller is in synchronous coordinates and the coordinate transformations are not shown in the block diagram.

In the literature, the inner control loop is most commonly represented with a constant parameter current controller. Proportional integral derivative (PID) type current controllers are used for example in [70], [71], [72], and [55]. However, little attention is usually given to analytical controller tuning.

Analytical design rules for a model-based PI-type current controller are presented in [73] for conventional AC machines. The same principle can be applied to bearingless machines. However, if a constant parameter current controller is used for heavily saturating machines, such as SyRMs and FSPM machines, the controller performance will vary depending on the operating point. This can be addressed by using, for example, gain scheduling control or implementing inductance variation in the form of lookup tables or explicit functions [74]. These approaches can manage the problem of varying loop bandwidth due to saturation, but they do not address the cross-coupling between the torque and force components. Decoupling methods are presented in [50] and [75], but no analytical rules for the tuning of the current controller are given.

Publication III proposes a model-based analytical design method for a state-space flux-linkage controller. The method is described as applied to bearingless SyRMs, but it can be extended to other machine types. Using the flux linkage as a state variable has multiple advantages: inherently taking into account the mutual coupling between the windings; easier implementation when using a nonlinear magnetic model; and simpler derivation of the controller gain matrices. The flux-linkage controller design and selected simulation results from Publication III are briefly presented below.

Fig. 3.2 shows the proposed flux-linkage controller structure. The measured current vector $\boldsymbol{i} = [i_\mathrm{td}, i_\mathrm{tq}, i'_\mathrm{fd}, i'_\mathrm{fq}]^\mathrm{T}$ and the reference current vector $\boldsymbol{i}_\mathrm{ref} = [i_\mathrm{td,ref}, i_\mathrm{tq,ref}, i'_\mathrm{fd,ref}, i'_\mathrm{fq,ref}]^\mathrm{T}$ are transformed into the corresponding flux-linkage estimate $\hat{\boldsymbol{\psi}}$ and reference flux-linkage $\boldsymbol{\psi}_\mathrm{ref}$ using a static mapping function $\boldsymbol{\psi}(\boldsymbol{i},x,y)$. The rotor displacement dependency x,y in the mapping function is optional and can be omitted for simplicity, resulting in the same

form as (2.11)

$$\boldsymbol{\psi}(\boldsymbol{i}) = \begin{bmatrix} \boldsymbol{\psi}_{\mathrm{t}}(\boldsymbol{i}_{\mathrm{t}}, \boldsymbol{i}'_{\mathrm{f}}) \\ \boldsymbol{\psi}_{\mathrm{f}}(\boldsymbol{i}_{\mathrm{t}}, \boldsymbol{i}'_{\mathrm{f}}) \end{bmatrix} = \begin{bmatrix} \psi_{\mathrm{td}}(i_{\mathrm{td}}, i_{\mathrm{tq}}, i'_{\mathrm{fd}}, i'_{\mathrm{fq}}) \\ \psi_{\mathrm{tq}}(i_{\mathrm{td}}, i_{\mathrm{tq}}, i'_{\mathrm{fd}}, i'_{\mathrm{fq}}) \\ \psi_{\mathrm{fd}}(i_{\mathrm{td}}, i_{\mathrm{tq}}, i'_{\mathrm{fd}}, i'_{\mathrm{fq}}) \\ \psi_{\mathrm{fq}}(i_{\mathrm{td}}, i_{\mathrm{tq}}, i'_{\mathrm{fd}}, i'_{\mathrm{fq}}) \end{bmatrix} \tag{3.2}$$

The mapping function linearizes the plant as seen by the controller and decouples the torque- and force-producing components. The mapping can be defined with FEM-based or measured data and implemented using, e.g., lookup tables or explicit functions.

The voltage equations in the synchronous coordinates are defined as

$$\frac{\mathrm{d}\boldsymbol{\psi}}{\mathrm{d}t} = \boldsymbol{u} - \boldsymbol{R}\boldsymbol{i} - \boldsymbol{\Omega}(\omega_{\mathrm{M}})\boldsymbol{\psi} \tag{3.3}$$

where

$$\boldsymbol{R} = \begin{bmatrix} R_{\mathrm{m}}\boldsymbol{I} & \boldsymbol{O} \\ \boldsymbol{O} & R_{\mathrm{s}}\boldsymbol{I} \end{bmatrix} \qquad \boldsymbol{\Omega}(\omega_{\mathrm{M}}) = \begin{bmatrix} 2\omega_{\mathrm{M}}\boldsymbol{J} & \boldsymbol{O} \\ \boldsymbol{O} & 2\omega_{\mathrm{M}}\boldsymbol{J} \end{bmatrix}$$

$\boldsymbol{I} = \left[\begin{smallmatrix} 1 & 0 \\ 0 & 1 \end{smallmatrix}\right]$ is a 2×2 identity matrix, and $\boldsymbol{O} = \left[\begin{smallmatrix} 0 & 0 \\ 0 & 0 \end{smallmatrix}\right]$ is a 2×2 zero matrix.

Following the internal model control (IMC) principle [73], the open-loop dynamics of the system are first canceled by using appropriate feedback compensations. Then, the feedback controller together with the feedforward compensator are designed to obtain the desired dynamics for the closed-loop system. The control law is given as

$$\boldsymbol{u}_{\mathrm{ref}} = -\left[\boldsymbol{K} - \boldsymbol{\Omega}(\omega_{\mathrm{M}})\right]\hat{\boldsymbol{\psi}} + \hat{\boldsymbol{R}}\boldsymbol{i} + \boldsymbol{K}_{\mathrm{I}}\boldsymbol{x}_{\mathrm{I}} + \boldsymbol{K}_{\mathrm{T}}\boldsymbol{\psi}_{\mathrm{ref}} \tag{3.4}$$

where $\boldsymbol{K}$, $\boldsymbol{K}_{\mathrm{I}}$, and $\boldsymbol{K}_{\mathrm{T}}$ are the controller matrices; $\hat{\boldsymbol{R}}$ is the resistance matrix estimate; and the integral state is defined as $\mathrm{d}\boldsymbol{x}_{\mathrm{I}}/\mathrm{d}t = \boldsymbol{\psi}_{\mathrm{ref}} - \hat{\boldsymbol{\psi}}$.

With accurate parameter estimates and mapping, the resulting closed-loop system can be shaped to have the desired dynamics. For example, if first-order dynamics are selected for each of the system states, then the desired closed-loop transfer-function matrix is

$$\boldsymbol{G}_{\mathrm{c}}(s) = \frac{\alpha_{\mathrm{c}}}{s + \alpha_{\mathrm{c}}}\boldsymbol{I}_4 \tag{3.5}$$

where $\boldsymbol{I}_4$ is a 4×4 identity matrix and α_{c} is the closed-loop system bandwidth. The desired closed-loop transfer function is realized by selecting the controller matrices as

$$\boldsymbol{K} = 2\alpha_{\mathrm{c}}\boldsymbol{I}_4 \qquad \boldsymbol{K}_{\mathrm{I}} = \alpha_{\mathrm{c}}^2\boldsymbol{I}_4 \qquad \boldsymbol{K}_{\mathrm{T}} = \alpha_{\mathrm{c}}\boldsymbol{I}_4 \tag{3.6}$$

Diagonal control matrices result in the decoupled closed-loop dynamics of each state variable. By changing (3.5), different closed-loop dynamics could be selected, e.g., different bandwidths can be chosen for the main and suspension windings. It is worth mentioning that not only model-based

control but also other approaches (e.g., [76], [77]) can be applied for the flux-linkage controller design. For conventional synchronous machines, a systematic flux-linkage controller design is presented in [78] including a direct discrete-time design.

3.3 Reference Calculation

The reference calculation methods are discussed separately for rotating SyRMs and for double-sided FSPM linear machines.

3.3.1 Rotating SyRMs

For bearingless SyRMs, the reference calculation block generates the current reference $\boldsymbol{i}_{\mathrm{ref}} = [i_{\mathrm{td,ref}}, i_{\mathrm{tq,ref}}, i'_{\mathrm{fd,ref}}, i'_{\mathrm{fq,ref}}]^{\mathrm{T}}$ for the inner control loop based on the torque reference $T_{\mathrm{M,ref}}$ and the radial force reference $\boldsymbol{F}_{\mathrm{ref}} = [F_{\mathrm{x,ref}}, F_{\mathrm{y,ref}}]$ coming from the outer control loop. The same reference calculation methods are applicable for machines with separated windings as well as combined windings.

The reference calculation can be performed based on the textbook model described in Section 2.3.1 [5]. When the torque reference is known, the current references $i_{\mathrm{td,ref}}$ and $i_{\mathrm{tq,ref}}$ can be solved from (2.10), e.g., by applying the maximum-torque-per-ampere (MTPA) principle. Alternatively, a constant magnetization $i_{\mathrm{td,ref}}$ may be selected, then $i_{\mathrm{tq,ref}}$ is calculated from (2.10) as

$$i_{\mathrm{tq,ref}} = \frac{T_{\mathrm{M,ref}}}{3(L_{\mathrm{d}} - L_{\mathrm{q}})i_{\mathrm{td,ref}}} \tag{3.7}$$

When $i_{\mathrm{td,ref}}$ and $i_{\mathrm{tq,ref}}$ are obtained and the radial force reference $\boldsymbol{F}_{\mathrm{ref}}$ is given, then $i'_{\mathrm{fd,ref}}$ and $i'_{\mathrm{fq,ref}}$ can be calculated based on (2.9) as

$$\boldsymbol{i}'_{\mathrm{f,ref}} = \begin{bmatrix} i'_{\mathrm{fd,ref}} \\ i'_{\mathrm{fq,ref}} \end{bmatrix} = \begin{bmatrix} M_{\mathrm{d}} i_{\mathrm{td,ref}} & M_{\mathrm{q}} i_{\mathrm{tq,ref}} \\ M_{\mathrm{q}} i_{\mathrm{tq,ref}} & -M_{\mathrm{d}} i_{\mathrm{td,ref}} \end{bmatrix}^{-1} \begin{bmatrix} F_{\mathrm{x,ref}} \\ F_{\mathrm{y,ref}} \end{bmatrix} \tag{3.8}$$

In addition, SyRMs with combined windings should respect the upper limits of $i'_{\mathrm{fd,ref}} \leq i_{\mathrm{td,ref}}$ and $i'_{\mathrm{fq,ref}} \leq i_{\mathrm{td,ref}}$, as further increase in force producing currents would reverse the direction of the flux and lower the radial force instead of increasing it. SyRMs with separated windings have a similar upper limit on the force-producing currents, which should be defined based on the number of turns in the main and suspension windings.

The method of reference calculation presented above relies on the accuracy of the textbook model with constant parameters. In Publication III, the magnetic model from Section 2.3.2 is applied in the reference calculation. Explicit-function-based parameters (2.12) replace the constant parameters in (3.7) and (3.8). In this way, the reference calculation accounts for the variation in inductances and force constants due to the saturation.

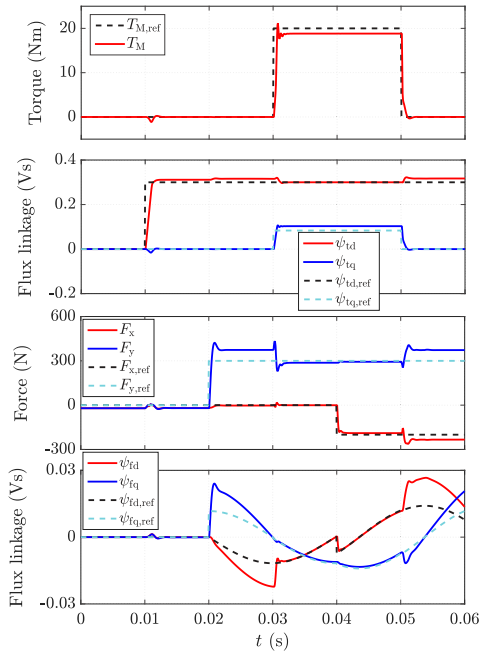

(a)

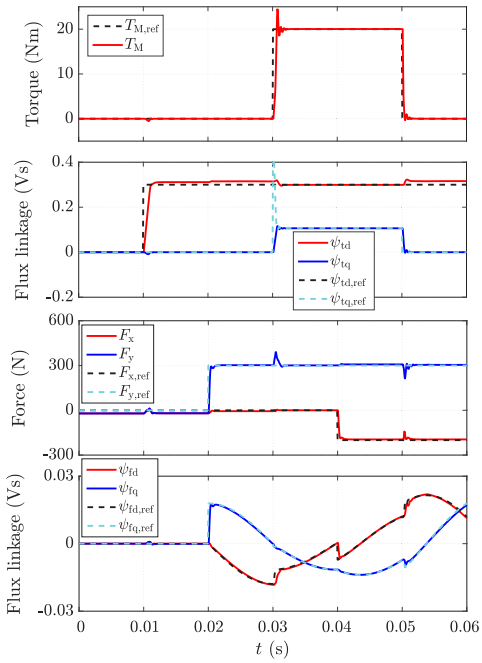

(b)

Figure 3.3. Simulation results with the proposed flux-linkage controller and the reference calculation based on (a) a constant parameter magnetic model and (b) an explicit-function-based magnetic model (2.12). The subplots show with solid lines the torque T_M, the radial forces F_x,F_y, and the flux linkages ψ_{td},ψ_{tq},ψ_{fd},ψ_{fq} produced by the machine. The respective references from the control system are shown with dashed lines.

Fig. 3.3 shows the time-domain simulation results of a model-based torque and radial force control system. In this simulation, the outer control loop is left out, and the torque and force references are defined directly by the user. The reference calculation is performed with (3.7) and (3.8). The inner control loop is realized with a discrete-time implementation of the flux-linkage controller, as described in Section IV of Publication III. The bandwidth of the flux-linkage controller is $\alpha_c = 2\pi \cdot 600$ rad/s, and the switching frequency is $f_{sw} = 8$ kHz. The plant model is based on the example bearingless SyRM considered in Section 2.3.2. The plant model consists of voltage equations (2.6) and FEM-based four-dimensional lookup tables to represent the magnetic model and calculate the produced radial forces. Motor torque is calculated with (2.10) based on the current and flux-linkage information.

The simulation sequence consists of stepping the magnetization reference $i_{td,ref}$ from 0 to 20 A at 0.01 s, stepping the y-axis radial force reference $F_{y,ref}$ from 0 to 300 N at 0.02 s, stepping the torque reference $T_{M,ref}$ from 0 to 20 Nm at 0.03 s and back to 0 at 0.05 s, and finally stepping the x-axis radial force reference $F_{x,ref}$ from 0 to −200 N at 0.04 s.

Fig. 3.3(a) shows the simulation results when constant parameters are used in the reference calculation and in the flux-linkage controller. Fig. 3.3(b) shows the results when an explicit-function-based magnetic model is applied in the reference calculation and in the flux-linkage controller. As can be seen from this comparison, using explicit-function based parameters in the reference calculation reduces the steady-state error in the torque and the radial force as compared to using constant parameters. Using an explicit-function-based magnetic model in the mapping function $\boldsymbol{\psi}(\boldsymbol{i})$ of the flux-linkage controller means that the controller tuning is not affected by the magnetic saturation. Hence, the controller performance remains the same throughout the operating range of the machine in terms of allowable currents.

Reference calculation methods presented thus far do not take into account the rotor eccentricity. An eccentric rotor results in changing magnetic model parameters and also introduces UMP, which can be thought of as a disturbance force. The change in magnetic model parameters can be accounted for in the static mapping function of the flux-linkage controller $\boldsymbol{\psi}(\boldsymbol{i}, x, y)$ as well as in the reference calculation process by introducing the dependency of the parameters in (3.7) and (3.8) on x and y. If the UMP can be quantified in real-time, it can be compensated simply by subtracting the x and y components of the UMP from the corresponding force references $F_{x,ref}$ and $F_{y,ref}$ used in (3.8).

Moreover, the eccentricity modeling method presented in Section 2.3.3 can be applied to control design. This would result in the eccentricity effects being inherently included in the reference calculation. This topic, however, is left for future research.

3.3.2 Double-Sided Linear FSPM Machines

A schematic of a bearingless double-sided linear FSPM machine system is shown in Fig. 2.16. The reference calculation involves calculating the reference current components $[i_{\mathrm{d1,ref}}, i_{\mathrm{q1,ref}}]$ and $[i_{\mathrm{d2,ref}}, i_{\mathrm{q2,ref}}]$ for the two opposing linear machine units based on the force references. When the total thrust force reference $\Sigma F_{\mathrm{x,ref}}$ and the differential attraction force reference $\Delta F_{\mathrm{y,ref}}$ are known, the reference forces for each machine unit can be defined based on (2.35) as

$$F_{\mathrm{x1,ref}} = F_{\mathrm{x2,ref}} = \Sigma F_{\mathrm{x,ref}}/2 \tag{3.9a}$$

$$F_{\mathrm{y1,ref}} = F_0 - \Delta F_{\mathrm{y,ref}}/2 \tag{3.9b}$$

$$F_{\mathrm{y2,ref}} = F_0 + \Delta F_{\mathrm{y,ref}}/2 \tag{3.9c}$$

where F_0 is a common-mode attraction-force component, which can be arbitrarily selected within the boundaries of the maximum motor current.

The current references are then calculated based on the force expressions of a single linear FSPM machine unit. For example, the current references can be derived based on the modeling results from Section 2.4 using equations (2.29a) and (2.34) and the proposed magnetic model of the machine. In this way, the magnetic self-axis and cross-axis saturation and the effect of the air gap variation are inherently compensated for in the reference calculation.

In Publication VI, the described method of reference calculation was applied in the control system of a bearingless double-sided FSPM linear machine system. The force expressions (2.29a) and (2.34) were approximated for easier real-time implementation and used together with the air gap feedback to calculate the current references.

3.4 Outer Control Loop

After the inner control loop and the reference calculation are properly designed and implemented, the system, in an ideal case, becomes linear and decoupled as seen from the interfaces of the outer control loop. Hence, the levitation and rotation/propulsion controllers can be designed and tuned independently of each other using any single-input single-output (SISO) control method for linear time-invariant systems.

3.4.1 Rotation/Propulsion Control

In this dissertation, the rotation/propulsion control system is considered independently of the levitation control. Hence, the same methods can be employed for designing the rotation/propulsion control system as are

used for conventional rotating/linear electric machines, e.g., [79] and [37]. Since this topic is outside of the main scope of this dissertation, simple PI speed controllers were used to conduct the experiments with the prototype bearingless machines.

3.4.2 Levitation Control

The performance of the levitation control loop is critical to maintaining stable levitation of the bearingless system. It is designed to stabilize the system under all possible operating conditions, which involves compensating for the inherent negative stiffness of the electromechanical system, providing additional damping, and rejecting disturbances.

In the literature, the levitation control is most commonly realized with PID-type controllers, where each DOF is stabilized by one SISO controller. Such a levitation control strategy is employed, for example, in [80], [81], [82], [27], and [83]. The popularity of PID controllers is mostly due to their simplicity, while being sufficient for stable levitation in most applications. The levitation performance obtained with a PID controller can be comparable to that of more complicated methods, e.g., H_∞ control, as demonstrated in [84]. However, the tuning of the PID controllers in practice is usually hindered by the lack of analytical tuning rules and is often done by a trial-and-error approach. Hence, this approach can make it difficult to design a motion controller with the desired predefined dynamics.

A model-based control design of a rotating bearingless motor is presented in a simulation study [85]. In [72] and [86], a MIMO model-based control approach is proposed, including a state-feedback method and linear-quadratic regulator (LQR). While presenting interesting results, these studies do not include analytical rules for the controller and estimator tuning and do not discuss pole placement in detail.

A direct discrete-time design of a state-feedback control system is presented in Publication VI. Analytical design rules for the levitation controller are presented, including the calculation of the feedback gains and the state observer gains. Pole placement considerations are also discussed. An example controller design is carried out for a double-sided bearingless linear motor and verified using experiments. The experimental results in Publication V are obtained by employing the same control method.

The proposed state feedback controller structure is shown in Fig. 3.4. The controller consists of an integrator with a gain k_I, a state feedback with a gain $\boldsymbol{K}_\mathrm{fb} = [k_1, k_2]$, and a full-order state observer. The shaded area shows the limiting of the force reference and an anti-windup scheme using back-calculation.

Here, the controller is presented as applied to a double-sided bearingless linear system. In this case, the differential air gap Δy is used as a feedback signal, and the differential force reference $\Delta F_{\mathrm{y,ref}}$ is the output of the con-

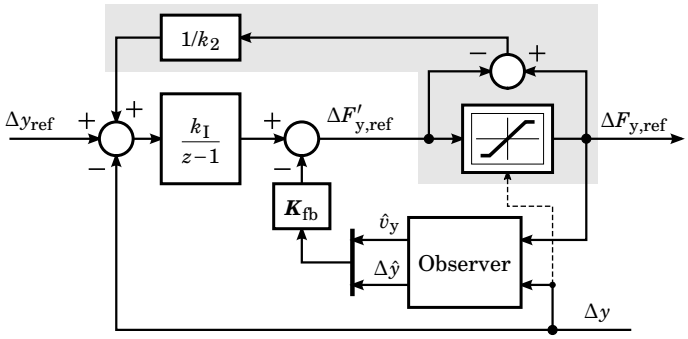

Figure 3.4. Proposed state-feedback levitation controller for a double-sided bearingless linear motor. The shaded area shows a back-calculation anti-windup mechanism. This controller structure is also applicable for one-axis levitation control of a rotating bearingless machine.

troller. Likewise, the proposed controller can easily be adapted to rotating bearingless machines by using two instances of the controller, with rotor coordinates x and y as feedback and radial force references $F_{\mathrm{x,ref}}$ and $F_{\mathrm{y,ref}}$ as outputs.

The mechanical model presented in Section 2.1 and 2.4.4 is used as a basis for model-based controller synthesis. A detailed derivation of the control law is given in Publication VI.

The closed loop system has three states: the differential air gap Δy, the linear velocity v_{y}, and the integral state Δy_{I}. Hence, there are three poles to be placed. The poles are divided into one real pole and a pair of complex poles. Thus, the characteristic polynomial of the closed loop system is of the form $B_{\mathrm{fb}}(z) = (z + a_{\mathrm{z}})(z^2 + b_{\mathrm{z}}z + c_{\mathrm{z}})$, which results in a simple calculation of the feedback gains:

$$k_1 = m\frac{a_{\mathrm{z}} - b_{\mathrm{z}} + c_{\mathrm{z}} + 7}{4T_{\mathrm{s}}} \quad k_2 = m\frac{3a_{\mathrm{z}} + b_{\mathrm{z}} - c_{\mathrm{z}} + 5}{2T_{\mathrm{s}}^2} \quad k_{\mathrm{I}} = m\frac{a_{\mathrm{z}} + b_{\mathrm{z}} + c_{\mathrm{z}} + 1}{T_{\mathrm{s}}^2} \tag{3.10}$$

where T_{s} is the sampling interval of the levitation control system.

The system state corresponding to linear velocity usually cannot be directly measured and, hence, needs to be estimated. A common solution is using a derivative of the position signal. However, this approach amplifies the noise of the position measurement signal. To attenuate the noise, a low pass filter may be used; however, this introduces additional delay in the feedback loop and deteriorates the levitation control performance.

A full-order state observer is a more elaborate approach to obtain the velocity information. Based on the desired second-order characteristic polynomial $B_{\mathrm{o}}(z) = z^2 + d_{\mathrm{z}}z + e_{\mathrm{z}}$, the observer gains are calculated as

$$l_1 = (e_{\mathrm{z}} + d_{\mathrm{z}} + 1)/T_{\mathrm{s}} \qquad l_2 = d_{\mathrm{z}} + 2 \tag{3.11}$$

The coefficients a_{z}, b_{z}, c_{z}, d_{z}, and e_{z} in (3.10) and (3.11) are selected according to the pole placement recommendations, which are discussed in the following section.

3.5 Pole Placement Considerations

In order to tune the proposed flux-linkage and levitation controllers, a pole placement method is utilized. Also, more involved alternatives, for example, LQR or robust control methods [87], can be applied for controller tuning. The control system is intended to be implemented on a digital computer and executed with a fixed sampling frequency. Hence, the sampling time imposes an upper limit on the bandwidth of the control system. Pole locations should be selected starting from the innermost control loop and moving to the outermost control loop. In the considered cascaded control structure, the inner and outer control loops are designed independently of each other. To ensure sufficient separation of the dynamics of the outer and inner control loops, the poles of the inner control loop should preferably have at least ten times higher natural frequency than the poles of the outer control loop.

The flux-linkage controller bandwidth α_c in (3.6) should be selected according to $\alpha_c < \pi/(10T_{sc})$, where T_{sc} is the sampling interval of the inner control loop. Bearing in mind this condition, the bandwidth α_c can be set as high as possible, since it defines the upper limit for the bandwidth of the outer control loop. One of the few situations when it is advisable to lower the bandwidth of the flux-linkage controller is in the case of a high noise content in the measured current, which can cause audible noise and high frequency vibrations when amplified by the controller. Also, lowering the bandwidth can improve the robustness against the parameter errors.

For the levitation control system, the pole locations are easier to choose in the continuous-time domain, with subsequent mapping to discrete time. The controller and the observer characteristic polynomials in the continuous-time domain can be expressed together as

$$\begin{aligned} B(s) &= (s+a_p)(s^2+b_c s+c_c)(s^2+d_c s+e_c) \\ &= (s+a_p)(s^2+2\zeta_s\omega_s s+\omega_s^2)(s^2+2\zeta_o\omega_o s+\omega_o^2) \end{aligned} \tag{3.12}$$

where a_p, b_c, c_c, d_c, and e_c are the coefficients to be decided. The standard form representation is used for the second order polynomials with the coefficients ω_s, ζ_s, ω_o, and ζ_o.

The complex-conjugate poles of $s^2+2\zeta_s\omega_s s+\omega_s^2$ are treated as faster poles related to the linear velocity control. When $0.6 < \zeta_s < 0.9$ is selected according to the desired damping ratio, ω_s represents the approximate bandwidth of the speed-control loop and can be selected according to $\omega_s < \alpha_c/10$.

The real-valued pole $s = -a_p$ represents the air-gap regulation dynamics, a_p being the approximate bandwidth. This pole can be selected slower than ω_s according to $a_p < \omega_s/10$. Such a pole placement ensures levitation stability with a faster and well-damped pole-pair corresponding to ω_s. The slower pole a_p is moved only slightly in order to avoid unnecessarily increasing the control effort.

The remaining polynomial $s^2 + 2\zeta_o\omega_o s + \omega_o^2$ is related to the observer poles. The selection of ω_o in the range $2\omega_s < \omega_o < \alpha_c/2$ is a compromise between the measurement-noise amplification and the effect of the observer on the dynamic response of the overall control system. If the noise content in the position measurement is low, a high value can be selected for ω_o which will ensure minimal influence of the observer on the overall control system performance.

Additional considerations for the tuning of the levitation controller may arise from the specific application requirements or unmodeled effects. For example, in Publication VI, the bandwidth of the faster pole-pair corresponding to ω_s was lowered in order to avoid exciting the bending mode of the rail in the low-frequency range.

Finally, after the pole locations in the continuous-time domain have been selected, the coefficients are mapped to their exact discrete-time equivalents as

$$
\begin{aligned}
a_z &= -\mathrm{e}^{-a_p T_s} \\
b_z &= -2\mathrm{e}^{-b_c T_s/2}\cos\left(T_s\sqrt{c_c - b_c^2/4}\right) \qquad & c_z &= \mathrm{e}^{-b_c T_s} \\
d_z &= -2\mathrm{e}^{-d_c T_s/2}\cos\left(T_s\sqrt{e_c - d_c^2/4}\right) \qquad & e_z &= \mathrm{e}^{-d_c T_s}
\end{aligned}
\tag{3.13}
$$

4. Experimental Bearingless Setups

This chapter describes the prototype bearingless machines that were used in the scope of this dissertation for the experimental validation of the results. The chapter provides an overview of the experimental setups and describes the utilized hardware, system parameters, and implementation-related issues. The three studied prototypes are:

- Bearingless 4.7-kW SyRM with separated windings;
- Bearingless slice SyRM with combined windings;
- Bearingless linear motor system based on linear FSPM machines.

4.1 4.7-kW SyRM with Separated Windings

The overview of this experimental setup is shown in Fig. 4.1. The studied machine type is a synchronous reluctance motor with a four-pole multi-flux-barrier rotor. The details of the machine design are reported in [88]. Two three-phase windings are sinusoidally distributed in the stator slots: a four-pole main winding for the torque production and a two-pole suspension winding for the radial force production. Out of the available slot space, approximately 80% is occupied by the main winding and 20% by the suspension winding. Both windings are star-connected and supplied independently by two three-phase PWM-operated inverters. The DC-link voltage for the main winding inverter is 400 V, while the suspension winding inverter has a DC-link voltage of 60 V. The suspension winding typically operates at low voltage, because it does not need to overcome the rotation-induced back-EMF and usually carries relatively low currents. Using the 400 V DC-link for the suspension winding would result in very narrow voltage pulses. Lowering the DC-link voltage increases the useful pulse-width modulation resolution in the low voltage range.

The mechanical arrangement is presented in Fig. 4.1(a). Both ends of the prototype machine are supported with AMBs. This helps with the initial

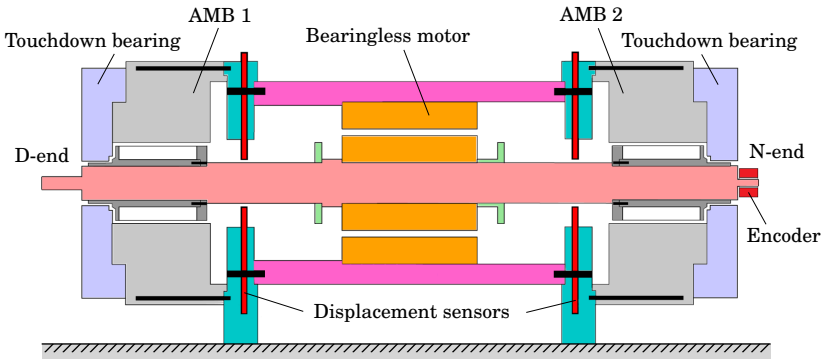

(a)

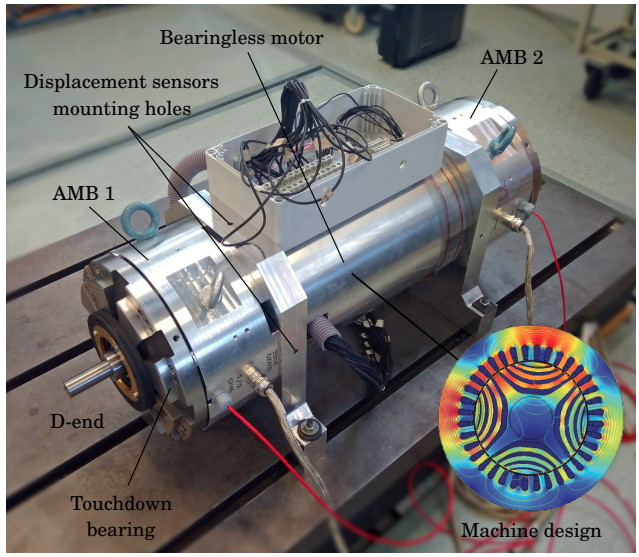

(b)

Figure 4.1. Overview of the bearingless 4.7-kW SyRM setup: (a) mechanical drawing showing the main components of the assembly and (b) photograph of the test setup and a drawing of the machine geometry.

testing of the control system and makes it possible to indirectly measure the radial forces produced by the bearingless motor without operating the machine in the levitation-control mode. Mechanical touchdown bearings support the rotor at rest and provide safe touchdown in case of levitation control failure during operation.

The control algorithm was developed in the Matlab/Simulink environment and implemented on a dSPACE MicroLabBox rapid prototyping platform for real-time execution. The gate signals generated by the control system are passed to the inverters through the appropriate interface boards. The main winding was supplied by an ABB ACS880 inverter. The suspension winding was supplied by an ABB ACSM1 inverter, which was modified to work with a 60 V DC-link voltage. The feedback signals for

the control system include phase current measurements from the main and suspension windings; DC-link voltage measurements of the main and suspension inverters; the rotation angle of the rotor; and the radial position of the rotor in the xy coordinates. The measured quantities are sampled synchronously with the PWM.

The rotation angle is measured using an incremental encoder attached to the non-drive end of the shaft. The radial position of the rotor is measured at the shaft using eight proximity probes in total—two groups of four probes placed at both sides of the bearingless machine. The sensors are eddy current type 3300 XL 8mm proximity transducers from Bently Nevada. Radial displacement along one axis is obtained with a differential reading from two opposing sensors. The differential measurement compensates for rotor manufacturing imperfections and for possible thermal expansion of the rotor.

This machine design was used in Publication II as a basis for FEM analysis and for deriving the system model, and in Publication III for the time-domain simulation study. Experimental levitation results from this machine have not been published before and are presented for the first time in this dissertation.

4.2 Slice SyRM with Combined Windings

The test setup for a prototype bearingless slice SyRM is shown in Fig. 4.2 together with the machine geometry. Due to the slice motor structure, the disk-shaped rotor is passively stabilized in the axial movement and tilting degrees of freedom. The machine has a four-pole reluctance rotor with flux barriers and a stator with six slots and a double-layer concentrated winding. The machine geometry is based on the design presented in [89] and [90]. The main motor dimensions and system parameters are listed in Table 4.1. Bearingless operation is achieved by using the combined winding structure. Six phases of the machine are arranged into two independent star connections and supplied with a PWM-operated inverter with six half-bridges. The method to superimpose the torque-producing and force-producing currents into the combined winding is described in Publication V.

The measured signals from the motor include six phase currents, DC-link voltage, the rotor radial position, and the rotor angle. These signals are fed back into the control system for real-time levitation and rotation control. Real-time control is implemented on a digital signal processor (DSP) TMS320F28335 by Texas Instruments. The DSP and the power inverter are integrated into a control unit LCM-ECU-10HB-10A provided by Linz Center of Mechatronics. The control unit also includes the necessary hardware for voltage and current measurement; analog-to-digital converters for sampling the rotor position and angle sensors; and a communication

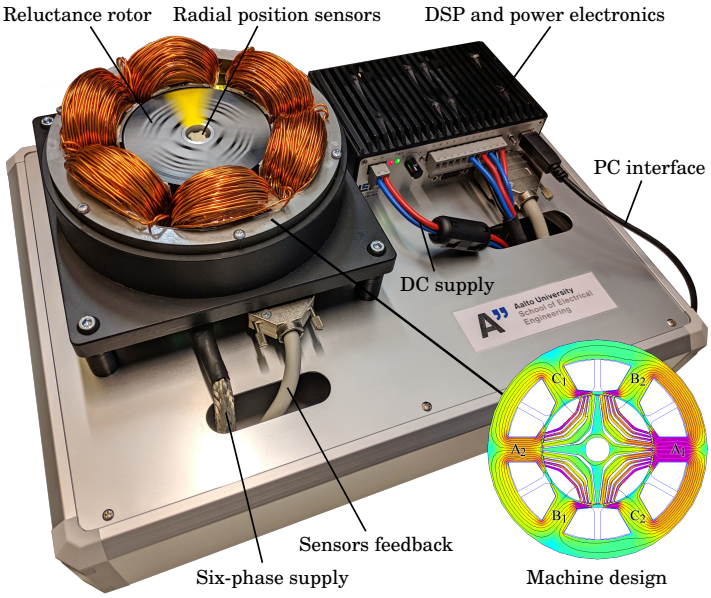

Figure 4.2. Photograph of the test setup for the prototype bearingless slice SyRM with combined windings. Drawing of the bearingless machine design is also shown.

interface for programming and monitoring purposes. The control system was developed using the Matlab/Simulink environment. X2C software for Matlab was utilized for code generation and for programming the DSP.

Table 4.1. Parameters of the bearingless slice SyRM.

Parameter	Value	Unit
Airgap	1	mm
Rotor outer diameter	80	mm
Stator outer diameter	160	mm
Rotor and stator stack lengths	10	mm
Rotor weight	0.25	kg
DC-link voltage	60	V
Continuous RMS current	6	A
Number of wire turns per coil	200	

The radial position of the rotor is measured with four eddy current type displacement sensors. Four printed circuit board coils are mounted on a stationary post in the center of the rotor and measure rotor displacement against a polished aluminum insert fixed to the rotor. An analog circuit is utilized to obtain the displacement information using the method presented in [91].

Implementing a reliable and contactless rotor angle measurement is

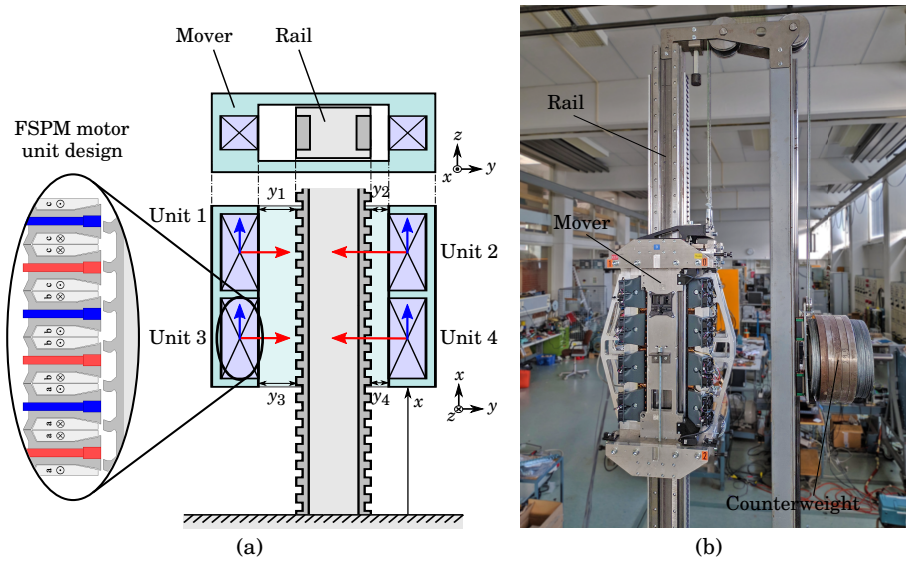

Figure 4.3. Overview of the linear bearingless system setup: (a) a mechanical drawing showing the arrangement of four FSPM motor units on two sides of the vertical rail with red and blue arrows denoting the normal and thrust forces of the motor units respectively and (b) a photograph of the test setup.

challenging, since the reluctance rotor does not produce its own magnetic field. An axially magnetized multi-pole PM ring was attached concentrically to the bottom side of the rotor. Four analog Hall effect sensors are placed under the rotor in order to measure the variation of the flux from the PM ring. Finally, the atan2 function is used to obtain the rotor angle. The filtered derivative of the angle provides the speed information. This solution was implemented with an 18-pole PM ring RMSI30.9-18A-F from BOGEN Electronic and SS495A Hall sensors from Honeywell.

The experimental results from this setup are presented in Publication V along with the description of the control algorithm and system parameters.

4.3 Linear FSPM Motor System

In this experimental setup, four linear motor units are mechanically connected to form a linear bearingless system, as shown in Fig. 4.3(a). The mover consists of four three-phase linear FSPM motors arranged in a double-sided configuration around a fixed vertical rail. Each motor unit is supplied with a separate three-phase power inverter. The machine design is shown in Fig. 4.3(a). One motor unit consists of 12 mover slots and 14 rail poles. Additional teeth are included at both ends of the mover to reduce the end effects. The mover travels along the rail in the x-direction by using the thrust force produced by each motor unit. At the same time,

Table 4.2. Parameters of the bearingless linear FSPM motor system.

Parameter	Value	Unit
Nominal air gap	1.05	mm
Total mover mass	100	kg
Nominal thrust force of each unit	600	N
Continuous RMS current	10	A
Nominal travel speed	1	m/s

the attraction force of each motor unit towards the rail can be controlled to achieve contactless operation. In the experimental setup, three degrees of freedom are actively controlled: levitation along the y-axis, tilting around the z-axis, and movement along the x-axis. Rotation around the x-axis, tilting around the y-axis, and movement along the z-axis are mechanically prevented with linear bearings. A counterweight is used to compensate for the gravitational force acting on the mover. Fig. 4.3(b) shows a photograph of the test setup. The main system parameters are listed in Table 4.2.

The levitation and propulsion control systems receive real-time feedback in the form of the DC-link voltages and phase currents of each motor unit, linear x-axis position along the rail, and air gap length of each motor unit. The linear position of the mover and the air gaps are measured with eddy current sensors. The linear position is determined by measuring the magnetic saliency of the rail teeth. The air gap information is obtained by measuring against a flat aluminum strip placed along the rail. The control system is designed using Matlab/Simulink and implemented on a programmable logic controller from Beckhoff. The code for the control algorithm is generated and programmed using TwinCAT software. The power inverters are also supplied by Beckhoff.

The differential normal force measurements are carried out by mechanically fixing the mover into the desired constant y position using load cells, which also provide the force measurement while the currents can be varied arbitrarily.

This experimental setup was used for testing the control system and the feedback linearization method in Publication VI. Normal force and back-EMF measurements from this experimental setup were used for validating the modeling approach in Publication VII.

5. Example Experimental Results

The control system described in Chapter 3 was implemented in discrete time for real-time execution and applied to three bearingless machine systems described in Chapter 4. This section presents selected experimental results from the levitation tests and discusses the most important control system aspects for each prototype machine.

5.1 4.7-kW SyRM with Separated Windings

The experimental results obtained from the bearingless 4.7-kW SyRM prototype are shown in Fig. 5.1. The rotor lift-up test is shown in Fig. 5.1(a), including rotor displacements and currents. Because the machine is horizontally mounted, prior to the lift-up, the force of gravity keeps the rotor resting on the safety bearings at a negative y-axis displacement.

The x-axis position is regulated to 0 and the y-axis position is regulated to +0.1 mm in order to have the gravity force partially canceled out by the UMP and to reduce the steady-state suspension-winding current.

After the levitation is established, the machine is accelerated up to the nominal rotation speed of 157.08 rad/s as shown in Fig. 5.1(b). The nominal speed is reached in less than 2 s while maintaining stable levitation with very little radial rotor movement. During the spin-up, the magnetizing current i_{td} is gradually increased from 5 A to 10 A which improves the levitation stability at high rotation speeds.

Due to the distributed windings structure, the force production of this prototype machine is accurate and predictable. Hence, the levitation control is relatively simple to implement and tune. Successful experimental tests are also facilitated by the accurate and low-noise position and current sensing hardware.

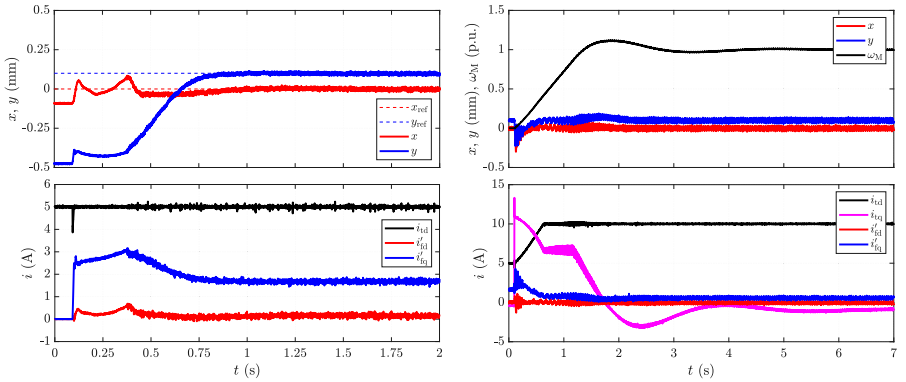

Figure 5.1. Experimental results of a prototype 4.7-kW bearingless SyRM with separated windings: (a) the lift-up test showing the rotor transition to the centric position and current components during the transient and (b) the acceleration to the nominal rotation speed of 157.08 rad/s during active levitation control.

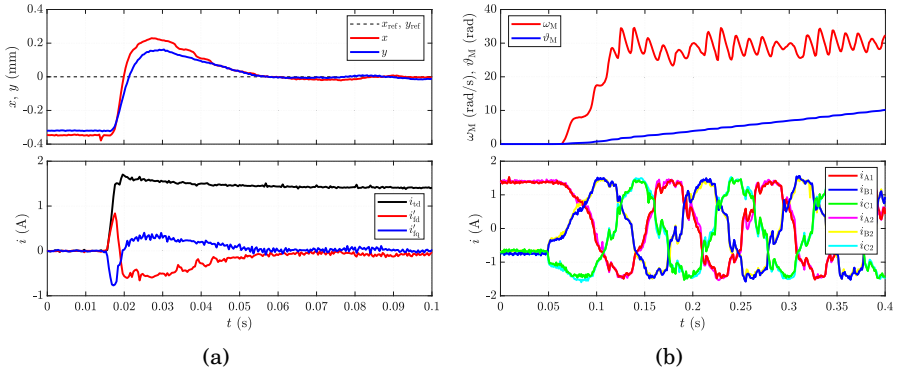

Figure 5.2. Experimental results of a prototype bearingless slice SyRM with combined windings: (a) the lift-up test showing the rotor transition to centric position and current components during the transient and (b) the rotation test during active levitation control. A speed reference step of 30 rad/s is applied at $t = 0.05$ s.

5.2 Slice SyRM with Combined Windings

Experimental results obtained from the bearingless slice SyRM prototype are shown in Fig. 5.2. The rotor lift-up transient is shown in Fig. 5.2(a). This prototype machine has the axis of rotation positioned vertically; hence, the xy movement is not influenced by the force of gravity. While the rotor is levitated in the centric position, the motor is accelerated up to 30 rad/s, as demonstrated in Fig. 5.2(b), which shows the rotor speed ω_M, the rotor angle ϑ_M, and instantaneous phase currents. The ripple in the measured speed signal is due to an imprecise spatial distribution of Hall-effect sensors that are used for measuring the rotor angle and speed. Nevertheless, stable levitation is maintained at this rotation speed. Higher rotation

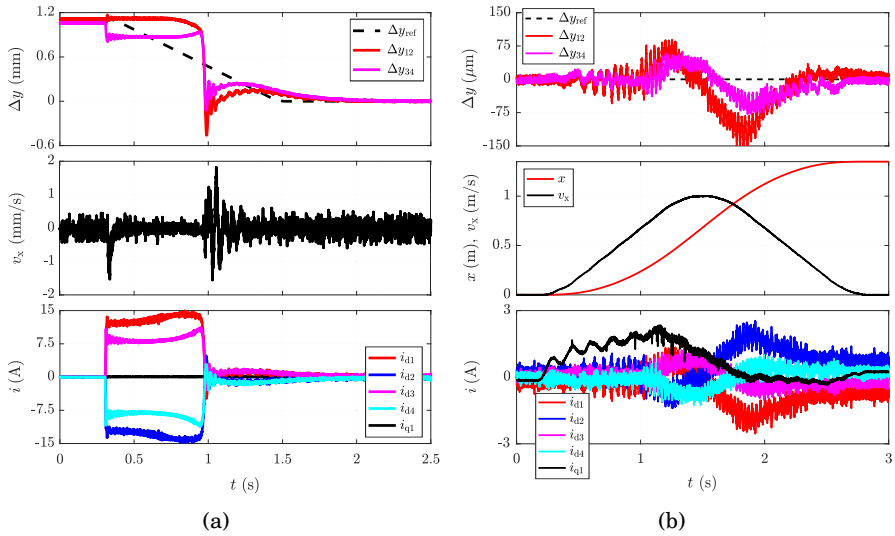

(a) (b)

Figure 5.3. Experimental results of a prototype bearingless linear motor system based on FSPM machines: (a) the lift-up test with reference shaping for smoother transition to levitation and (b) the propulsion test while maintaining active levitation.

speeds were not achieved with this prototype, due to a tilting instability that occurs when the rotation speed reaches approximately 60 rad/s.

The use of concentrated winding in the design of this prototype SyRM results in a relatively high inaccuracy in the radial force production, which complicates the control system design and tuning.

5.3 Linear FSPM Motor System

Experimental results obtained from the bearingless linear FSPM motor system are shown in Fig. 5.3. Fig. 5.3(a) shows the levitation start. The upper subplot shows the differential air gaps of the upper and lower machine unit pairs, as denoted by Δy_{12} and Δy_{34}, respectively. The magnetizing currents i_{d} of each machine unit (which are used to control the attraction force) are shown in the bottom subplot and denoted with i_{d1}, i_{d2}, i_{d3}, and i_{d4}. The thrust-force producing currents i_{q} are controlled to be equal for each machine unit; hence, only i_{q1} is shown. Before the lift-up, the mover is held attached to the rail by the attraction forces due to the PMs. The levitation control is enabled at $t = 0.3$ s. However, the currents immediately requested by the levitation controller do not produce sufficient force to overcome the attraction force due to the PMs. Because of the integral action of the levitation controller, the currents continue to slowly rise until approximately $t = 1$ s. At this point, the mover detaches from the rail and both differential air gaps are regulated to 0.

Fig. 5.3(b) shows the results of a thrust-direction movement test. The mover levitation is kept stable, while it travels 1.3 m along the rail reaching the nominal speed of $v_x = 1$ m/s.

This prototype bearingless system has been shown to be the most demanding out of the studied machines in terms of the control system design. This is mostly due to high inherent negative stiffness. A complicated and saturating magnetic circuit results in non-linear force production with respect to both the air gap and the currents, which further complicates the control system design. Proper dynamic modeling and feedback linearization has proven to be an important tool in stabilizing the levitation control of this prototype.

Most recently, the existing experimental setup was extended to a four-sided system with eight machine units and has been used in [92] to demonstrate stable levitation in all six degrees of freedom.

6. Summary of Publications

6.1 Abstracts

The abstracts of the publications are reprinted in this section. Publication I deals with flywheel energy storage. Publications II, III, and IV deal with bearingless SyRMs with separated windings. Publication V deals with bearingless SyRMs with combined windings. Publications VI and VII deal with bearingless FSPM linear machines.

Publication I

This paper presents a novel analytical method for electro-mechanical design of a high speed long-term flywheel energy storage system and thermal evaluation of possible operating modes of the system. Flywheel's composite shell rotor along with the motor/generator unit are assumed to be placed into a sealed vacuum chamber, which presents a challenge of heat transfer, produced by rotor losses. Developed method takes into account thermal radiation properties of the rotor and is realized using Mathcad software, which allows for quick investigation of any flywheel configuration. The method involves calculations for preliminary rotor sizing and determining achievable operation modes, while keeping the rotor under a specified temperature limit. Results of using this method for studying dependencies of thermal performance on initial system parameters are presented and conclusions are drawn. Based on the conducted study, recommendations on system design considerations are given.

Publication II

This paper deals with magnetic modeling of a bearingless synchronous reluctance motor. The motor under consideration includes two separate sets of three-phase windings, one for torque production and the other one

for radial-force production. This paper demonstrates by means of finite-element analysis, that it is unrealistic to assume the two three-phase windings to be decoupled from one another. Instead, it is shown that especially the torque-producing winding currents affect to the operation of the radial-force producing winding. A simple nine-parameter explicit-function based magnetic model is proposed to model the cross-saturation between the two winding sets. The effectiveness of the proposed magnetic model is demonstrated by applying it together with model-based torque and radial-force controllers.

Publication III

This paper deals with a model-based state-space flux-linkage control of a dual three-phase-winding bearingless synchronous reluctance motor. Analytical tuning rules for the state feedback, integral action, and reference feedforward gains are derived in the continuous-time domain. The proposed method is easy to apply: the desired closed-loop bandwidth together with the estimated magnetic-model of the motor are required. Furthermore, the proposed method automatically takes into account the mutual coupling between the two windings. A simple digital implementation is provided and the robustness of the proposed control method against the system parameter inaccuracies and eccentric rotor positions is analyzed. The proposed controller design is evaluated by means of simulations by keeping in mind the most important aspects related to an experimental evaluation.

Publication IV

This paper deals with modelling of rotor eccentricity in a dual three-phase winding bearingless synchronous reluctance motors (BSyRMs). The motor includes two separate sets of three-phase windings: one for torque production and the other one for radial force production. For this motor, an improved analytical model with linear magnetic material is presented. The accuracy of the model depends on the accuracy of the inverse airgap function. Typically, a series expansion is used for approximating the inverse-airgap function. In order to make the main-winding inductances depend on the radial position, at least the first two terms have to be included in the expansion, enabling calculation of the radial forces caused by unbalanced magnetic pull. The improved model is applicable, e.g., for stability analysis, time-domain simulations, or developing real-time control methods.

Publication V

This paper deals with modeling of bearingless synchronous reluctance motors with a combined winding. A method to link an existing model used for the separated windings structure to the combined winding structure is proposed. A dynamic model applicable for the purposes of time-domain simulation, model-based control design, and real-time control is presented. The finite-element method (FEM) is used to validate the proposed model and to show the feasibility of the considered slice motor type, including passive stability of axial movement and tilting, force and torque production, and ripple. Applicability of the developed model in control design is demonstrated. The model is validated by means of experiments.

Publication VI

This paper deals with levitation control for a double-sided bearingless linear-motor system. Analytical design rules for a state-feedback gain and a state observer are derived. To decouple the production of forces in thrust- and normal-force directions, feedback-linearizing control based on the magnetic model is proposed. The proposed control design is tested in an experimental system consisting of four individually supplied linear-motor units in a double-sided configuration. The results from time-domain simulations and experimental tests suggest that the proposed control design can successfully provide smooth transition to contactless operation and retain the stable levitation during the movement in the thrust-force direction.

Publication VII

This paper deals with dynamic models for three-phase bearingless flux-switching permanent-magnet (FSPM) linear machines. This machine type can be used to build a magnetically levitating long-range linear drive system, whose rail does not need any active materials apart from iron. A dynamic machine model is developed by means of equivalent magnetic models, taking into account air-gap variation and magnetic saturation. The effects of these phenomena are analyzed using finite-element method (FEM) simulations of a test machine. The parameters of the proposed model can be identified using the FEM or measured data. The model can be applied to real-time control and time-domain simulations. The model is validated by means of experiments.

6.2 Scientific Contributions

The main scientific contributions of the dissertation are summarized as follows:

- A simple explicit-function based magnetic model (2.12) is proposed for bearingless SyRMs in Publication II, taking into account the effects of the self-saturation and the cross-saturation between the main and the suspension windings. Based on the FEM analysis it is shown that the cross-coupling due to saturation can be present even with a centric rotor.

- A model-based design method for a state-space flux-linkage controller is developed for bearingless SyRMs in Publication III. The proposed controller is easy to apply and automatically takes into account the cross-coupling between the main and the suspension windings. Analytical tuning rules for the controller gains are derived.

- An analytical model including rotor eccentricity is proposed for bearingless SyRMs in Publication IV. The proposed model improves upon the existing textbook model [5] by including more terms in the inverse air-gap length approximation, which gives it better accuracy in predicting radial forces under eccentric rotor conditions.

- A method to link the textbook model of the bearingless SyRM with separated windings to the machines with a combined multiphase winding is proposed in Publication V. The developed method allows to apply the existing dynamic models of separated windings SyRMs to the machines with combined windings.

- A state-space levitation controller is designed for a double-sided bearingless linear-motor system in Publication VI. Analytical design rules for the levitation controller are derived. The control system includes a feedback linearization method, which is based on the magnetic model of the machine and can take into account the effects of saturation and air gap variation.

- A dynamic model for bearingless FSPM linear machines is developed in Publication VII. The proposed model is derived from the equivalent magnetic circuit and takes into account air gap variation and magnetic saturation, which allows it to predict the force production of the machine at various operating conditions with good accuracy.

7. Conclusions

Bearingless machines, specifically SyRMs and FSPM linear machines, were studied in the scope of this dissertation. Due to the complex nature of these devices, conventional control methods are often insufficient to provide the desired level of levitation stability and driving performance. To improve the performance of bearingless machines, more sophisticated control methods, such as model-based control, have to be employed. Model-based methods can also provide a more thorough understanding of the system behavior, dynamics, and characteristics. However, the effectiveness of the control system heavily depends on the accuracy of the machine model, especially if high dynamic performance is required. This fact motivates the development of the dynamic models for bearingless machines. The mathematical machine model should be sufficiently accurate to represent the behavior of the actual machine to be applicable for control design purposes. Other important requirements are the generality and the physical consistency of the model, which ensure its applicability to different machine designs. Accurate analytical models are also useful for estimation purposes, time-domain simulations, and stability and robustness analyses.

In an effort to improve upon the existing modeling approaches, this dissertation focuses mainly on the modeling of two important phenomena: magnetic saturation and air gap variation. These are discussed in relation to bearingless SyRMs in Publication II and Publication IV respectively. A related future research topic could be to combine these modeling approaches in order to include both phenomena at once. By using the linking method proposed in Publication V, the models developed for bearingless SyRMs with separated windings can be also applied to machines with combined multiphase windings. A dynamic model for bearingless linear FSPM machines is developed in Publication VII, which accounts for both the saturation and the air gap variation. The accuracy of the proposed models was verified with FEM, including their ability to predict the magnetic behavior and the force production across different operating points. Proposed models can be parameterized via fitting to FEM-based or measured data. Future research could focus on developing identification methods to parameterize

the proposed models.

The proposed improvements to the modeling of bearingless machines are used as a basis for the contributions in control design. Among these contributions, it was discovered that classical pole placement control theory is well suited for levitation control of bearingless machines. For the inner control loop, Publication III proposes an elegant solution for changing the state variable from current to flux linkage. This allows a simple linear controller to effectively control the currents in the machine irrespective of the saturation, while also inherently decoupling the torque and force production. A levitation controller and a full-order state observer design is proposed in Publication VI. Using state-feedback control with direct pole placement results in an adequate levitation performance, as demonstrated by applying the developed controller to three experimental bearingless systems. Analytical tuning rules are given for each developed controller.

The reference calculation is an important part in a cascaded control system, whose role is to map the force references requested by the levitation controller to the current references for the inner control loop. Using constant coefficients for this mapping is often insufficient in the presence of nonlinear effects. Publication II and Publication VI demonstrate an improved control system performance when applying feedback linearization for a more accurate reference calculation.

Experimental results, including the force measurements of the linear FSPM machine prototype and levitation tests of the three bearingless prototypes, demonstrate the practical applicability of the proposed methods.

References

[1] J. R. Gómez, E. C. Quispe, R. P. Castrillón Mendoza, and P. R. Viego. Identification of technoeconomic opportunities with the use of premium efficiency motors as alternative for developing countries. *Energies*, 13(20), 2020.

[2] M. Key. The high cost of ignoring chiller oil buildup. *RSES Journal*, Nov. 2002.

[3] A. H. Bonnett. Cause and analysis of bearing failures in electrical motors. In *Proc. 39th Annual Petroleum and Chemical Industry Conference*, pages 87–95, San Antonio, TX, 1992.

[4] J. W. Jaisle. Turbocharger with magnetic bearing system that includes dampers. *United States Patent No. 6 846 167 B2*.

[5] A. Chiba, T. Fukao, O. Ichikawa, M. Oshima, M. Takemoto, and D. G. Dorrell. *Magnetic bearings and bearingless drives*. Newnes, Burlington, MA, 1st edition, 2005.

[6] W. Gruber and S. Silber. 20 years bearingless slice motor – its developments and applications. In *Proc. ISMB*, Kitakyushu, Japan, Aug. 2016.

[7] W. Gruber. Bearingless slice motors: general overview and the special case of novel magnet-free rotors. In *Innovative Small Drives and Micro-Motor Systems; 9. GMM/ETG Symposium*, pages 1–6, Nuremberg, Germany, Sep. 2013.

[8] Bearingless pumps - Levitronix. Accessed on 6 May 2021. Available online: https://www.levitronix.com/en/bearingless-pumps.html.

[9] P. K. Hermann. A radial active magnetic bearing having a rotating drive. *London Patent No. 1 500 809*.

[10] P. Meinke and G. Flachenecker. Electromagnetic drive assembly for rotary bodies using a magnetically mounted rotor, July 1974. *United States Patent No. 3 988 658*.

[11] R. Bosch. Development of a bearingless electric motor. In *Proc. ICEM*, page 373–375, Pisa, Italy, Sept. 1988.

[12] J. Chen, J. Zhu, and E. L. Severson. Review of bearingless motor technology for significant power applications. *IEEE Transactions on Industry Applications*, 56(2):1377–1388, Mar./Apr. 2020.

[13] B. Liu. Survey of bearingless motor technologies and applications. In *Proc. ICMA*, pages 1983–1988, Beijing, China, Aug. 2015.

[14] A. O. Salazar, A. Chiba, and T. Fukao. A review of developments in bearingless motors. In *Proc. ISMB*, pages 335–340, Aug. 2000.

[15] A. Boglietti and M. Pastorelli. Induction and synchronous reluctance motors comparison. In *Proc. IEEE IECON*, pages 2041–2044, Orlando, FL, Nov. 2008.

[16] ABB synchronous reluctance motors. Accessed on 6 May 2021. Available online: https://new.abb.com/motors-generators/iec-low-voltage-motors/process-performance-motors/synchronous-reluctance-motors.

[17] M. Palmieri, M. Perta, and F. Cupertino. Design of a 50.000-r/min synchronous reluctance machine for an aeronautic diesel engine compressor. *IEEE Transactions on Industry Applications*, 52(5):3831–3838, Sept./Oct. 2016.

[18] F. Cupertino, M. Palmieri, and G. Pellegrino. Design of high-speed synchronous reluctance machines. In *Proc. IEEE ECCE*, pages 4828–4834, Montreal, QC, Canada, Sept. 2015.

[19] J. Ikäheimo, J. Kolehmainen, T. Känsäkangas, V. Kivelä, and R. R. Moghaddam. Synchronous high-speed reluctance machine with novel rotor construction. *IEEE Transactions on Industrial Electronics*, 61(6):2969–2975, June 2014.

[20] J. D. Park, C. Khalizadeh, and H. Hofmann. Design and control of high-speed solid-rotor synchronous reluctance drive with three-phase lc filter. In *Proc. IEEE Fortieth IAS Annual Meeting*, pages 715–722, Hong Kong, China, Oct. 2005.

[21] J. Bichsel. The bearingless electrical machine. In *Proc. Int. Symp. Magn. Suspension. Technol*, pages 561–573, Hampton, VA, 1991.

[22] R. Schob and J. Bichsel. Vector control of the bearingless motor. In *Proc. ISMB*, pages 327–332, Zurich, Aug. 1994.

[23] M. A. Rahman, T. Fukao, and A. Chiba. Principles and developments of bearingless ac motors. In *Proc. IPEC*, volume 3, pages 1334–1339, Yokohama, Japan, Apr. 1995.

[24] R. L. A. Ribeiro, F. E. F. Castro, A. O. Salazar, and A. L. Maitelli. A suitable current control strategy for split-phase bearingless three-phase induction machine. In *Proc. IEEE 36th Power Electronics Specialists Conference*, pages 701–706, Recife, Brazil, June 2005.

[25] E. F. Rodriguez and J. A. Santisteban. An improved control system for a split winding bearingless induction motor. *IEEE Transactions on Industrial Electronics*, 58(8):3401–3408, Aug. 2011.

[26] J. M. S. Ferreira, M. Zucca, A. O. Salazar, and L. Donadio. Analysis of a bearingless machine with divided windings. *IEEE Trans. on Mag.*, 41(10):3931–3933, Oct. 2005.

[27] V. F. Victor, F. O. Quintaes, J. S. B. Lopes, L. d. S. Junior, A. S. Lock, and A. O. Salazar. Analysis and study of a bearingless ac motor type divided winding, based on a conventional squirrel cage induction motor. *IEEE Trans. on Mag.*, 48(11):3571–3574, Nov. 2012.

[28] K. Raggl, J. W. Kolar, and T. Nussbaumer. Comparison of winding concepts for bearingless pumps. In *Proc. ICPE*, pages 1013–1020, Daegu, Korea, Oct. 2007.

[29] E. L. Severson, R. Nilssen, T. Undeland, and N. Mohan. Design of dual purpose no-voltage combined windings for bearingless motors. *IEEE Transactions on Industry Applications*, 53(5):4368–4379, Sept./Oct. 2017.

[30] W. K. S. Khoo. Bridge configured winding for polyphase self-bearing machines. *IEEE Trans. on Mag.*, 41(4):1289–1295, Apr. 2005.

[31] W. K. S. Khoo, K. Kalita, and S. D. Garvey. Practical implementation of the bridge configured winding for producing controllable transverse forces in electrical machines. *IEEE Trans. on Mag.*, 47(6):1712–1718, June 2011.

[32] R. Oishi, S. Horima, H. Sugimoto, and A. Chiba. A novel parallel motor winding structure for bearingless motors. *IEEE Trans. on Mag.*, 49(5):2287–2290, May 2013.

[33] E. Severson, S. Gandikota, and N. Mohan. Practical implementation of dual-purpose no-voltage drives for bearingless motors. *IEEE Transactions on Industry Applications*, 52(2):1509–1518, Mar./Apr. 2016.

[34] H. W. Lee, K. C. Kim, and J. Lee. Review of maglev train technologies. *IEEE Trans. on Mag.*, 42(7):1917–1925, July 2006.

[35] G. Genta. *Dynamics of rotating systems*. Springer-Verlag New York, New York, NY, 1st edition, 2005.

[36] G. Schweitzer and E. H. Maslen. *Magnetic bearings. Theory, design, and application to rotating machinery.* Springer-Verlag Berlin Heidelberg, Berlin, 1st edition, 2009.

[37] S. E. Saarakkala. *Identification and speed control design of resonating mechanical systems in electric drives*. PhD thesis, Aalto University, 2014.

[38] E. Hoang, A. H. Ben-Ahmed, and J. Lucidarme. Switching flux permanent magnet polyphased synchronous machines. In *Proc. EPE*, volume 3, pages 903–908, Trondheim, Norway, Sep. 1997.

[39] A. E. Fitzgerald, C. Kingsley, Jr., and S. D. Umans. *Electric machinery*. McGraw-Hill, Boston, MA, 6th edition, 2003.

[40] A. Vagati. The synchronous reluctance solution: a new alternative in ac drives. In *Proc. IEEE IECON*, pages 1–13, Sep. 1994.

[41] J. Park, C. Kalev, and H. F. Hofmann. Control of high-speed solid-rotor synchronous reluctance motor/generator for flywheel-based uninterruptible power supplies. *IEEE Transactions on Industrial Electronics*, 55(8):3038–3046, Aug. 2008.

[42] R. Peña-Alzola, R. Sebastián, J. Quesada, and A. Colmenar. Review of flywheel based energy storage systems. In *Proc. International Conference on Power Engineering, Energy and Electrical Drives*, pages 1–6, Malaga, Spain, May 2011.

[43] M. Recheis. Increasing bearing life-time of mobile flywheels by using bearingless drive methods. In *Proc. ISMB*, pages 360–365, Linz, Austria, Aug. 2014.

[44] J. Park, C. Kalev, and H. F. Hofmann. Analysis and reduction of time harmonic rotor loss in solid-rotor synchronous reluctance drive. *IEEE Transactions on Power Electronics*, 23(2):985–992, Mar. 2008.

[45] A. Chiba, K. Chida, and T. Fukao. Principle and characteristics of a reluctance motor with windings of magnetic bearing. In *Proc. IPEC*, pages 919–926, Tokyo, Japan, Apr. 1990.

[46] A. Chiba, M. A. Rahman, and T. Fukao. Radial force in a bearingless reluctance motor. *IEEE Trans. on Mag.*, 27(2):786–790, Mar. 1991.

[47] T. Holenstein, T. Nussbaumer, and J. Kolar. A bearingless synchronous reluctance slice motor with rotor flux barriers. In *Proc. IPEC*, pages 3619–3626, Niigata, Japan, May 2018.

[48] A. Chiba, T. Deido, T. Fukao, and M. A. Rahman. An analysis of bearingless ac motors. *IEEE Transactions on Energy Conversion*, 9(1):61–68, Mar. 1994.

[49] W. Bu, S. Huang, S. Wan, and W. Liu. General analytical models of inductance matrices of four-pole bearingless motors with two-pole controlling windings. *IEEE Trans. on Mag.*, 45(9):3316–3321, Sept. 2009.

[50] C. Michioka, T. Sakamoto, O. Ichikawa, A. Chiba, and T. Fukao. A decoupling control method of reluctance-type bearingless motors considering magnetic saturation. *IEEE Transactions on Industry Applications*, 32(5):1204–1210, Sep./Oct. 1996.

[51] A. Chiba, M. Hanazawa, T. Fukao, and M. A. Rahman. Effects of magnetic saturation on radial force of bearingless synchronous reluctance motors. *IEEE Transactions on Industry Applications*, 32(2):354–362, Mar./Apr. 1996.

[52] M. F. Far, V. Mukherjee, F. Martin, P. Rasilo, and A. Belahcen. Model order reduction of bearingless reluctance motor including eccentricity. In *Proc. ICEM*, pages 2243–2249, Alexandroupoli, Greece, Oct. 2018.

[53] S. Yamamoto, T. Ara, and K. Matsuse. A method to calculate transient characteristics of synchronous reluctance motors considering iron loss and cross-magnetic saturation. *IEEE Transactions on Industry Applications*, 43(1):47–56, Jan./Feb. 2007.

[54] D. Steinert, T. Nussbaumer, and J. W. Kolar. Slotless bearingless disk drive for high-speed and high-purity applications. *IEEE Transactions on Industrial Electronics*, 61(11):5974–5986, Nov. 2014.

[55] Y. Jiang, R. A. Torres, and E. L. Severson. Current regulation in parallel combined winding bearingless motors. *IEEE Transactions on Industry Applications*, June 2019.

[56] W. Gruber and K. Radman. Modeling and realization of a bearingless flux-switching slice motor. *Actuators*, 6(12), Mar. 2017.

[57] N. Turk, N. Bulić, and W. Gruber. Nonlinear control of a bearingless flux-switching slice motor with combined winding system. *IEEE/ASME Transactions on Mechatronics*, 25(1):152–163, Feb. 2020.

[58] S. Zhou, H. Yu, M. Hu, C. Jiang, and L. Huang. Nonlinear equivalent magnetic circuit analysis for linear flux-switching permanent magnet machines. 46(2):882–886, Feb. 2012.

[59] R. Cao, M. Cheng, C. Mi, W. Hua, X. Wang, and W. Zhao. Modeling of a complementary and modular linear flux-switching permanent magnet motor for urban rail transit applications. 27(2):489–497, Jun. 2012.

[60] S. R. Aleksandrov, L. Wang, D. T. E. H. van Casteren, J. J. H. Paulides, and E. A. Lomonova. Semi-analytical analysis of rotating and linear flux-switching PM machines including skewing. In *Proc. EVER*, pages 1–5, Monte Carlo, Monaco, Apr. 2017.

[61] R. P. Jastrzebski, P. Jaatinen, and O. Pyrhönen. Modeling and control design simulations of a linear flux-switching permanent-magnet-levitated motor. *Mechanical Engineering Journal*, 4(5), July 2017.

[62] H. H. Woodson and J. R. Melcher. *Electromechanical dynamics: part I: discrete systems*. John Wiley & Sons, New York, 1968. Massachusetts Institute of Technology: MIT OpenCourseWare.

[63] D. Meeker. Magnetic circuit derivation of energy stored in a permanent magnet. Apr. 2007.

[64] J. Fischer and U. Moser. Die nachbildung von magnetisierungskurven durch einfache algebraische oder transzendente funktionen. *Archiv für Electrotechnik*, 42(5):286–299, 1956.

[65] M. Hinkkanen, P. Pescetto, E. Mölsä, S. E. Saarakkala, G. Pellegrino, and R. Bojoi. Sensorless self-commissioning of synchronous reluctance motors at standstill without rotor locking. 53(3):2120–2129, May/Jun. 2017.

[66] G. F. Franklin, M.L. Workman, and J.D. Powell. *Digital control of dynamic systems*. Addison-Wesley Longman, 1997.

[67] F. Briz and M. Hinkkanen. Design, implementation and performance of synchronous current regulators for ac drives. *Chinese Journal of Electrical Engineering*, 4(3):53–65, 9 2018.

[68] G. L. Kruger, G. van Schoor, and P. A. van Vuuren. Control of magnetically suspended rotor combined with motor drive system. In *Proc. IFAC'14*, pages 7252–7257, Cape Town, South Africa, Aug. 2014.

[69] A. Smirnov, R. P. Jastrzebski, K. Hynynen, and O. Pyrhönen. Comparison of suboptimal control methods in magnetic levitation system. In *Proc. EPE*, pages 1–10, Lille, France, Sept. 2013.

[70] J. Asama, T. Oi, T. Oiwa, and A. Chiba. Simple driving method for a 2-dof controlled bearingless motor using one three-phase inverter. *IEEE Transactions on Industry Applications*, 54(5):4365–4376, Sept./Oct. 2018.

[71] W. Gruber and S. Silber. Dual field-oriented control of bearingless motors with combined winding system. In *Proc. IPEC*, pages 4028–4033, Niigata, Japan, May 2018.

[72] P. Jaatinen, J. Vuojolainen, N. Nevaranta, R. P. Jastrzebski, and O. Pyrhönen. Control system commissioning of fully levitated bearingless machine. *Modeling, Identification and Control*, 40(1):27–39, 2019.

[73] L. Harnefors and H. P. Nee. Model-based current control of ac machines using the internal model control method. *IEEE Transactions on Industry Applications*, 34(1):133–141, Jan. 1998.

[74] Z. Qu, T. Tuovinen, and M. Hinkkanen. Inclusion of magnetic saturation in dynamic models of synchronous reluctance motors. In *Proc. XXth International Conference on Electrical Machines*, pages 994–1000, Marseille, France, Sept. 2012.

[75] K. Hijikata, N. Ando, M. Takemoto, and S. Ogasawara. A decoupling method for current regulation in bearingless motors using ac suspension current. In *Proc. ICEMS*, pages 2310–2314, Hangzhou, China, Oct. 2014.

[76] F. Briz, M. W. Degner, and R. D. Lorenz. Dynamic analysis of current regulators for ac motors using complex vectors. *IEEE Transactions on Industry Applications*, 35(6):1424–1432, Nov. 1999.

[77] M. Hinkkanen, H. Asad Ali Awan, Z. Qu, T. Tuovinen, and F. Briz. Current control for synchronous motor drives: direct discrete-time pole-placement design. *IEEE Transactions on Industry Applications*, 52(2):1530–1541, Mar. 2016.

[78] H. A. A. Awan, S. E. Saarakkala, and M. Hinkkanen. Flux-linkage-based current control of saturated synchronous motors. *IEEE Transactions on Industry Applications*, 55(5):4762–4769, Sept./Oct. 2019.

[79] L. Harnefors, S. E. Saarakkala, and M. Hinkkanen. Speed control of electrical drives using classical control methods. In *Proc. IEEE ECCE*, pages 1713–1720, Phoenix, AZ, Sept. 2011.

[80] H. Grabner, W. Amrhein, S. Silber, and W. Gruber. Nonlinear feedback control of a bearingless brushless dc motor. *IEEE/ASME Transactions on Mechatronics*, 15(1):40–47, Feb. 2010.

[81] M. Ooshima, A. Chiba, M. A. Rahman, and T. Fukao. An improved control method of buried-type ipm bearingless motors considering magnetic saturation and magnetic pull variation. *IEEE Transactions on Energy Conversion*, 19(3):569–575, Sept. 2004.

[82] H. Mitterhofer and W. Amrhein. Motion control strategy and operational behaviour of a high speed bearingless disc drive. In *Proc. PEMD*, pages 1–6, Bristol, United Kingdom, Mar. 2012.

[83] E. L. Severson. *Bearingless AC homopolar machine design and control for distributed flywheel energy storage*. PhD thesis, University of Minnesota, 2015.

[84] F. Zürcher, T. Nussbaumer, S. Walter, C. Wegmüller, and J.W. Kolar. Comparison of different control concepts for bearingless brushless motors. In *Proc. ISMB*, pages 223–231, Wuhan, China, Aug. 2010.

[85] S. Sahoo, R. P. Jastrzebski, D. Kepsu, K. Zenger, P. Jaatinen, and O. Pyrhönen. Modelling and model-based control of a bearingless 100 kw electric motor for high-speed applications. In *Proc. EPE*, pages 1–10, Riga, Latvia, Sep. 2018.

[86] P. Jaatinen. *Design and control of a permanent magnet bearingless machine*. PhD thesis, LUT University, 2019.

[87] P. Jaatinen, N. Nevaranta, J. Vuojolainen, R. P. Jastrzebski, and O. Pyrhönen. h_∞ control of a dual motor bearingless machine. In *Proc. IEMDC*, pages 875–881, San Diego, CA, May 2019.

[88] V. Mukherjee, J. Pippuri, A. Belahcen, S. E. Saarakkala, M. Hinkkanen, and K. Tammi. Finite element analysis for bearingless operation of a multi flux barrier synchronous reluctance motor. In *Proc. ICEMS*, pages 688–691, Pattaya, Thailand, Oct. 2015.

[89] C. M. Spargo. *Synchronous reluctance motors with fractional slot-concentrated windings*. PhD thesis, University of Newcastle, 2016.

[90] C. M. Spargo, B. C. Mecrow, J. D. Widmer, and C. Morton. Application of fractional-slot concentrated windings to synchronous reluctance motors. *IEEE Transactions on Industry Applications*, 51(2):1446–1455, Mar./Apr. 2015.

[91] J. Passenbrunner, S. Silber, and W. Amrhein. Investigation of a digital eddy current sensor. In *Proc. IEEE IEMDC*, pages 728–734, May 2015.

[92] R. Hosseinzadeh, F. Martin, and M. Hinkkanen. A dynamic model for six-degree-of-freedom bearingless linear motor systems. *IEEE Transactions on Industry Applications*, early access, 2021. doi:10.1109/TIA.2021.3077354.

Errata

Publication V

In Fig. 9(b) the cyan current component trace should have a legend i_{C2} instead of i_{C3}.

In Section IV B, the tilting stabilizing torque T_{stab} is given with a measurement unit of Nm/A, while the correct measurement unit is Nm·A. Similarly, the axial passive stabilizing force F_{stab} is given with a measurement unit of N/A, but the correct measurement unit is N·A.

Towards magnetically levitated electric motors

Bearingless motor is an electric machine that integrates the functions of a conventional electric motor and a magnetic bearing in one unit. Magnetic suspension provides a completely contactless operation, which eliminates friction, the need for lubrication and maintenance, and allows to reach high rotational speeds.

This book makes an effort to give a comprehensive overview of the mathematical modeling and control aspects of bearingless synchronous reluctance machines (SyRMs) and linear flux-switching permanent magnet (FSPM) machines. Particular attention in modeling is given to characterizing the force production under the effects of magnetic saturation and air gap variation. The proposed dynamic models are utilized as a basis for the development of model-based control systems, which were experimentally tested on three prototype bearingless drives.

Aalto-DD 186/2021

ISBN 978-952-64-0650-3 (printed)
ISBN 978-952-64-0651-0 (pdf)
ISSN 1799-4934 (printed)
ISSN 1799-4942 (pdf)

Aalto University
School of Electrical Engineering
Department of Electrical Engineering and Automation
www.aalto.fi

BUSINESS + ECONOMY

ART + DESIGN + ARCHITECTURE

SCIENCE + TECHNOLOGY

CROSSOVER

DOCTORAL DISSERTATIONS